J. Fluid Mech. (1990), *vol.* 220, *pp.* 187–252
Printed in Great Britain

The phase diffusion and mean drift equations for convection at finite Rayleigh numbers in large containers

By ALAN C. NEWELL[1], THIERRY PASSOT[2] AND MOHAMMAD SOULI[1]

[1] Arizona Center for the Mathematical Sciences, University of Arizona, Tucson, AZ 85721, USA
[2] Observatoire de Nice, BP 139, 06003 Nice Cedex, FRANCE

(Received 13 October 1989 and in revised form 16 March 1990)

We derive the phase diffusion and mean drift equations for the Oberbeck–Boussinesq equations in large-aspect-ratio containers. We are able to recover all the long-wave instability boundaries (Eckhaus, zigzag, skew-varicose) of straight parallel rolls found previously by Busse and his colleagues. Moreover, the development of the skew-varicose instability can be followed and it becomes clear how the mean drift field conspires to enhance the necking of phase contours necessary for the production of dislocation pairs. We can calculate the wavenumber selected by curved patterns and find very close agreement with the dominant wavenumbers observed by Heutmaker & Gollub at Prandtl number 2.5, and by Steinberg, Ahlers & Cannell at Prandtl number 6.1. We find a new instability, the focus instability, which causes circular target patterns to destabilize and which, at sufficiently large Rayleigh numbers, may play a major role in the onset of time dependence. Further, we predict the values of the Rayleigh number at which the time-dependent but spatially ordered patterns will become spatially disordered. The key difficulty in obtaining these equations is the fact that the phase diffusion equation appears as a solvability condition at order ϵ (the inverse aspect ratio) whereas the mean drift equation is the solvability condition at order ϵ^2. Therefore, we had to use extremely robust inversion methods to solve the singular equations at order ϵ and the techniques we use should prove to be invaluable in a wide range of similar situations. Finally, we discuss the introduction of the amplitude as an active order parameter near pattern defects, such as dislocations and foci.

1. Introduction

1.1. *General discussion and goals*

Convection in a horizontal layer of fluid heated from below provides a canonical example of pattern-forming transitions in continuous dissipative systems far from equilibrium. For an infinite horizontal layer of depth d in which the external conditions are symmetric about the midlayer level, a spatially uniform (pure conduction) state becomes unstable to a spatially periodic, time-independent state of straight, parallel, convecting rolls. The existence and stability of these roll solutions has been studied in detail by Busse and several colleagues (Busse 1967, 1978, 1981; Busse & Whitehead 1971, 1974; Clever & Busse 1974, 1978, 1979) over a period of twenty years. The conclusion is that, for a range of Rayleigh numbers R, depending

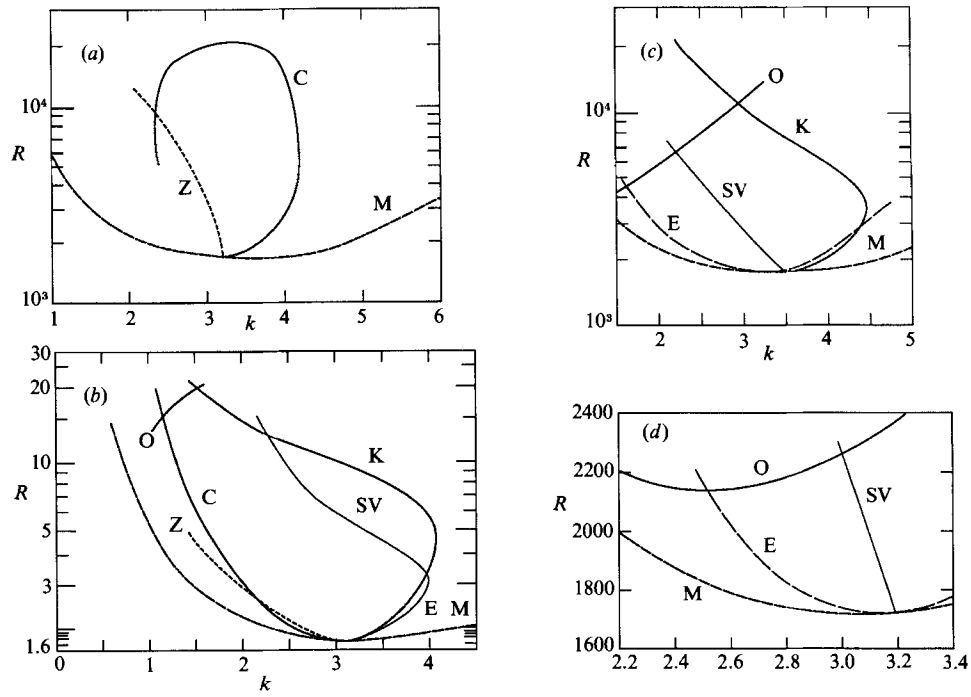

FIGURE 1. Schematic drawings of the Busse balloon at Prandtl numbers (*a*) $P = 70$, (*b*) $P = 2.5$, (*c*) $P = 0.71$, (*d*) $P = 0.1$. The borders are marked: C (cross-roll), Z (zigzag), SV (skew-varicose), E (Eckhaus), O (oscillations), K (knot), and denote the various instabilities. M denotes the neutral stability curve of the conduction solution.

on the Prandtl number P, the straight rolls are linearly stable if their wavenumber $k(R, P)$ lies in a band, called the Busse balloon. In figure 1 we display this balloon at several values of P. The caption gives names to the various instabilities which occur at the borders. The Busse balloon has been extraordinarily successful both qualitatively and quantitatively in predicting the onset of time-dependent behaviour for configurations dominated by straight parallel rolls.

However, in convecting boxes wide enough to hold many rolls (the ratio of a typical horizontal dimension L to the depth d is called the aspect ratio and denoted by Γ), these solutions are usually not reached when convection is initiated spontaneously. There are two main and connected reasons for this. First, the rotational symmetry of the infinite horizontal layer means that straight parallel rolls with different orientations can appear at different locations. Second, these local orientations are often chosen by lateral sidewalls, as the rolls tend to align themselves so that their axes are everywhere almost normal to the boundary. Because of these reasons, the patterns which are attained are usually quite complicated, consisting of patches of curved rolls, often almost circular in shape, and defects such as disclinations, foci singularities, dislocations and grain boundaries. When the pattern is stationary, these pattern singularities or defects are necessary in order to mediate between the various roll patches because it is simply impossible to tile a closed box with regions of smooth rolls. When the pattern is evolving, defects, and in particular dislocations, are particularly important as mechanisms for adjusting the local wavenumber.

To illustrate these statements we show in figure 2 results from experiments by

Heutmaker & Gollub (1987), Croquette, Mory & Schosseler (1983) in cylindrical boxes, by Gollub, McCarriar & Steinman (1982) in rectangular ones, and numerical experiments by Greenside & Coughran (1986) carried out on the Swift–Hohenberg equation. Observe that the patterns (some are equilibrium states; others are snapshots of time-dependent states) often contain almost circular patches surrounding sidewall foci, disclinations (marked DS in figure 2*b*, *c*) which separate circular patches, dislocations (marked D in figure 2*d*, *e*, *h*) which allow the pattern adjust its local wavenumber, and grain boundaries (marked G in figure 2*a*) attached to the sidewalls. What is not obvious from these pictures is the presence of a mean drift flow field which is driven by the curvature of the rolls and the variation in intensity in the underlying pattern. In figure 2(*e*), we have superimposed the mean drift field which is produced by that pattern. The mean drift is driven by the pattern curvature and in turn affects the pattern by advecting its phase contours. It has extremely important consequences and is responsible for turning the Eckhaus stability boundary sharply left towards smaller wavenumbers (see figure 1*b*, *c*), where it is called the skew-varicose instability, and in triggering the focus instability associated with circular and curved patches. This latter instability, first observed by Heutmaker & Gollub (1987), Steinberg, Ahlers & Cannell (1985), Croquette *et al.* (1986*b*), and discovered analytically by Newell (1988) and Pocheau (1988) using the Cross–Newell equations (which we shall shortly discuss) and derived in §3.2 of this paper using the correct equations, is not one of the borders of the Busse balloon because it is an instability of circular target patterns and not an instability of straight parallel rolls. We shall argue that the basic instability mechanism, which is that the compression of rolls by mean drift velocity advection overcomes the relaxation of the pattern towards a selected wavenumber, may also be important for understanding the onset of time dependence at low and low to moderate Prandtl numbers.

The goal of this paper is to write down macroscopic equations for the wavevector $\boldsymbol{k}$ and a depth-averaged (with appropriate weighting) mean drift velocity field $\boldsymbol{V}$, both of which quantities vary slowly over the pattern. Except at singularities (which are points or lines and therefore of zero measure with respect to area), the spatial gradients of these fields are of order $\epsilon = \Gamma^{-1}$, the inverse aspect ratio, and their time derivatives are of order $\epsilon^2 = \Gamma^{-2}$, the inverse of the horizontal diffusion timescale. The form of these equations was first written down by Cross & Newell (1984). They used model equations in order to derive the phase diffusion equation (1.1); the mean drift equation was written down by an experienced hand guided by small-amplitude theory. It turns out that, whereas the Cross–Newell mean drift equation had many features that were correct, it had neglected terms that give rise to important quantitative differences. Although several of the key ideas were developed in the earlier paper, the derivation of both equations for the full Oberbeck–Boussinesq model proved to be a daunting task for reasons we shall describe later. The phase diffusion and mean drift equations are

$$\frac{\partial \Theta}{\partial T} + \rho(k)\, \boldsymbol{V} \cdot \boldsymbol{\nabla}\Theta + \frac{1}{\tau(k)} \boldsymbol{\nabla} \cdot \boldsymbol{k} B(k) = 0, \tag{1.1}$$

$$\hat{\boldsymbol{z}} \cdot \boldsymbol{\nabla} \times \{\hat{\boldsymbol{k}}\alpha(\hat{\boldsymbol{k}} \times \boldsymbol{\nabla}\psi) \cdot \boldsymbol{z}\} - \boldsymbol{\nabla} \cdot \hat{\boldsymbol{k}}\beta\hat{\boldsymbol{k}} \cdot \boldsymbol{\nabla}\psi = \hat{\boldsymbol{z}} \cdot \boldsymbol{\nabla} \times \left(\sigma \boldsymbol{k} \boldsymbol{\nabla} \cdot \boldsymbol{k} A^2 - \frac{\hat{\boldsymbol{k}}}{\tau_\alpha} \boldsymbol{\nabla} \cdot \boldsymbol{k} B_\alpha\right)$$

$$- \boldsymbol{\nabla} \cdot \hat{\boldsymbol{k}} (\boldsymbol{\nabla} \times \boldsymbol{k} B_\beta) \cdot \hat{\boldsymbol{z}}, \tag{1.2}$$

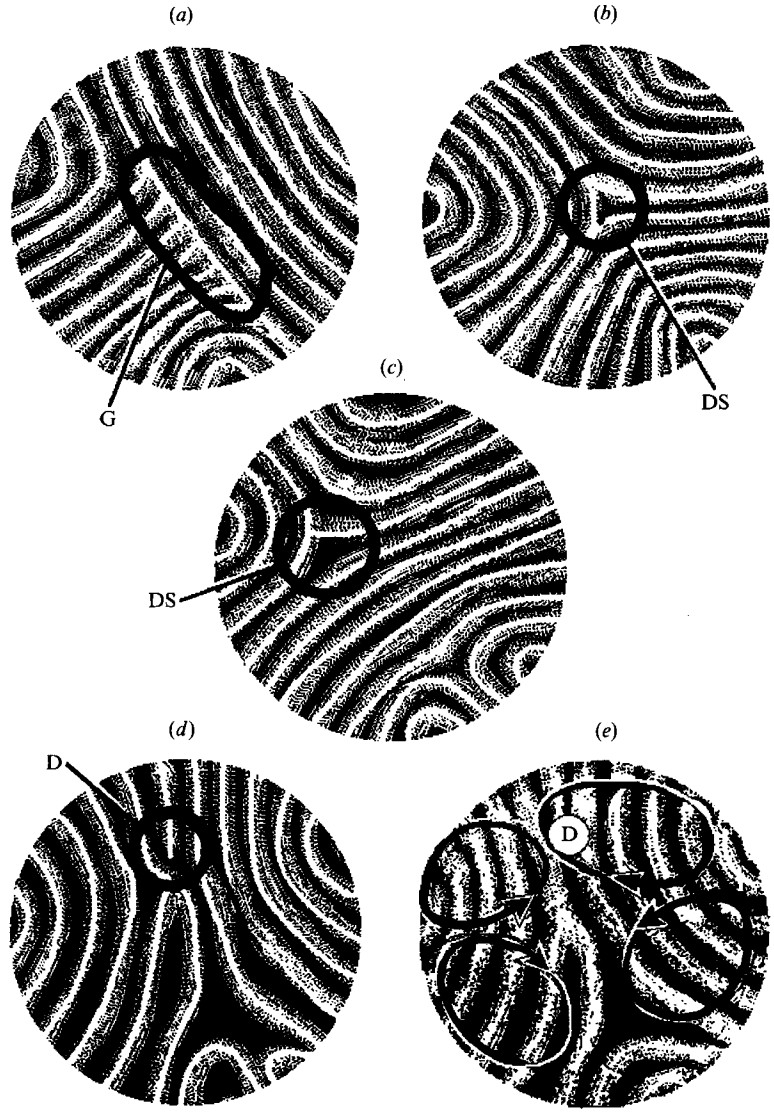

FIGURE 2(*a–e*). For caption see facing page.

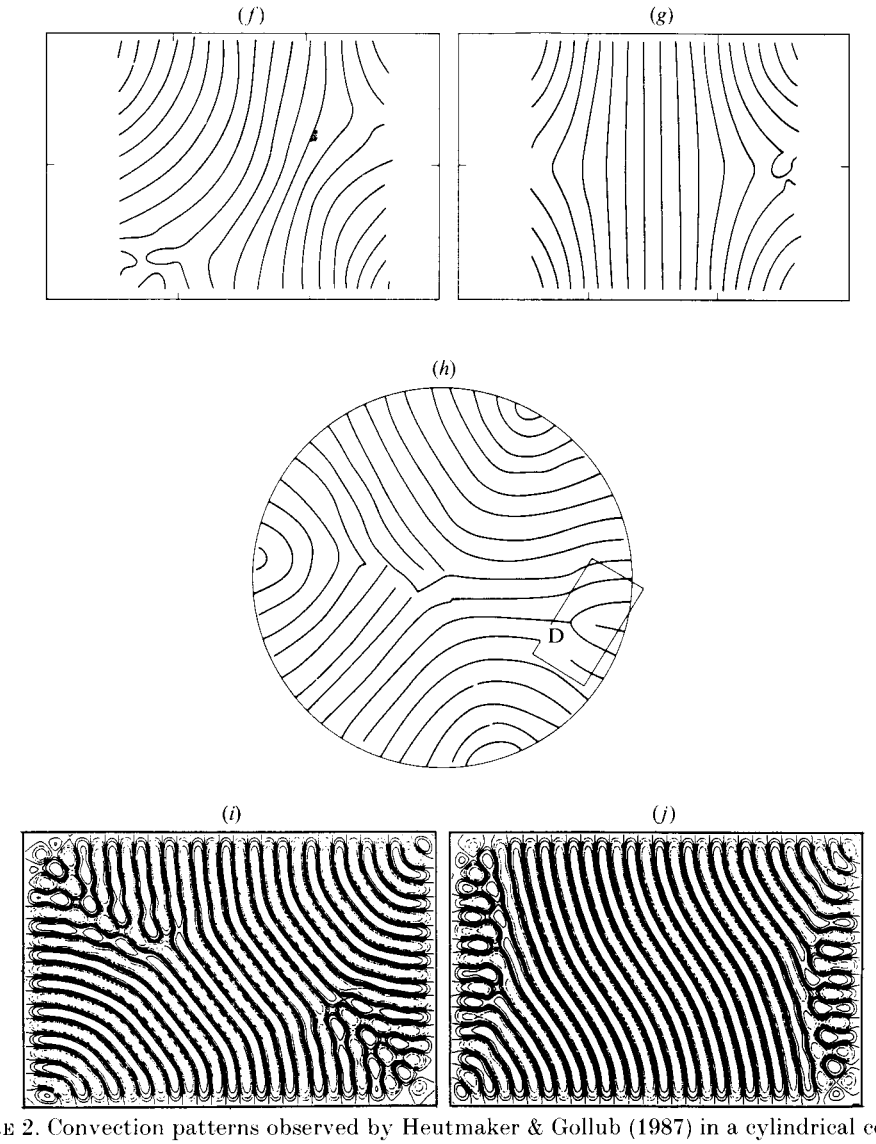

FIGURE 2. Convection patterns observed by Heutmaker & Gollub (1987) in a cylindrical container at Prandtl number 2.5. (*a*) R = $1.17R_c$, showing a grain boundary (G). Also note that the roll axes are not perpendicular to the boundary. (*b*) and (*c*) Two different final stationary states at the same parameter values. They display foci singularities and disclinations (DS). (*d*) and (*e*) $R = 4.84R_c$; sequential snapshots of the formation of a dislocations pair (D). In (*b*, *c*, *d*, *e*) the roll axes are everywhere almost perpendicular to the boundary. (*f*) and (*g*) From experiments by Gollub *et al.* (1982) in a rectangular container, showing the pattern after the horizontal diffusion scale (*f*) and after the aspect ratio times the horizontal diffusion timescale (*g*). (*h*) From Croquette *et al.* (1983). (*i*) and (*j*) A numerical simulation by Greenside & Coughran (1986) of the Swift–Hohenberg equations. Note their similarity with (*f*) and (*g*).

where $T = \epsilon^2 t$, $(X, Y) = \epsilon(x, y)$, $\epsilon^{-1} = \Gamma$, $\hat{\boldsymbol{z}}$ the unit vector in the vertical direction, and

$$\boldsymbol{k} = \boldsymbol{\nabla}\Theta, \quad k = |\boldsymbol{k}|, \quad \hat{\boldsymbol{k}} = \frac{\boldsymbol{k}}{k}, \quad \boldsymbol{V} = \boldsymbol{\nabla} \times \psi \hat{\boldsymbol{z}}. \tag{1.3}$$

The functions $B(k)$, $B_\alpha(k)$, $B_\beta(k)$, $\tau(k)$, $\tau_\alpha(k)$, $\rho(k)$, $\alpha(k)$, $\beta(k)$ and $A^2(k)$ are explicitly calculated and their graphs as functions of k and the graphs of important functions

of these quantities are given in figures 9 and 10 in §3. Of these nine functions, only two, A^2 and B_α, can be combined but, for pedagogic reasons explained later, we choose not to do so at this time. The coefficient $\rho(k)$ cannot be incorporated because it is not quite constant. The equations have the properties that they are rotationally invariant and locally Galilean invariant even though, because of the no-slip boundary condition, the original boundary value problem is not. They reproduce all the long-wave instabilities (zigzag, Eckhaus and skew-varicose) of the Busse balloon exactly. At infinite Prandtl number and in coordinates parallel (X) and perpendicular (Y) to the local wavevector $\boldsymbol{k}$, (1.1) is the Pomeau–Manneville (1979) phase diffusion equation,

$$\Theta_T - D_\parallel(k)\,\Theta_{XX} - D_\perp(k)\,\Theta_{YY} = 0, \tag{1.4}$$

with

$$D_\parallel = -\frac{1}{\tau(k)}\frac{\mathrm{d}}{\mathrm{d}k}(kB), \quad D_\perp = -\frac{1}{\tau(k)}B(k), \tag{1.5}$$

except that here the coefficients are exactly calculated and the corresponding wavevector $\boldsymbol{k} = \boldsymbol{\nabla}_X\Theta$ is not a small perturbation of a fixed wavevector (Pomeau & Manneville take the phase Θ to be $\boldsymbol{k}_0 \cdot \boldsymbol{X} + \epsilon\Phi(X, Y, T)$). The loci in the (R, k)-plane at which the diffusion coefficients become negative, that is where $D_\perp(k) = 0$ and $D_\parallel(k) = 0$ are the borders of the zigzag and Eckhaus instabilities respectively. The zero of $B(k)$ and $D_\perp(k)$, which we shall call k_B, is the wavenumber selected by curved roll textures. At finite Prandtl number, the mean drift field comes into play and the zigzag boundary is moved far to the left (see figure 1*b*, *c*) whereas, on the right-hand boundary of the Busse balloon, for sufficiently large values of the Rayleigh number, the Eckhaus instability turns into the skew-varicose one. (Note: Some authors choose to denote the 'effective' perpendicular diffusion coefficient which includes mean drift effects by $D_\perp$ (the factor $-(B/\tau) - \rho k^2\sigma A^2$) in (3.17)) but we do not.) The calculation of these boundaries is carried out in §3.1. The equations also capture an instability, which we call the focus instability, experienced by circular target patterns and circular patches surrounding foci singularities. This instability is very important at low to moderate Prandtl numbers and serves to initiate time-dependent behaviour well within the confines of the Busse balloon. They can, in addition, be used to calculate the mean drift fields that are associated with various pattern configurations. We suggest that, when appropriately regularized, they also contain information about singularities and the nucleation and motion of defects, which we believe are suitably defined weak solutions. The regularization is achieved by adding back into the description an active rather than passive amplitude order parameter. We shall illustrate its importance when discussing the focus instability. The equation (1.2) would have the form proposed by Cross & Newell if α and β were constant and equal and the terms on the right-hand side of (1.2) that contain B_α and B_β were absent. This form would be roughly correct if one assumes that the horizontally averaged vertical profile of the mean drift velocity field is parabolic (Poiseuille-like), but it is not. Finally, the lateral sidewall boundary conditions most appropriate (we use the term appropriate advisedly; the extent to which $\boldsymbol{k} \cdot \hat{\boldsymbol{n}}$ is zero has not been theoretically derived) to these fields are that the wavevector $\boldsymbol{k}$ and mean drift velocity $\boldsymbol{V}$ fields are parallel to lateral boundaries; that is, if $\hat{\boldsymbol{n}}$ is the unit outward normal to the sidewall,

$$\boldsymbol{k} \cdot \hat{\boldsymbol{n}} = \boldsymbol{V} \cdot \hat{\boldsymbol{n}} = 0. \tag{1.6}$$

In certain cases where one applies thermal forcing at the lateral boundary, the roll axis will be parallel to it and then the appropriate boundary condition would be

$$\boldsymbol{k} \times \hat{\boldsymbol{n}} = 0. \tag{1.7}$$

1.2. *Experiments*

Over the past two decades, a series of very sophisticated and careful experiments, notably by Ahlers & Behringer (1978), Ahlers, Steinberg & Cannell (1985), Steinberg *et al.* (1985), Bergé & Dubois (1974), Busse & Whitehead (1974), Croquette, Le Gal & Pocheau (1986*a*), Croquette (1989*a*, *b*), Croquette *et al.* (1983), Gollub *et al.* (1982), Heutmaker & Gollub (1987), Kolodner *et al.* (1986*a*, *b*), Koschmieder & Pallas (1974), Krishnamurti (1970), have given us reliable details about pattern evolution in both rectangular and cylindrical boxes with large aspect ratios, covering all ranges of Prandtl number, high ($P > 7$), moderate ($1 < P < 7$), and low ($P < 1$). The control of the parameters in many of these experiments has been such that a given experiment can be continued for times up to 50 and in some cases 100 horizontal diffusion times, often of the order of a week or more. The experiments in the high-Prandtl-number range have reproduced the Busse balloon in circumstances where straight rolls were originally forced. They also display no time dependence until very large Rayleigh numbers, typically greater than ten times critical, and that behaviour does not occur till after the bimodal state, consisting of the original rolls with rolls at 90° superimposed, is reached. For uncontrolled initial conditions, the evolution of a pattern occurs in two stages. On the horizontal diffusion scale, the pattern consists of circular patches surrounding foci singularities which in rectangular boxes often sit in the corners (see figure 2*f*, *i*). Wavenumber selection is an important part of the dynamics on this timescale. This subject has attracted a lot of attention in the literature and several different mechanisms that select a preferred wavenumber have been proposed. Roll curvature, first suggested by Pomeau & Manneville (1981), is one of the principal mechanisms, and these authors calculated the value of k_B close to threshold for the infinite-Prandtl-number case. Later, Cross & Newell (1984) showed that in the absence of dislocations the functional

$$F = -\int\left(\frac{1}{2}\int^{k^2} B\,\mathrm{d}k^2\right)\mathrm{d}X\,\mathrm{d}Y$$

acts as a Lyapunov functional in the infinite-Prandtl-number case so that it is reasonable to expect the wavenumber in curved patterns to relax to a value as close to the zero k_B of $B(k)$ as the boundary conditions will allow. However, for infinite Prandtl number, the selected wavenumber k_B is at the left-hand edge of the Busse balloon, the zigzag instability boundary, where the rolls lose their resistance to lateral bending. Because of this, the rolls can develop undulations along their axes which scale like $\Gamma^{\frac{1}{2}}d$ (rather than $\Gamma d = L$) and this means higher-order correction terms must be added to (1.1). The earliest timescale on which the pattern can settle down is very long, namely Γ times the horizontal diffusion time. In rectangular geometries it can become stationary as in figure 2(*g*, *j*), whereas in circular geometries it can stay permanently time dependent. This behaviour is consistent with the properties of the phase-diffusion equation (in the infinite-Prandtl-number limit, the mean drift flow is not generated), and is discussed in the original Cross–Newell (1984) paper.

Of more interest to us in this paper is the behaviour at moderate and low Prandtl numbers because it is in these regimes that the mean drift velocity, which in this paper has for the first time been calculated as a functional of the pattern wavevector, is most important. Here we shall give a brief account of some of the experimental observations, relying principally on the articles of Heutmaker & Gollub (1987), Steinberg *et al.* (1985) and Croquette (1989*a*, *b*) who investigated the behaviour at

Prandtl numbers 2.5, 6.1 and 0.71 respectively. Heutmaker & Gollub (1987) investigated convection in water in a cylindrical dish of depth $d = 3$ mm, diameter $L = 41.7$ mm and aspect ratio $\Gamma = L/d$ of about 14. They found three regimes of behaviour. In the first $R < 1.2R_c$, they observed, somewhat surprisingly, that the pattern remains time dependent and aperiodic. This feature was also noted earlier by Ahlers & Behringer (1978) in experiments in liquid helium (P in the range 0.7 to 3) and in very large-aspect-ratio boxes and by Ahlers *et al.* (1985) working with fluids of Prandtl number 5.7. After several horizontal diffusion timescales, the patterns simplify and appear to contain weakly circular roll patches about sidewall foci which are connected to the other part of the lateral walls by grain boundaries. A typical state is shown in figure 2(*a*). Notice that for these low values of $(R-R_c)/R_c$, the roll axes and the boundary normal are not parallel and a significant angle can occur between these two directions. An analysis of the wavenumber band in the pattern shows that a significant portion of the spectrum lies to the left (that is the small-wavenumber side) of the zigzag and cross-roll instability boundaries in the Busse balloon and therefore the appearance of two patches of rolls, roughly at right angles and separated by a grain boundary is not surprising. The shape of the box would seem to have some influence. In a square cell of the same aspect ratio, some of the runs appear to stabilize after 100 horizontal diffusion times.

In the second regime, $1.2R_c < R < 4.5R_c$, the pattern will always stabilize but the final structure may not be unique. Again, in both the rectangular and circular geometries, the textures are dominated by circular patches which (usually) surround sidewall foci. The rolls are more bent and the roll axes are almost everywhere perpendicular to the boundaries. After transients, there would appear to be a minimal number of defects and disclinations which mediate and separate the different circular patches. The pattern takes several horizontal diffusion times to become time independent. The band of wavenumbers is almost wholly contained in the stable portion of the Busse balloon between the zigzag and skew-varicose instability boundaries. Figures 2(*b*) and 2(*c*) are stable patterns. We add one extra observation here from a numerical experiment in a rectangular cell (11.5×16) of Arter & Newell (1988) who found that the finite box length (which limits the range of perturbation wavevectors) tends to push the skew-varicose boundary to slightly larger wavenumbers. Finally, in the third regime, $R > 4.5R_c$, the pattern remains time dependent via repetitive nucleation of dislocation pairs (see figures 2*d* and 2*e*) owing to what appears to be extra wavenumber production at sidewall foci. Although the dynamics is not periodic, it has a quasi-period of about 20–40 vertical diffusion times. The distribution of pattern wavenumbers lies across the skew-varicose instability boundary, namely on the large-wavenumber side of the Busse balloon.

In a pair of articles just published, Croquette (1989*a*, *b*) presents an overview of work with colleagues on low-Prandtl-number convection in cylindrical and rectangular boxes. Part 2 is based on the earlier work of Pocheau, Croquette & Le Gal (1985) and Croquette & Pocheau (1984). In the first part of this work they validate many of the boundaries of the Busse balloon by arranging that the shorter sidewalls are heated so as to negate the usual boundary conditions on these sides and cause the rolls to be almost straight and parallel to this side. Kolodner *et al.* (1986*a*, *b*) have also achieved experimental results consistent with predictions of the Busse balloon. However, as Croquette emphasizes strongly, significantly different behaviour is observed when the convection is allowed to begin spontaneously. He calls the resulting patterns 'natural patterns'. Their experiment investigates the convection patterns in argon gas at a Prandtl number of 0.71 in a cylindrical box of aspect ratios

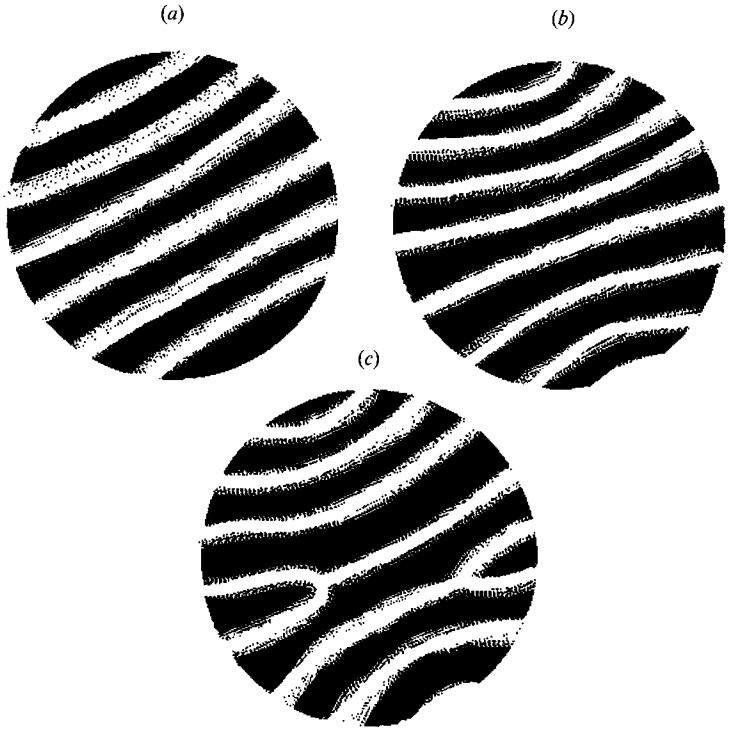

FIGURE 3. Taken from Croquette *et al.* (1986*a*) from an experiment with argon at $P = 0.71$ for an aspect ratio of 7.5. (*a*) A stationary state at $R = 1.05R_c$. (*b*) and (*c*) Approximately $R = 1.13R_c$, showing the patterns being compressed by the roll axes becoming perpendicular to the boundary (*b*) and the resulting nucleation of a dislocation pair (*c*).

7.6 and 20. In the former, the pattern remains stationary until $1.125R_c$ at which point, according to Croquette (1989*a*, *b*), time dependence sets in in the following manner. Very close to onset, the rolls are almost parallel except for two weakly circular patches about two foci singularities on the sidewalls (see figure 3*a*). As the Rayleigh number increases past $1.13R_c$, the boundary condition that the roll axes are parallel to the sidewall normal becomes more important and the inner rolls surrounding each focus become more curved. As a result, the rolls near the centre of the container are compressed (see figure 3*b*) so that their wavenumber crosses the skew-varicose boundary (see figure 1*c*). A defect pair is quickly nucleated; each dislocation climbs swiftly to the sidewall and then glides slowly towards, and eventually disappears in one of the two foci. The timescales for the nucleation and climb portions of this process are a few vertical diffusion times; the gliding takes of the order of the horizontal diffusion time. The surprising thing is that the relief of the stress on the pattern by the action of the dislocations in removing a roll pair does not lead to an equilibrium state. Instead, sidewall foci singularities nucleate new rolls, leading to the same pattern as the original one and the scenario consisting of roll compression, defect nucleation, climb and glide is repeated in an almost periodic cycle. The time dependence in range $1.13R_c < R < 1.16R_c$ appears to be well described by this mechanism, although in this range there are windows of almost periodic, stationary and chaotic behaviours. Periods can be very long and extend up to 100 horizontal diffusion timescales. The effect of increasing the aspect ratio is small. At higher Rayleigh numbers $R > 2R_c$, the patterns in argon become very

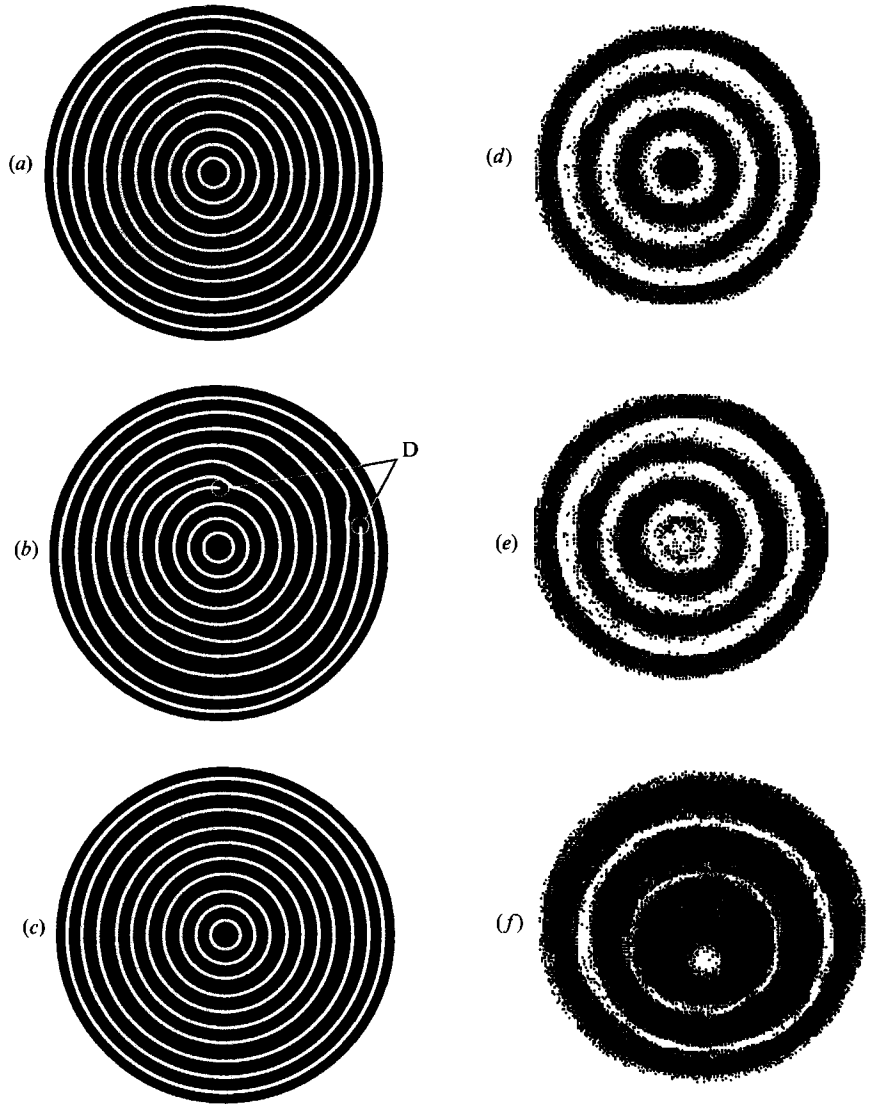

FIGURE 4. (*a*, *b*, *c*) From Croquette (1989) at $P = 0.71$, $R = 1.185R_c$, $\Gamma = 20$, showing the off-centre shift of the umbilicus of a target pattern and the compression of the roll pattern on one side (*a*), followed by the nucleation of a dislocation pair (*b*) which glide one at a time towards and vanish in the umbilicus, leaving a target pattern with one roll pair removed. The umbilicus quickly nucleates new rolls so that the original pattern is reproduced (*c*). The process repeats. (*d*, *e*, *f*) From Steinberg *et al.* (1985) at $P = 6.1$, $\Gamma = 6$ and at several Rayleigh numbers: (*d*) a stable $3\frac{1}{2}$ roll state at $R = 2.5R_c$; (*e*) a stable 3 roll state at $R = 3R_c$, and (*f*) its distortion at $R = 4R_c$. States (*d*), (*e*) and (*f*) are in equilibrium.

complicated, displaying spatially chaotic patterns consisting of many defects which create areas where the local wavenumber is too small, and this would appear to lead to the initiation of local cross-roll instabilities or bridges. On the other hand, there does not seem to be any analogue in the argon experiments of the chaotic behaviour observed by Heutmaker & Gollub (1987) and Ahlers *et al.* (1985) for $R < 1.2R_c$.

A study of the behaviour of circular target patterns was made by Steinberg *et al.* (1985) using aspect ratios of between 6 and 7 and a Prandtl number $P = 6.1$, and by Croquette (1989*a*, *b*) using a Prandtl number of 0.71 for aspect ratios of both 7 and

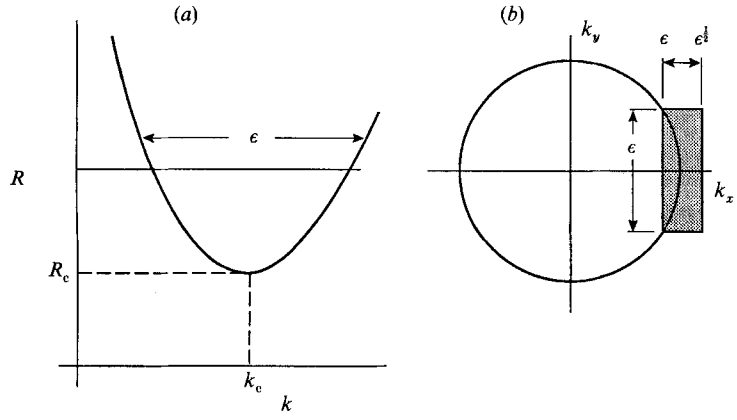

FIGURE 5. The neutral stability curve and the locus of stable wavevectors.

20. They used sidewall forcing to initiate the patterns, although as pointed out by Steinberg *et al.*, it was not necessary to sustain the forcing in order to maintain the circular target patterns. The principal features observed by Steinberg *et al.* were that, as the Rayleigh number increased past a certain value, a perfectly circular target pattern (figure 4*e*) would break its symmetry and reach a new stationary pattern in which its umbilicus (the focus singularity) was shifted off-centre (figure 4*f*). A further increase in Rayleigh number could bring about a transition from a pattern containing 3 roll pairs as in figure 4(*d*) to $2\frac{1}{2}$ roll pairs. At moderate Rayleigh numbers, they found that all these patterns remained stationary. They did notice, however, that the transitions from $3\frac{1}{2}$, to 3, to $2\frac{1}{2}$ roll pairs were hysteretic, namely the change from three to two and a half did not occur at the same value of the Rayleigh number as this parameter was increased as the change from two and a half to three as the Rayleigh number was decreased. Croquette, on the other hand, working at a much lower Prandtl number, observed that the target patterns, while displaying the same symmetry-breaking behaviour, could also sustain a continuing time dependence owing to the repetition of a cycle consisting of a symmetry-breaking bifurcation which compressed the rolls on the side to which the umbilicus moved, followed by the nucleation of a dislocation pair which eventually disappeared by first climbing to the sidewall and then gliding to the focus, followed by the nucleation of new rolls at the focus which brings the pattern back to the original starting point of the cycle.

1.3. *Theory*

1.3.1. *Small-amplitude convection*

Theoretical approaches to describe convection in large boxes fall into two categories. Near threshold, one takes advantage of the small convection amplitudes and expands each of the field variables $w(x, y, z, t)$ in an asymptotic expansion in an amplitude parameter $\epsilon = ((R-R_c)/R_c)^{\frac{1}{2}}$,

$$w(x, y, z, t) = \epsilon w_0 + \epsilon^2 w_1 + \epsilon^3 w_2 + \ldots. \tag{1.8}$$

The shape of w_0 is determined by the linear stability analysis of the conduction solution which yields two important graphs, the neutral stability curve R *vs.* k (independent of Prandtl number) separating regions of exponentially growing from decaying solutions, shown in figure 5(*a*), and the critical circle of wavevectors $\boldsymbol{k}$ at which convection first takes place, shown in figure 5(*b*). Rotational symmetry gives

rise to rotational degeneracy; the stability analysis only determines the modulus k of the wavevector $\boldsymbol{k}$. The shape of w_0 can be taken to be a linear combination of modes:

$$w_0 = \sum_j A_j \phi(z) \exp \mathrm{i}\boldsymbol{k}_j \cdot \boldsymbol{x} + (*), \tag{1.9}$$

where $\boldsymbol{k}_j$ lies either on the critical circle or in an annulus of width ϵ surrounding it and $\phi(z)$, which depends on k, is the vertical structure of the neutrally stable mode. In order to include the temporal evolution of the amplitudes of the motion, we allow A_j to be a slowly varying function of time $T = \epsilon^2 t$ which changes at a rate proportional to $(R - R_c)/R_c$, the growth rate of the instability. For a given value of ϵ^2, equations for the amplitudes are obtained as solvability conditions which must be applied in order to compute the iterates $w_1, w_2, \ldots$ in the expansion (1.8). For $|\boldsymbol{k}_j| = k_c$, $j = 1, \ldots, N$, these equations read

$$\frac{\mathrm{d}A_j}{\mathrm{d}T} = \mu A_j + c_{jmn} A_m^* A_n^* - \sum_{l=1}^{N} \beta_{jl} A_j A_l A_l^*. \tag{1.10}$$

The linear growth term in which μ is proportional to $(R - R_c)/\epsilon^2$ captures the linear instability. The quadratic term arises when the symmetry of the vertical structure $\phi(z)$ about the midplane is weakly broken. This can occur through a variety of non-Boussinesq effects such as weak quadratic variation of density with temperature and dependence of viscosity and other medium parameters on temperature. Mathematically, the term appears because a quadratic product like $\phi(z)\phi'(z) \exp(-\mathrm{i}(\boldsymbol{k}_m + \boldsymbol{k}_n) \cdot \boldsymbol{x})$ has a non-zero projection in another basis mode $\phi(z) \exp(\mathrm{i}\boldsymbol{k}_j \cdot \boldsymbol{x})$ when $\phi(z)\phi'(z)$, because of the slight asymmetry, has a non-zero projection on $\phi(z)$ and $\boldsymbol{k}_j + \boldsymbol{k}_m + \boldsymbol{k}_n = 0$, that is when the three wavevectors are 120° apart on the critical circle. The cubic terms are always present and arise from the projection of $\phi^3(z) \exp[\mathrm{i}(\boldsymbol{k}_j + \boldsymbol{k}_l - \boldsymbol{k}_l) \cdot \boldsymbol{x}]$, $l = 1, \ldots, N$ onto $\phi(z) \exp(\mathrm{i}\boldsymbol{k}_j \cdot \boldsymbol{x})$. These amplitude equations of Stuart–Watson–Landau (1960) type can be used to predict the existence and stability of the various planforms (rolls, $N = 1$; rectangles, $N = 2$ and $\boldsymbol{k}_1 \cdot \boldsymbol{k}_2 = 0$; hexagons, $N = 3$ and $\boldsymbol{k}_1 + \boldsymbol{k}_2 + \boldsymbol{k}_3 = 0$). These amplitude equations were used by Malkus & Veronis (1958), Schülter, Lortz & Busse (1965), Palm (1975), and Segel & Stuart (1962), to compute various measures of the convection fields such as heat flux, and to describe subcritical instabilities (which can arise because of the quadratic terms) of hexagonal form and the competition between the various configurations. For situations in which quadratic terms are absent, the roll solution ($N = 1$) is the only stable configuration.

A new description which automatically includes all the sidebands of a particular mode was suggested by Newell & Whitehead (1969) and Segel (1969). The idea is very simple. All the modes about the wavevector $(k_c, 0)$ contained in the rectangle in figure 5(*b*) and in the band AB in figure 5(*a*) are automatically included if we let

$$w_0 = A(X = \epsilon x, Y = \epsilon^{\frac{1}{2}} y, T = \epsilon^2 t)\, \phi(z) \exp(\mathrm{i}k_c x) + (*). \tag{1.11}$$

The solvability condition at order ϵ^3 gives a partial differential equation for the envelope $A(X, Y, T)$, which, in rescaled form, is

$$\frac{\partial A}{\partial T} - \left(\frac{\partial}{\partial X} - \frac{\mathrm{i}}{2k_c}\frac{\partial^2}{\partial Y^2}\right)^2 A = A - A^2 A^*. \tag{1.12}$$

In deriving (1.12), one assumes that the field consists of long-wavelength modulations of almost straight parallel rolls and that vertical asymmetries are absent. This

envelope equation has been used extensively. It automatically contains two of the long-wavelength instabilities of simple roll solutions

$$A = (1-K^2)^{\frac{1}{2}} e^{iKX} \tag{1.13}$$

found earlier by Busse (1967) (the zigzag instability which occurs if $K < 0$) and Eckhaus (1965) (the Eckhaus instability which occurs if $K^2 > \frac{1}{3}$). The phase diffusion equation (1.4) is also a limit of (1.12) and a little calculation will show that if A is written as $(1-K^2)^{\frac{1}{2}} \exp i(KX+\phi(X,Y,T))$, $D_{\parallel}$ and $D_{\perp}$ are proportional to $1-3K^2$ and K respectively. However Newell & Whitehead and Segel overlooked an effect which, although not important at small values of $(R-R_c)/R$, becomes increasingly important as the Rayleigh number increases. (It is important at small values if stress-free rather than zero tangential velocity boundary conditions are applied at the horizontal boundaries.) This effect, discovered by Siggia & Zippelius (1981*a*, *b*), involves mean currents which are driven by slow gradients in the intensity AA^* and 'along the roll' current density $-i/2k_c(A^*\partial A/\partial Y - A\partial A^*/\partial Y)$. The mean currents, computed from the vertical vorticity $\Omega = (\nabla \times U)\cdot\hat{z}$,

$$\left(-\frac{1}{P}\frac{\partial}{\partial t}+\nabla^2\right)\Omega = -\frac{4}{P}\epsilon\frac{\partial}{\partial Y}\left(\frac{\partial}{\partial X}AA^* - \frac{i}{2k_c}\frac{\partial}{\partial Y}\left(A^*\frac{\partial A}{\partial Y} - A\frac{\partial A^*}{\partial Y}\right)\right), \tag{1.14}$$

in turn advect the phase contours by the addition of $ik_c UA$, $U = (U, \epsilon^{\frac{1}{2}}V)$ to the left-hand side of (1.12). In the case of rigid–rigid boundary conditions, the dominant term on the left-hand side is $\partial^2\Omega/\partial z^2$ and thus Ω and U are of order ϵ and therefore ignorable. For free–free boundary conditions, there is no boundary constraint on Ω, the dominant term on the left-hand side of (1.14) is $\epsilon\partial^2\Omega/\partial Y^2$ and then Ω and U are order one. In this case, one also should include $O(\epsilon^{\frac{1}{2}})$ correction terms to the Siggia–Zippelius expansion in order to bring the stability boundaries into exact agreement with the results obtained by Bolton, Busse & Clever (1986). This last step was carried out by Bernoff (1989).

1.3.2. *Finite-amplitude theories*

One of the main results of the Schülter *et al.* (1965) small-amplitude theory is that among all possible planforms only the two-dimensional configuration consisting of straight, parallel rolls is stable in the Boussinesq approximation. However, as the Rayleigh number is increased, it is clear that the band of wavenumbers which give rise to roll solutions also increases. In a series of fundamental papers spanning a time period of twenty years, and in collaboration with several colleagues, Busse (Busse 1967, 1978, 1981; Busse & Whitehead 1971, 1974; Clever & Busse 1974, 1978, 1979) has provided a comprehensive analysis of the stability of finite-amplitude rolls for almost all values of the Rayleigh and Prandtl numbers and a catalogue of the various instabilities of straight parallel rolls which can occur. He constructed the finite-amplitude roll solutions by expanding the fields in Galerkin series (see §2 of this paper) and obtained nonlinear algebraic equations for their coefficients. He then performed a linear stability analysis of these solutions and in each case identified the ends of the band of stable wavenumbers and the mode of instability that occurred there. The stability regions are shown schematically in figure 1 for several values, high, moderate and low, of the Prandtl number. Each stability region is called a Busse balloon. The superposition of these regions in the Rayleigh number, wavenumber, Prandtl number space could be called the Busse windsock. Although the Busse balloon only outlines the stability region for a field of straight parallel rolls in an infinite horizontal geometry, it has proven to be extremely valuable in understanding

many of the qualitative features seen in convection in finite but large boxes. However, since the preponderance of observational evidence suggested that convection patterns are only straight rolls locally and are much more complicated when viewed globally, it was necessary to build a theory appropriate for curved roll patterns and this step was taken by Cross & Newell (1984).

The fundamental idea of the Cross–Newell approach followed naturally from the work of Whitham (1974) on almost periodic wavetrains in nonlinear dispersive systems. It was also used by Howard & Kopell (1977) in their investigations of spiral wave patterns in reaction–diffusion systems. It is different from the work of Pomeau & Manneville (1979) in the fact that the total wavenumber and not just a small perturbation to it is allowed to change significantly. Indeed, the Pomeau–Manneville equation is the Newell–Whitehead–Segel equation (1.12) obtained by taking $A = A_0 \exp(iKx + i\Theta)$ in (1.12) and assuming that the amplitude A_0 is slaved to the phase gradient, i.e. $A_0^2 = 1 - K^2$. Then,

$$\Theta_T - \frac{1-3K^2}{1-K^2}\Theta_{XX} - \frac{K}{k_c}\Theta_{yy} = 0.$$

Nevertheless, it should be emphasized that whereas the equation that Pomeau & Manneville derived had this limitation, they understood conceptually the role of a phase diffusion equation in describing finite-amplitude patterns in rotationally invariant systems. They also derived the phase diffusion equation for the perturbation to a patch of low-amplitude circular rolls and used it to show how a wavenumber would be selected. Their approach was continued to the finite-amplitude regime by Buell & Caton (1986), who in a very non-trivial piece of work, calculated what we call k_B. The Cross–Newell work, however, was the first to write down rotationally invariant phase diffusion and mean drift equations for a finite-amplitude system. We now describe the basic idea.

The basic premise of this theory is that, except at singularities, the field locally consists of spatially periodic, straight parallel rolls whose wavevector $\boldsymbol{k}$ gives the local wavenumber and roll direction. The wavevector $\boldsymbol{k}$ changes slowly, that is over distances compared with the box size L, whereas the fields themselves change significantly over a roll wavelength, that is on distances proportional to d, the layer depth. The small parameter ϵ in this theory is not $((R-R_c)/R_c)^{\frac{1}{2}}$ but rather Γ^{-1}, the inverse aspect ratio. We distinguish between two regimes of ϵ. For ϵ sufficiently large, the allowed set of wavenumbers will populate the nonlinear stability region (the Busse balloon) densely. From figure 1 we see that this width is about 1.5 and, if we define dense to mean that this band is revolved by ten k values, then

$$\epsilon = \frac{d}{L} \approx \frac{2\pi}{k_c L} = \frac{\Delta k}{k_c} = \frac{0.15}{3.1} \approx 0.05.$$

We refer to an $\epsilon < 0.05$ as a large-aspect-ratio situation (at least twenty rolls in the container) and $0.05 < \epsilon < 0.2, 0.3$ as a moderate-aspect-ratio situation. Although the patterns, when viewed on the global scale, are far from being straight rolls, the fact that they have this structure locally allows us to build solutions that are slow modulations of the finite-amplitude solutions of Busse. Each field variable w is approximated as a function of depth z and a phase variable θ,

$$w = f(\theta, z; A), \tag{1.15}$$

which, if the rolls were straight and parallel, would be an exact solution with $\theta = \boldsymbol{k} \cdot \boldsymbol{x}$, $\boldsymbol{k}$ constant. The imposition of 2π periodicity on f gives a relation between

k and A, a measure of the field amplitude, and the other parameters such as the Rayleigh and Prandtl numbers, R and P respectively,

$$\Omega(k, A; R, P) = 0. \tag{1.16}$$

When $\boldsymbol{k}$ is slowly varying, the phase variable θ is written as

$$\theta = \frac{1}{\epsilon}\Theta(X, Y, T) = \frac{1}{\epsilon}\int \boldsymbol{k}(X, Y, T)\cdot \mathrm{d}\boldsymbol{X}, \tag{1.17}$$

where $X = \epsilon x$, $Y = \epsilon y$, $T = \epsilon^2 t$. Also (1.15) is no longer an exact solution but only an approximation to the field $w(\boldsymbol{x}(x, y), z, t)$, which we now write

$$w(\boldsymbol{x}, z, t) = f(\theta, z; A) + \epsilon w_1 + \epsilon^2 w_2 + \ldots. \tag{1.18}$$

The iterates $w_1, w_2, \ldots$ are calculated by linearizing the governing equations about the fully nonlinear solution $f(\theta, z; A)$. The solvability conditions for the iterates give us equations for the slowly varying wavevector $\boldsymbol{k}$, called the phase diffusion equation, and a depth-averaged mean drift velocity field $\boldsymbol{V}$. The amplitude A will turn out to satisfy the same algebraic equation (1.16) as it did at leading order but there will be higher-order corrections which depend on gradients of the wavevector field. These corrections only become important close to onset, that is for values of R close to R_c, or at isolated singularities in the field where the amplitude is no longer slaved to k and approaches zero.

The solvability conditions arise because the Oberbeck–Boussinesq equations, when linearized about the nonlinear solution $f(\theta, z; A)$, have non-trivial solutions. The first of these corresponds to translational invariance of the phase; if $f(\theta, z; A)$ is a solution, so is $f(\theta + \theta_0, z; A)$ and thus f_θ satisfies the linearized homogeneous equation. At small amplitudes, the amplitude A is also a free parameter, it is not restricted by (1.16), and therefore there is a continuous one-parameter family of solutions whose 'symmetry' $\partial f/\partial A$ also satisfies the linearized homogeneous equations. The presence of a non-trivial solution of the linearized boundary-value problem means that the adjoint problem will also have a non-trivial solution and that the right-hand sides of the equations for $w_1, w_2, \ldots$ etc., which depend on the slow time and space derivatives of $\boldsymbol{k}$ and A, will have to satisfy the Fredholm alternative theorem. The translational invariance of the phase gives rise to the phase diffusion equation. At small amplitudes, the one-parameter family of amplitude-free solutions gives rise to another constraint, a partial differential equation for the amplitude A. When written together as a complex amplitude A, e.g. $A \exp i\theta \rightarrow$ complex A, these equations become the Newell–Whitehead–Segel equations (1.12). However, at larger amplitudes, the second symmetry is absent and the equation for amplitudes is replaced by the algebraic equation (1.16), a result of demanding spatial periodicity of the finite-amplitude solution. Away from onset, therefore, amplitudes are slaved to phase gradients (A is an algebraic function of k), and only phase diffusion matters. Near defect singularities, this slaving no longer occurs, and, at the defect, the amplitude attains a zero value. These points, of zero measure with respect to area, must be handled separately, although we shall suggest that certain weak solutions of the phase diffusion equation may still apply.

There is also another symmetry, which is simply that the pressure field of the nonlinear solution contains a free constant, independent of the depth and horizontal coordinates. The solvability condition arising from this symmetry says that the divergence of the velocity field averaged over the depth and the horizontal period must be zero. However, as we have already indicated, the quadratic nonlinearities in

the momentum equation can give rise to Reynolds stresses which drive large-scale mean flows whose average over θ and z does not necessarily satisfy continuity. In order to ensure that they do, a slowly varying pressure field must be introduced, namely the constant pressure in the nonlinear solution must be taken as a slowly varying function of time and the horizontal coordinates.

The major difficulty in deriving the phase diffusion (1.1) and mean drift flow equations (1.2) from the Oberbeck–Boussinesq equation is that the latter equation first arises as a non-trivial solvability condition at order ϵ^2 whereas the former is a solvability condition at order ϵ. Further, the mean velocity field, which is order ϵ and generated as part of w_1, depends also on the fluctuating (θ-dependent) part of the solution w_1. Therefore we must apply the solvability condition at order ϵ to obtain the phase diffusion equation, and then solve the remaining part of this equation for w_1 before we can get to the solvability condition at order ϵ^2. In practice this is very difficult because the coefficients of the equations as functions of wavenumber k must be determined numerically (although their structure in terms of the direction of the vector $\boldsymbol{k}$ can be found analytically) and therefore the terms remaining on the right-hand side of the equation for w_1 do not quite satisfy the Fredholm alternative theorem, which is the solvability condition for this equation. One therefore needs a robust method of solution, a means of inverting the non-homogeneous equation for w_1 that is relatively insensitive to these errors. It turns out that there is such a scheme, based on the singular-valued decomposition of the singular matrix which is the representation of the differential operator acting on w_1 in some chosen basis. Using this, we are able to solve for the perturbed field w_1 very accurately and then use this information to construct the mean drift velocity equation as the solvability equation of order ϵ^2. What turns out to be surprising is that the vertical structure of the horizontally averaged (over θ) horizontal velocity field is quite complicated and, especially at low Prandtl numbers, depends crucially on the pattern structure in addition to the slowly varying pressure field which is created in order to assure that mass conservation is satisfied. At moderate to large Prandtl numbers, this field is approximately parabolic, having the shape that one expects from the presence of a depth-independent, slowly varying pressure gradient. Indeed if one ignores the vertical Reynolds stresses, the terms $(\partial/\partial z)\,\overline{uw}$, $(\partial/\partial z)\,\overline{vw}$ in the horizontally averaged momentum equations (u, v, w are the velocity components, overbar denotes average over θ), the mean drift profile would have a Poiseuille-like shape. However, at moderate ($P \sim 2.5$) to low Prandtl numbers, the vertical Reynolds stresses are as important as the slowly varying horizontal Reynolds stresses,

$$\frac{\partial}{\partial X}\overline{u}^2+\frac{\partial}{\partial Y}\overline{uv}, \quad \frac{\partial}{\partial X}\overline{uv}+\frac{\partial}{\partial Y}\overline{v}^2$$

and greatly change the vertical profile of the mean drift flow.

1.4. *The outline of the paper*

In §2, we give the mathematical formulation and derivation of the phase and mean drift equations. We use two formulations, the momentum equations which include the pressure and the vorticity equations in which the pressure is eliminated. The latter calculation is written out explicitly in Appendix A. The reason for emphasizing the former is that the slowly varying, depth-independent, components of pressure plays a very important role in controlling the mean drift velocity field and ensuring mass conservation over large scales. In order to make the account as readable as possible, details of the consistency of different approaches and the numerical

procedures are postponed to Appendices B and C. Section 3 discusses the results. In §3.1, we reproduce the long-wave stability borders of the Busse balloon and integrate a pattern undergoing the skew-varicose instability to a finite-amplitude state. In §3.2, we discuss circular roll patterns and introduce the focus instability. A combination of this instability and the skew-varicose instability provides a mechanism for wavenumber adjustment and may also be important in inducing time dependence. We discuss scenarios for the onset of time dependence in §3.3. In the Conclusion, we discuss how to introduce the amplitude as an active order parameter near singularities and review some open problems.

2. Mathematical formulation and derivation of the phase diffusion and mean drift equations

2.1. *Governing equations*

The governing equations are a combination of the Navier–Stokes and heat equations in which one assumes that density changes are linearly proportional to temperature changes and ignores all density fluctuations except where they appear in the buoyancy force. This is called the Oberbeck–Boussinesq approximation. Length is scaled with the depth d of the layer, time by d^2/κ where κ is the thermometric conductivity, velocity by κ/d and temperature by $\nu\kappa/\alpha g d^3$ where ν is the fluid viscosity, g gravity and α the coefficient of cubic expansion. The temperature difference across the layer is ΔT which in non-dimensional units is called the Rayleigh number

$$R = \frac{\alpha g d^3 \Delta T}{\kappa \nu}. \tag{2.1}$$

The other parameter that appears in the equation is the Prandtl number P, the ratio of viscous to thermal diffusivity, which we write as σ^{-1}. For values of R less than 1708, the conductive state

$$\boldsymbol{u}_c = 0, \quad T_c = -Rz + T_0, \quad \frac{\mathrm{d}p_c}{\mathrm{d}z} = -T_c(z), \tag{2.2}$$

consisting of a zero velocity field and a linear temperature gradient, is stable. In non-dimensional form, the equations for the velocity field $\boldsymbol{u}$ and the fluctuation of the temperature T and pressure p fields about the conduction solutions are

$$\sigma\left(\frac{\partial \boldsymbol{u}}{\partial t} + (\boldsymbol{u}\cdot\boldsymbol{\nabla})\boldsymbol{u}\right) = -\boldsymbol{\nabla}p + T\hat{\boldsymbol{z}} + \boldsymbol{\nabla}^2\boldsymbol{u}, \tag{2.3}$$

$$\frac{\partial T}{\partial t} + \boldsymbol{u}\cdot\boldsymbol{\nabla}T - Rw = \boldsymbol{\nabla}^2 T, \tag{2.4}$$

$$\boldsymbol{\nabla}\cdot\boldsymbol{u} = 0, \tag{2.5}$$

where the velocity field $\boldsymbol{u}$ has components (u, v, w). We shall also find it useful to work with the vorticity equation in which the pressure force is eliminated,

$$\sigma\left(\frac{\partial \boldsymbol{\omega}}{\partial t} + (\boldsymbol{u}\cdot\boldsymbol{\nabla})\boldsymbol{\omega} - (\boldsymbol{\omega}\cdot\boldsymbol{\nabla})\boldsymbol{u}\right) = \boldsymbol{\nabla}T\times\hat{\boldsymbol{z}} + \boldsymbol{\nabla}^2\boldsymbol{\omega}, \tag{2.6}$$

with $\boldsymbol{\omega} = \boldsymbol{\nabla}\times\boldsymbol{u} = (\xi, \eta, \zeta)$.

The boundary conditions are

$$\boldsymbol{u} = T = 0 \quad \text{at} \quad z = \pm\tfrac{1}{2}, \tag{2.7}$$

reflecting the fact that the horizontal boundaries are rigid and isothermal. For the approximation in which we consider an infinite horizontal layer of fluid, we simply ask that both fields are bounded as $x,\ y \to \pm\infty$.

2.2. *Steady roll solutions*

We have already indicated that the starting point for the theory is a field of straight parallel rolls, periodic in the horizontal direction with wavevector $\boldsymbol{k}$ and wavelength $\lambda = 2\pi/k, k = |\boldsymbol{k}|$. There is no loss of generality in taking $\boldsymbol{k}$ to be $(k, 0)$, that is the roll axes are parallel to the y-direction. In constructing these solutions by a Galerkin scheme, we follow Busse (1967), and write

$$u = \sum_{m,n} u_{mn}\, \mathrm{e}^{\mathrm{i}m\theta} g_n'(z), \tag{2.8}$$

$$w = \sum_{m,n} w_{mn}\, \mathrm{e}^{\mathrm{i}m\theta} g_n(z), \tag{2.9}$$

$$T = \sum_{m,n} T_{mn}\, \mathrm{e}^{\mathrm{i}m\theta} f_n(z), \tag{2.10}$$

$$p = \sum_{m,n} p_{mn}\, \mathrm{e}^{\mathrm{i}m\theta} h_n(z) + p_{\mathrm{s}} = p_0 + p_{\mathrm{s}}, \tag{2.11}$$

where p_{s} is a free constant. The summations in (2.8)–(2.11) are over $1 \leqslant n \leqslant N$, $-M \leqslant m \leqslant M$. The argument θ in the exponential is $\boldsymbol{k} \cdot \boldsymbol{x} = kx$ since we have taken $\boldsymbol{k} = (k, 0)$. The functions which carry the vertical structure of the velocity fields are approximations of the eigenfunctions of the operator which arises in investigating the linear stability of the conductive state. They are given by the formulae (see Chandrasekhar 1961)

$$\begin{aligned} g_n(z) &= \frac{\sinh \mu_n z}{\sinh \tfrac{1}{2}\mu_n} - \frac{\sin \mu_n z}{\sin \tfrac{1}{2}\mu_n}, \quad n \text{ even}, \\ &= \frac{\cosh \lambda_n z}{\cosh \tfrac{1}{2}\lambda_n} - \frac{\cos \lambda_n z}{\cos \tfrac{1}{2}\lambda_n}, \quad n \text{ odd}, \end{aligned} \tag{2.12}$$

with μ_n, λ_n the positive roots of $\coth \tfrac{1}{2}\mu = \cot \tfrac{1}{2}\mu$ and $\tanh \tfrac{1}{2}\lambda = \tan \tfrac{1}{2}\lambda$ respectively. The vertical structure of the temperature field and the pressure field are written in the bases

$$f_n(z) = \sin(n\pi(z+\tfrac{1}{2})), \quad h_n(z) = \cos(n\pi(z+\tfrac{1}{2})). \tag{2.13}$$

Reality and symmetry about the planes $z = 0$, $x = 0$ require u_{mn} to be pure imaginary and w_{mn}, T_{mn}, p_{mn} to be real. We may write $u_{mn} = \mathrm{i}\, U_{mn}$, with $U_{-mn} = U_{mn}$ and then, from continuity (2.5), $w_{mn} = kmU_{mn}$. The vorticity $\boldsymbol{\omega}$ of the basic roll pattern is $(0, \eta, 0)$ with

$$\eta = \sum_{m,n} \mathrm{i}\, U_{mn}\, \mathrm{e}^{\mathrm{i}m\theta}(g_n''(z) - k^2 m^2 g_n(z)). \tag{2.14}$$

Substituting (2.8)–(2.11), (2.14) into (2.3), (2.4), (2.5) and (2.6) will give us a system of nonlinear algebraic equations for the coefficients U_{mn}, T_{mn} and p_{mn} obtained by projecting the horizontal momentum, the vertical momentum, and heat equations onto the basis functions $\mathrm{e}^{\mathrm{i}m\theta} g_n'(z)$, $\mathrm{e}^{\mathrm{i}m\theta} g_n(z)$ and $\mathrm{e}^{\mathrm{i}m\theta} f_n(z)$ respectively. These equations admit solutions for which all coefficients whose indices m and n sum to an odd number are zero, and these are the finite-amplitude roll solutions of interest. The choice of basis functions $\{h_n = \cos n\pi(z+\tfrac{1}{2})\}$ for the pressure field proves to be better

than $\{g_n'(z)\}$ which, at first glance at the horizontal momentum equation, might appear more natural. The reason for this is that the pressure field is not constrained to be zero at the boundaries and using a basis which forces this only leads to a Gibbs-like behaviour near $z = \pm\frac{1}{2}$.

A Newton's method is used to obtain the solution of the system of nonlinear algebraic equations. We found it convenient to obtain a first approximation to the solution by solving for the coefficients iteratively in terms of the amplitude A of the lowest mode $g_1(z)\,e^{i\theta}$. Convergence was tested by checking the value of the Nusselt number and comparing the results with those of Clever & Busse (1974, 1979). In this way, we obtain a set of solutions that depend on the parameters R, σ and k. Since it is important to know the fields and many of their global integrals, such as the heat flux, as a function of continuous k, we first solved the system of nonlinear algebraic equations for a discrete set of values spanning the interval of interest (determined by the marginal stability of the conduction solution) and then interpolated the fields using cubic spline polynomials so as to be able to compute their k-derivatives. It is important to stress that the solution of the system of nonlinear algebraic equations gives us a relation between R, σ, k and some measure A (e.g. square root of heat flux) of the solution amplitude.

The finite-amplitude roll solution has two free parameters: θ_0, an arbitrary translation of phase; and p_s, the constant pressure. Each gives rise to a symmetry in the sense that the derivative of the finite-amplitude solution with respect to either θ_0 or p_s is a solution of the linear homogeneous equation obtained by perturbing the system about the finite-amplitude roll solution.

2.3. *Modulated roll solution*

We next look for modulated roll solutions by seeking approximate solutions for each of the dependent variables $\boldsymbol{v} = (\boldsymbol{u}, T, p)$ in the form

$$\boldsymbol{v} = \boldsymbol{f}\left(\theta = \frac{\Theta(X, Y, T)}{\epsilon}, z; A(X, Y, T)\right), \tag{2.15}$$

where

$$X = \epsilon x, \quad Y = \epsilon y, \quad T = \epsilon^2 t \tag{2.16}$$

and ϵ, $0 < \epsilon \ll 1$, is the inverse aspect ratio $\Gamma^{-1} = d/L$, the horizontal scale over which we expect the pattern wavevector

$$\boldsymbol{k} = \boldsymbol{\nabla}_x \theta = \boldsymbol{\nabla}_X \Theta \tag{2.17}$$

to change. We also allow the hitherto constant pressure field p_s to depend on X, Y and T. The relevant timescale will be $(1/\epsilon^2)\,d^2/\kappa = L^2/\kappa$, the horizontal diffusion scale. Because of the slow modulation, the expression (2.15) with $\boldsymbol{f}$ given by the steady roll state of §2.2 is no longer an exact solution of the Oberbeck–Boussinesq equations. We therefore seek solutions in the form of an asymptotic expansion in ϵ,

$$\boldsymbol{v} = \boldsymbol{v}_0 + \epsilon \boldsymbol{v}_1 + \epsilon^2 \boldsymbol{v}_2 + \ldots, \tag{2.18}$$

where

$$\boldsymbol{v}_0\left(\theta = \frac{\Theta(X, Y, T)}{\epsilon}, z; A(X, Y, T)\right),$$

as a function of θ and z is exactly the steady parallel roll state. However,

$$\frac{\partial \boldsymbol{v}_0}{\partial x} = \frac{\partial \boldsymbol{v}_0}{\partial \theta}\frac{\partial \theta}{\partial x} + \epsilon \frac{\partial \boldsymbol{v}_0}{\partial X} = \left(k_1 \frac{\partial}{\partial \theta} + \epsilon \frac{\partial}{\partial X}\right)\boldsymbol{v}_0,$$

where k_1 is the x-component of the slowly varying wavevector $\boldsymbol{k}$. Therefore, when acting on a function of $\theta, z, \boldsymbol{X} = (X, Y), T$,

$$\left.\begin{aligned} &\frac{\partial}{\partial z} \to \frac{\partial}{\partial z}, \\ &\boldsymbol{\nabla}_x \to \boldsymbol{k}\frac{\partial}{\partial \theta} + \epsilon \boldsymbol{\nabla}_X, \quad \boldsymbol{k} = (k_1, k_2), \\ &\frac{\partial}{\partial t} \to \epsilon \Theta_T \frac{\partial}{\partial \theta} + \epsilon^2 \frac{\partial}{\partial T}, \\ &\nabla^2 \to k^2 \frac{\partial^2}{\partial \theta^2} + \frac{\partial^2}{\partial z^2} + \epsilon D \frac{\partial}{\partial \theta} + \epsilon^2 \nabla_X^2, \end{aligned}\right\} \tag{2.19}$$

where

$$D = 2\boldsymbol{k} \cdot \boldsymbol{\nabla}_X + \boldsymbol{\nabla}_X \cdot \boldsymbol{k}. \tag{2.20}$$

Our goal is to choose slow dependence of the wavevector $\boldsymbol{k}(X, Y, T)$ and pressure $p_s(X, Y, T)$ (or equivalently, the mean drift horizontal velocity field which it drives) fields in order to keep (2.18) a uniform asymptotic expansion, i.e.

$$\left| v - \sum_{l=0}^{m} \epsilon^l v_l \right| = o(\epsilon^m), \quad \text{for all} \quad m, X, Y, T.$$

The perturbation equations for u_1, v_1, w_1, T_1 and p_1 are

$$\left(k^2\frac{\partial^2}{\partial\theta^2} + \frac{\partial^2}{\partial z^2}\right)u_1 - 2\sigma k_1 \frac{\partial}{\partial\theta}u_0 u_1 - \sigma k_2 \frac{\partial}{\partial\theta}(u_0 v_1 + u_1 v_0) - \sigma\frac{\partial}{\partial z}(u_0 w_1 + u_1 w_0) - k_1\frac{\partial p_1}{\partial\theta}$$

$$= \sigma\Theta_T\frac{\partial u_0}{\partial\theta} - D\frac{\partial u_0}{\partial\theta} + \sigma\frac{\partial}{\partial X}u_0^2 + \sigma\frac{\partial}{\partial Y}u_0 v_0 + \frac{\partial p_0}{\partial X} + \frac{\partial p_s}{\partial X}, \tag{2.21}$$

$$\left(k^2\frac{\partial^2}{\partial\theta^2} + \frac{\partial^2}{\partial z^2}\right)v_1 - \sigma k_1 \frac{\partial}{\partial\theta}(u_0 v_1 + u_1 v_0) - 2\sigma k_2 \frac{\partial}{\partial\theta}v_0 v_1 - \sigma\frac{\partial}{\partial z}(v_0 w_1 + v_1 w_0) - k_2\frac{\partial p_1}{\partial\theta}$$

$$= \sigma\Theta_T\frac{\partial v_0}{\partial\theta} - D\frac{\partial v_0}{\partial\theta} + \sigma\frac{\partial}{\partial X}u_0 v_0 + \sigma\frac{\partial}{\partial Y}v_0^2 + \frac{\partial p_0}{\partial Y} + \frac{\partial p_s}{\partial Y}, \tag{2.22}$$

$$\left(k^2\frac{\partial^2}{\partial\theta^2} + \frac{\partial^2}{\partial z^2}\right)w_1 - \sigma k_1 \frac{\partial}{\partial\theta}(u_0 w_1 + u_1 w_0) - \sigma k_2 \frac{\partial}{\partial\theta}(v_0 w_1 + v_1 w_0) - 2\sigma\frac{\partial}{\partial z}w_0 w_1 + T_1 - \frac{\partial p_1}{\partial z}$$

$$= \sigma\Theta_T\frac{\partial w_0}{\partial\theta} - D\frac{\partial w_0}{\partial\theta} + \sigma\frac{\partial}{\partial X}u_0 w_0 + \sigma\frac{\partial}{\partial Y}v_0 w_0, \tag{2.23}$$

$$\left(k^2\frac{\partial^2}{\partial\theta^2} + \frac{\partial^2}{\partial z^2}\right)T_1 - k_1\frac{\partial}{\partial\theta}(u_0 T_1 + u_1 T_0) - k_2\frac{\partial}{\partial\theta}(v_0 T_1 + v_1 T_0) - \frac{\partial}{\partial z}(w_0 T_1 + w_1 T_0) + R w_1$$

$$= \Theta_T\frac{\partial T_0}{\partial\theta} - D\frac{\partial T_0}{\partial\theta} + \sigma\frac{\partial}{\partial X}u_0 T_0 + \sigma\frac{\partial}{\partial Y}v_0 T_0, \tag{2.24}$$

$$k_1\frac{\partial}{\partial\theta}u_1 + k_2\frac{\partial}{\partial\theta}v_1 + \frac{\partial w_1}{\partial z} = -\frac{\partial u_0}{\partial X} - \frac{\partial v_0}{\partial Y}, \tag{2.25}$$

$$k_1\frac{\partial}{\partial\theta}u_2 + k_2\frac{\partial}{\partial\theta}v_2 + \frac{\partial w_2}{\partial z} = -\frac{\partial u_1}{\partial X} - \frac{\partial v_1}{\partial Y}. \tag{2.26}$$

For reasons that we are about to discuss we include both the order ϵ and ϵ^2 contributions in the continuity equation.

We seek solutions $\boldsymbol{v}_j = (u_j, v_j, w_j, T_j, p_j)$, $j = 1, 2, \ldots$ to these equations which are periodic in θ and satisfy the no-slip $\boldsymbol{u}_j = 0$ and isothermal $T_j = 0$ boundary conditions on $z = \pm\frac{1}{2}$. The presence of the free parameter θ_0 in the phase means that there exists a non-trivial solution $\partial \boldsymbol{v}_0/\partial\theta$ to the homogeneous equations obtained by ignoring the right-hand sides of (2.21)–(2.25). This means that in order for (2.21)–(2.25) to have a solution, the right-hand sides must satisfy a certain solvability or compatibility condition. In order to find this condition, we are obliged to solve the homogeneous adjoint boundary-value problem to (2.21)–(2.25) (we write down its form in the next subsection). This condition becomes the phase diffusion equation and it describes how the phase $\Theta(X, Y, T)$ and its gradient, the wavevector $\boldsymbol{k}(X, Y, T)$, evolve under the combined influences of phase diffusion and slowly varying mean drift fields. The mean drift field arises because there is a second solvability condition (we checked numerically that there are only two) which results from the presence of the arbitrary parameter p_s and corresponds to mass conservation. It is easy to see that the almost trivial vector $\boldsymbol{v} = (u = v = w = T = 0, p = 1)$ satisfies the homogeneous equations and boundary conditions and also those of the adjoint problem. Therefore the solvability condition arising from this solution is obtained by multiplying (2.21)–(2.25) by 0, 0, 0, 0 and 1 and averaging over θ and z. It is clear that this condition is simply mass conservation. At order ϵ, namely in (2.25), it gives a trivial result as averaging u_0 and v_0 over θ and z automatically gives zero. However, at order ϵ^2, the condition is not trivial because the perturbed fields u_1 and v_1 pick up non-periodic components due to the slow horizontal Reynolds stresses

$$\sigma\frac{\partial}{\partial X}u_0^2 + \sigma\frac{\partial}{\partial Y}u_0 v_0 \quad \text{and} \quad \sigma\frac{\partial}{\partial X}u_0 v_0 + \sigma\frac{\partial}{\partial Y}v_0^2$$

in (2.21), (2.22).

In order to apply the second condition, one has to apply first the solvability condition at order ϵ and then solve for the θ-independent components of the horizontal velocity fields. Once these are known, we find the second solvability condition by averaging the horizontal momentum equations over θ to give

$$\frac{\partial^2 \bar{u}_1}{\partial z^2} = \sigma\frac{\partial}{\partial z}\overline{u_0 w_1 + u_1 w_0} + \sigma\frac{\partial}{\partial X}\bar{u}_0^2 + \sigma\frac{\partial}{\partial Y}\overline{u_0 v_0} + \frac{\partial p_s}{\partial X}, \tag{2.27}$$

$$\frac{\partial^2 \bar{v}_1}{\partial z^2} = \sigma\frac{\partial}{\partial z}\overline{v_0 w_1 + v_1 w_0} + \sigma\frac{\partial}{\partial X}\overline{u_0 v_0} + \sigma\frac{\partial}{\partial Y}\bar{v}_0^2 + \frac{\partial p_s}{\partial Y}, \tag{2.28}$$

and then over z. This second average removes the vertical Reynolds stresses because they are zero on boundaries. However, their presence significantly alters the vertical profile of $\bar{u}_1$ and $\bar{v}_1$, the θ-independent component of the perturbed field; and therefore they contribute to the horizontal stresses $\partial\bar{u}_1/\partial z$ and $\partial\bar{v}_1/\partial z$ at the boundaries $z = \pm\frac{1}{2}$. We obtain

$$\left\langle\frac{\partial^2 u_1}{\partial z^2}\right\rangle = \left[\frac{\partial \bar{u}_1}{\partial z}\right]_{-\frac{1}{2}}^{\frac{1}{2}} = \sigma\frac{\partial}{\partial X}\langle u_0^2\rangle + \sigma\frac{\partial}{\partial Y}\langle u_0 v_0\rangle + \frac{\partial p_s}{\partial X}, \tag{2.29}$$

$$\left\langle\frac{\partial^2 v_1}{\partial z^2}\right\rangle = \left[\frac{\partial \bar{v}_1}{\partial z}\right]_{-\frac{1}{2}}^{\frac{1}{2}} = \sigma\frac{\partial}{\partial X}\langle u_0 v_0\rangle + \sigma\frac{\partial}{\partial Y}\langle v_0^2\rangle + \frac{\partial p_s}{\partial Y}. \tag{2.30}$$

In (2.27)–(2.30), the overbar means an average over θ,

$$\bar{f}(z) = \frac{1}{2\pi}\int f(\theta, z)\,\mathrm{d}\theta, \tag{2.31}$$

the angle brackets $\langle\ \rangle$ denote averages over both θ and z,

$$\langle f\rangle = \frac{1}{2\pi}\int_{-\frac{1}{2}}^{\frac{1}{2}} \mathrm{d}z \int f(\theta, z)\,\mathrm{d}\theta, \tag{2.32}$$

and the square brackets,

$$[f(z)]_{-\frac{1}{2}}^{\frac{1}{2}} = f(\tfrac{1}{2}) - f(-\tfrac{1}{2}),$$

means the difference in the value of $f(z)$ at the upper and lower boundaries. The solvability condition at order ϵ^2 tells us that

$$\frac{\partial}{\partial X}\langle u_1\rangle + \frac{\partial}{\partial Y}\langle v_1\rangle = 0, \tag{2.33}$$

a condition which is enforced by the introduction of a mean drift stream function $\psi(X, Y, T)$,

$$\langle u_1\rangle = \frac{\partial \psi}{\partial Y}, \quad \langle v_1\rangle = -\frac{\partial \psi}{\partial X}. \tag{2.34}$$

The solvability condition is obtained by eliminating p_s from (2.29), (2.30), expressing the left-hand sides of the equations in terms of ψ and obtaining a single equation (1.2) which links the mean drift stream function $\psi(X, Y, T)$ with derivatives of the phase function $\Theta(X, Y, T)$. However, before we can achieve this in a concrete way, we must know the vertical (z) structure of the θ-independent horizontal velocity fields $\bar{u}_1$ and $\bar{v}_1$, and this we must obtain by solving (2.21)–(2.25) after first applying the solvability condition which gives rise to the phase diffusion equation (1.1).

So our task now is to effect this calculation. There are many non-trivial steps in the process, so in first presenting them we shall avoid as much of the detail as possible and postpone the discussion of particulars plus the many crosschecks we used to the Appendices. The first step is to introduce cross-roll along-the-roll horizontal velocities

$$\left.\begin{aligned} \tilde{u} &= \hat{\boldsymbol{k}}\cdot\boldsymbol{u} = \hat{k}_1 u + \hat{k}_2 v, \\ \tilde{v} &= (\hat{\boldsymbol{k}}\times\boldsymbol{u})\cdot\hat{\boldsymbol{z}} = -\hat{k}_2 u + \hat{k}_1 v, \end{aligned}\right\} \tag{2.35}$$

where $\hat{\boldsymbol{k}}$ is a unit vector having the direction of the local wavevector $\boldsymbol{k}$ and $\boldsymbol{u} = (u, v)$. In particular, since $\tilde{v}_0 = 0$, we can invert (2.35) to obtain $u_0 = \hat{k}_1\tilde{u}_0$, $v_0 = \hat{k}_2\tilde{u}_0$, where $\tilde{u}_0$ is the horizontal velocity of the straight parallel roll solution (2.8). Using this notation, the averaged horizontal Reynolds stresses can be expressed as

$$\sigma\begin{bmatrix} \dfrac{\partial}{\partial X}\langle u_0^2\rangle + \dfrac{\partial}{\partial Y}\langle u_0 v_0\rangle \\ \dfrac{\partial}{\partial X}\langle u_0 v_0\rangle + \dfrac{\partial}{\partial Y}\langle v_0^2\rangle \end{bmatrix} = \sigma\boldsymbol{k}\boldsymbol{\nabla}\cdot\boldsymbol{k}\frac{\langle\tilde{u}_0^2\rangle}{k^2} + \tfrac{1}{2}\sigma\frac{\langle\tilde{u}_0^2\rangle}{k^2}\boldsymbol{\nabla}k^2, \tag{2.36}$$

where, in deriving (2.36) we have used the fact that the wavevector $\boldsymbol{k}$ is the phase gradient and therefore subject to the condition $(\boldsymbol{\nabla}\times\boldsymbol{k})\cdot\hat{\boldsymbol{z}} = (\partial k_2/\partial X) - (\partial k_1/\partial Y) = 0$.

Having rotated the horizontal velocities to a frame of reference coincident with the local cross-roll and along-the-roll coordinates of the rolls, we next must decide how we are going to decompose the fluctuating fields $\tilde{u}_1 = \hat{\boldsymbol{k}} \cdot \boldsymbol{u}_1$, $\tilde{v}_1 = (\hat{\boldsymbol{k}} \times \boldsymbol{u}_1) \cdot \hat{\boldsymbol{z}}$, w_1, T_1, p_1. For the steady roll solution we had introduced the bases $\{g_n'(z)\,\mathrm{e}^{\mathrm{i}m\theta}$, $g_n(z)\,\mathrm{e}^{\mathrm{i}m\theta}$, $\sin n\pi(z+\frac{1}{2})\,\mathrm{e}^{\mathrm{i}m\theta}$ and $\cos n\pi(z+\frac{1}{2})\,\mathrm{e}^{\mathrm{i}m\theta}\}$ for these fields respectively. However, the steady roll solution has no net flux in either of the horizontal velocities whereas we now know that, because of the pattern curvature, a mean drift flow will be produced. Therefore, in principle, we should solve the equations for the fluctuating fields on a set of basis elements which includes the extra modes $f_0(z)$ and $g_0(z)$, such that the mean fluxes

$$\int_{-\frac{1}{2}}^{\frac{1}{2}} f_0(z)\,\mathrm{d}z, \quad \int_{-\frac{1}{2}}^{\frac{1}{2}} g_0(z)\,\mathrm{d}z$$

are non-zero, in the two horizontal velocity components. This means that when the solvability condition (which leads to the phase diffusion equation) is applied, the term $\boldsymbol{\nabla} p_s$ involving the gradient of the slowly varying pressure component p_s will enter directly into the phase diffusion equation as the adjoint eigenfunctions will contain terms whose vertical average is non-zero. Whereas the presence of this term is absolutely correct, in this form it is difficult to see that it is precisely equivalent to an advection of the phase contours by the mean drift velocity. Therefore, we adopt a slightly different approach, which leads to a more natural form of the phase diffusion equation in which terms involving $\boldsymbol{\nabla} p_s$ are absent and are replaced by a term representing the advection of the phase contour by a mean drift horizontal velocity field. The consistency and complete equivalence of the two points of view is discussed in Appendix B.

Accordingly we write

$$\tilde{u}_1 = U_1 + \tilde{u}_1', \quad \tilde{v}_1 = V_1 + \tilde{v}_1', \tag{2.37}$$

where the components U_1, V_1 are θ-independent and have a non-zero mean flux with a vertical structure $f(z)$ satisfying the zero boundary conditions on $z \pm \frac{1}{2}$. The components $\tilde{u}_1'$ and $\tilde{v}_1'$ have zero fluxes. In practice we shall choose $f(z)$ to have the profile of a Poiseuille flow $z^2 - \frac{1}{4}$ because, as the Prandtl number gets larger, the vertical structure approaches this profile closely; namely the terms in $\tilde{u}_1'$, $\tilde{v}_1'$ contribute significantly to the stresses at the horizontal boundaries, i.e. to the left-hand side of (2.29), (2.30). Using (2.34) we can write

$$U_1 = \frac{f}{\langle f \rangle}(\hat{\boldsymbol{k}} \times \boldsymbol{\nabla}\psi) \cdot \hat{\boldsymbol{z}}, \quad V_1 = -\frac{f}{\langle f \rangle}\hat{\boldsymbol{k}} \cdot \boldsymbol{\nabla}\psi \tag{2.38}$$

where $\langle f \rangle = \int_{-\frac{1}{2}}^{\frac{1}{2}} f(z)\,\mathrm{d}z$.

The equations for $\tilde{u}_1$, $\tilde{v}_1$, w_1, T_1, p_1 decompose into two separate groups, one set for $\tilde{u}_1$, w_1, T_1, and p_1 and a separate equation for $\tilde{v}_1$. The equations for the former set are singular, having a non trivial roll solution $\partial\tilde{u}_0/\partial\theta$, $\partial w_0/\partial\theta$, $\partial T_0/\partial\theta$, $\partial p_0/\partial\theta$. They are not self-adjoint, however, and therefore we shall be required to compute the adjoint solution. On the other hand, the equation for $\tilde{v}_1'$ is non-singular. The equations are

$$\left(k^2\frac{\partial^2}{\partial\theta^2} + \frac{\partial^2}{\partial z^2}\right)\tilde{u}_1' - 2\sigma k\frac{\partial}{\partial\theta}\tilde{u}_0\tilde{u}_1' - \sigma\frac{\partial}{\partial z}(\tilde{u}_0 w_1 + \tilde{u}_1' w_0) - k\frac{\partial p_1}{\partial\theta}$$

$$= \sigma\Theta_T\frac{\partial}{\partial\theta}\tilde{u}_0 + \sigma U_1 k\frac{\partial\tilde{u}_0}{\partial\theta} + \sigma w_0\frac{\partial U_1}{\partial z} - \frac{\partial^2 U_1}{\partial z^2} - D\frac{\partial}{\partial\theta}\tilde{u}_0 + \sigma\boldsymbol{\nabla}\cdot\hat{\boldsymbol{k}}\,\tilde{u}_0^2 + (\hat{\boldsymbol{k}}\cdot\boldsymbol{\nabla})(p_0 + p_s), \tag{2.39}$$

$$\left(k^2\frac{\partial^2}{\partial\theta^2}+\frac{\partial^2}{\partial z^2}\right)w_1-\sigma k\frac{\partial}{\partial\theta}(\tilde{u}_0 w_1+\tilde{u}_1' w_0)-2\sigma\frac{\partial}{\partial z}w_0 w_1-\frac{\partial p_1}{\partial z}+T_1$$

$$=\sigma\Theta_T\frac{\partial w_0}{\partial\theta}+\sigma U_1 k\frac{\partial w_0}{\partial\theta}-D\frac{\partial w_0}{\partial\theta}+\sigma\nabla\cdot\hat{\boldsymbol{k}}\,\tilde{u}_0 w_0, \quad (2.40)$$

$$\left(k^2\frac{\partial^2}{\partial\theta^2}+\frac{\partial^2}{\partial z^2}\right)T_1-k\frac{\partial}{\partial\theta}(\tilde{u}_0 T_1+\tilde{u}_1 T_0)-\frac{\partial}{\partial z}(w_0 T_1+w_1 T_0)+Rw_1$$

$$=\Theta_T\frac{\partial T_0}{\partial\theta}+U_1 k\frac{\partial T_0}{\partial\theta}-D\frac{\partial T_0}{\partial\theta}+\nabla\cdot\hat{\boldsymbol{k}}\,\tilde{u}_0 T_0, \quad (2.41)$$

$$k\frac{\partial\tilde{u}_1'}{\partial\theta}+\frac{\partial w_1}{\partial z}=-\nabla\cdot\boldsymbol{u}_0=-\nabla\cdot\hat{\boldsymbol{k}}\,\tilde{u}_0, \quad (2.42a)$$

$$k\frac{\partial\tilde{u}_2}{\partial\theta}+\frac{\partial w_2}{\partial z}=-\frac{\partial u_1}{\partial X}-\frac{\partial v_1}{\partial Y}, \quad (2.42b)$$

$$\left(k^2\frac{\partial^2}{\partial\theta^2}+\frac{\partial^2}{\partial z^2}\right)\tilde{v}_1-\sigma k\frac{\partial}{\partial\theta}\tilde{u}_0\tilde{v}_1-\sigma\frac{\partial}{\partial z}(w_0\tilde{v}_1')$$

$$=-\frac{\partial^2 V_1}{\partial z^2}+\sigma w_0\frac{\partial V_1}{\partial z}-2\tilde{u}_0(\hat{\boldsymbol{k}}\times(\hat{\boldsymbol{k}}\cdot\nabla)\cdot\hat{\boldsymbol{k}})+\sigma\tilde{u}_0^2(\hat{\boldsymbol{k}}\times(\hat{\boldsymbol{k}}\cdot\nabla)\cdot\hat{\boldsymbol{k}})+(\hat{\boldsymbol{k}}\times\nabla(p_0+p_s))\cdot\hat{\boldsymbol{z}}. \quad (2.43)$$

The equations for the adjoint fields $(\tilde{u}^A, \tilde{v}^A, w^A, T^A, p^A)$ with the boundary conditions that the first four variables vanish at the horizontal boundaries and that all are periodic in θ are

$$\left(k^2\frac{\partial^2}{\partial\theta^2}+\frac{\partial^2}{\partial z^2}\right)\tilde{u}^A+2\sigma k\tilde{u}_0\frac{\partial}{\partial\theta}\tilde{u}^A+\sigma w_0\frac{\partial}{\partial z}\tilde{u}^A+\sigma k w_0\frac{\partial}{\partial\theta}w^A+kT_0\frac{\partial}{\partial\theta}T^A-k\frac{\partial}{\partial\theta}p^A=0, \quad (2.44)$$

$$\left(k^2\frac{\partial^2}{\partial\theta^2}+\frac{\partial^2}{\partial z^2}\right)\tilde{w}^A+\sigma\tilde{u}_0\frac{\partial}{\partial z}\tilde{u}^A+\sigma k\tilde{u}_0\frac{\partial}{\partial z}w^A+2\sigma w_0\frac{\partial}{\partial\theta}w^A+T_0\frac{\partial}{\partial\theta}T^A+RT^A-\frac{\partial}{\partial\theta}p^A=0, \quad (2.45)$$

$$\left(k^2\frac{\partial^2}{\partial\theta^2}+\frac{\partial^2}{\partial z^2}\right)T^A+w^A+k\tilde{u}_0\frac{\partial}{\partial\theta}T^A+w_0\frac{\partial}{\partial z}T^A=0, \quad (2.46)$$

$$k\frac{\partial}{\partial\theta}\tilde{u}^A+\frac{\partial}{\partial z}w^A=0, \quad (2.47)$$

$$\left(k^2\frac{\partial^2}{\partial\theta^2}+\frac{\partial^2}{\partial z^2}\right)\tilde{v}^A+\sigma k\tilde{u}_0\frac{\partial}{\partial\theta}\tilde{v}^A+\sigma w_0\frac{\partial}{\partial z}\tilde{v}^A=0. \quad (2.48)$$

For these equations, there are two non-trivial solutions. The first, $(\tilde{u}^A, w^A, T^A, p^A, \tilde{v}^A=0)$ must be computed as function of k numerically and corresponds to the homogeneous solution $(\partial/\partial\theta)(\tilde{u}_0, w_0, T_0, p_0, \tilde{v}_0=0)$ of the homogeneous equations (2.39)–(2.43). The second, $(\tilde{u}^A=w^A=T^A=\tilde{v}^A=0,\ p^A=1)$ corresponds to the simpler solution $(\partial/\partial p_s)(\tilde{u}_0, w_0, T_0, p_0+p_s)$. To each of these solutions of the adjoint

problem, there corresponds a non-trivial constraint, a solvability condition found by applying the Fredholm alternative theorem, on the right-hand sides of (2.39)–(2.43). As we have mentioned, the second solvability condition is satisfied trivially at order ϵ and only gives a non-trivial result at order ϵ^2. Its application at second order in ϵ requires a knowledge of the θ-independent components of $\tilde{u}_1'$ and $\tilde{v}_1'$.

On the other hand, the application of the first solvability condition gives a non-trivial constraint, the phase diffusion equation, at order ϵ:

$$\begin{aligned}
&\Theta_T\left\{\sigma\left(\tilde{u}^{\mathrm{A}},\frac{\partial\tilde{u}_0}{\partial\theta}\right)+\sigma\left(w^{\mathrm{A}},\frac{\partial w_0}{\partial\theta}\right)+\left(T^{\mathrm{A}},\frac{\partial T_0}{\partial\theta}\right)\right\}+(\boldsymbol{k}\times\boldsymbol{\nabla}\psi)\cdot\hat{\boldsymbol{z}}\left\{\sigma\left(\frac{f}{\langle f\rangle}\frac{\partial\tilde{u}_0}{\partial\theta},\tilde{u}^{\mathrm{A}}\right)\right.\\
&\quad+\sigma\left(\frac{f}{\langle f\rangle}\frac{\partial w_0}{\partial\theta},w^{\mathrm{A}}\right)+\left(\frac{f}{\langle f\rangle}\frac{\partial T_0}{\partial\theta},T^{\mathrm{A}}\right)\\
&\quad\left.+\frac{\sigma}{k}\left(w_0\frac{1}{\langle f\rangle}\frac{\mathrm{d}f}{\mathrm{d}z},\tilde{u}^{\mathrm{A}}\right)-\frac{1}{k}\left(\frac{1}{\langle f\rangle}\frac{\mathrm{d}^2f}{\mathrm{d}z^2},\tilde{u}^{\mathrm{A}}\right)\right\}\\
&\quad-\left(D\frac{\partial\tilde{u}_0}{\partial\theta},\tilde{u}^{\mathrm{A}}\right)+\sigma(\boldsymbol{\nabla}\cdot\hat{\boldsymbol{k}}\tilde{u}_0^2,\tilde{u}^{\mathrm{A}})+(\hat{\boldsymbol{k}}\cdot\boldsymbol{\nabla}p_0,\tilde{u}^{\mathrm{A}})\\
&\quad-\left(D\frac{\partial w_0}{\partial\theta},w^{\mathrm{A}}\right)+\sigma(\boldsymbol{\nabla}\cdot\hat{\boldsymbol{k}}\tilde{u}_0w_0,w^{\mathrm{A}})-\left(D\frac{\partial T_0}{\partial\theta},T^{\mathrm{A}}\right)\\
&\quad+(\boldsymbol{\nabla}\cdot\hat{\boldsymbol{k}}\tilde{u}_0T_0,T^{\mathrm{A}})-(p^{\mathrm{A}},\boldsymbol{\nabla}\cdot\hat{\boldsymbol{k}}\tilde{u}_0)=0. \qquad (2.49)
\end{aligned}$$

The notation $(\tilde{u}^{\mathrm{A}},\partial\tilde{u}_0/\partial\theta)$ means

$$\int_{-\frac{1}{2}}^{\frac{1}{2}}\mathrm{d}z\int_0^{2\pi}\mathrm{d}\theta\,\tilde{u}^{\mathrm{A}}(\theta,z)\frac{\partial\tilde{u}_0}{\partial\theta}(\theta,z).$$

In practice, these inner products and indeed the concrete representations of the adjoint solutions are all calculated in the Galerkin basis used to convert the partial differential equations (2.39)–(2.43) to algebraic equations. However, it is useful for the moment to treat the equation formally in order to see its structure. The factors of Θ_T and $(\boldsymbol{k}\times\boldsymbol{\nabla}\psi)\cdot\hat{\boldsymbol{z}}$, depend only on k, the modulus of the wavevector. They are determined numerically. Writing $\boldsymbol{V}=\boldsymbol{\nabla}\times\psi\hat{\boldsymbol{z}}$, the first two terms can be written as

$$\Theta_T+\rho(k)\,\boldsymbol{k}\cdot\boldsymbol{V}, \qquad (2.50)$$

a combination which indicates that the contours of constant phase are advected by an effective (a vertically averaged with non-trivial weighting) mean drift field $\rho(k)\,\boldsymbol{V}$. Observe that while $\boldsymbol{V}$, the horizontal velocity induced by the short-scale Reynolds stresses, is divergence free, the effective mean drift field $\rho(k)\,\boldsymbol{V}$, which advects the phase contours, has a non-zero divergence. The remaining terms divided by the factor multiplying Θ_T, can be written in the form

$$\gamma_{11}\Theta_{XX}+2\gamma_{12}\Theta_{XY}+\gamma_{22}\Theta_{YY}, \qquad (2.51)$$

where

$$\gamma_{11}=\gamma(k)+\beta(k)\,\Theta_X^2,\quad \gamma_{12}=\beta(k)\,\Theta_X\Theta_Y,\quad \gamma_{22}=\gamma(k)+\beta(k)\,\Theta_Y^2 \qquad (2.52)$$

and, after multiplication by a suitable integration factor, this term takes the rotationally invariant form

$$\frac{1}{\tau(k)}\boldsymbol{\nabla}\cdot\boldsymbol{k}B(k). \qquad (2.53)$$

The phase diffusion equation is, therefore,

$$\Theta_T + \rho(k)\,\boldsymbol{k}\cdot\boldsymbol{V} + \frac{1}{\tau(k)}\nabla\cdot\boldsymbol{k}B(k) = 0, \tag{2.54}$$

and has exactly the form derived by Cross & Newell (1984) for several model equations of Oberbeck–Boussinesq type.

It remains to derive the equation for

$$\boldsymbol{V} = \nabla\times\psi\hat{\boldsymbol{z}}. \tag{2.55}$$

The steps in this calculation are

(i) Solve the singular equations (2.39)–(2.42), partial differential equations in the independent variables θ and z, for $\tilde{u}_1', w_1, T_1, p_1$ and in particular the θ-independent component of $\tilde{u}_1'$ (which we call $\hat{u}_1$) in terms of $(\hat{\boldsymbol{k}}\times\nabla\psi)\cdot\hat{\boldsymbol{z}}$ and the partial derivatives Θ_T, Θ_{XX}, Θ_{XY}, Θ_{YY}. We find

$$\hat{u}_1 = \hat{u}_0\Theta_T + \hat{u}_{11}\Theta_{XX} + 2\hat{u}_{12}\Theta_{XY} + \hat{u}_{22}\Theta_{YY} + \hat{u}(\boldsymbol{k}\times\nabla\psi)\cdot\hat{\boldsymbol{z}}. \tag{2.56}$$

The coefficients $\hat{u}_0$, $\hat{u}_{ij}$, $\hat{u}$ are functions of z.

(ii) Solve the non-singular equation (2.43) for $\tilde{v}_1'$ and in particular its θ-independent component which we call $\hat{v}_1$,

$$\hat{v}_1 = \hat{v}_{11}\Theta_{XX} + 2\hat{v}_{12}\Theta_{XY} + \hat{v}_{22}\Theta_{YY} - \hat{v}(\hat{\boldsymbol{k}}\cdot\nabla\psi). \tag{2.57}$$

The total θ-independent velocity components $U_1+\hat{u}_1$, $V_1+\hat{v}_1$ in the across-the-roll and along-the-roll directions are therefore exactly (2.56) and (2.57) with $\hat{u}$ replaced by $f/\langle f\rangle+\hat{u}$ and $\hat{v}$ replaced by $f/\langle f\rangle+\hat{v}$. It is important to make the point that the functions $f/\langle f\rangle+u$ and $f/\langle f\rangle+\hat{v}$ are independent of the choice of $f(z)$. This was verified numerically by comparing these functions for several choices of $f(z)$, among them $f(z)=z^2-\frac{1}{4}$, the most convenient, and $f(z)=\sin\pi(z+\frac{1}{2})$.

Remark By inspection of the right-hand sides of (2.56) and (2.57) the terms $\hat{u}_{11}\Theta_{XX}+2\hat{u}_{12}\Theta_{XY}+\hat{u}_{22}\Theta_{YY}$ can be seen to have the form of an integrating factor times $\nabla\cdot\boldsymbol{k}F(k)$. The terms $\hat{v}_{11}\Theta_{XX}+2\hat{v}_{12}\Theta_{XY}+\hat{v}_{22}\Theta_{YY}$ have the form of the z-component of a curl, namely $(\nabla\times\boldsymbol{k}F(k))\cdot\hat{\boldsymbol{z}}$.

(iii) Define

$$\left.\begin{aligned}
&\left\langle\frac{\mathrm{d}^2\hat{u}_0}{\mathrm{d}z^2}\right\rangle = \alpha_0, \quad \left\langle\frac{\mathrm{d}^2\hat{u}_{ij}}{\mathrm{d}z^2}\right\rangle = \alpha_{ij}, \quad \left\langle\frac{\mathrm{d}^2\hat{u}}{\mathrm{d}z^2}+\frac{1}{\langle f\rangle}\frac{\mathrm{d}^2 f}{\mathrm{d}z^2}\right\rangle = \alpha',\\
&\left\langle\frac{\mathrm{d}^2\hat{v}_{ij}}{\mathrm{d}z^2}\right\rangle = \beta_{ij}, \quad \left\langle\frac{\mathrm{d}^2\hat{v}}{\mathrm{d}z^2}+\frac{1}{\langle f\rangle}\frac{\mathrm{d}^2 f}{\mathrm{d}z^2}\right\rangle = \beta
\end{aligned}\right\} \tag{2.58}$$

and substitute

$$\left\langle\frac{\mathrm{d}^2}{\mathrm{d}z^2}\begin{pmatrix}\bar{u}_1\\ \bar{v}_1\end{pmatrix}\right\rangle = \begin{pmatrix}\hat{k}_1\\ \hat{k}_2\end{pmatrix}\left\langle\frac{\mathrm{d}^2}{\mathrm{d}z^2}(U_1+\hat{u}_1)\right\rangle + \begin{pmatrix}-\hat{k}_2\\ \hat{k}_1\end{pmatrix}\left\langle\frac{\mathrm{d}^2}{\mathrm{d}z^2}(V_1+\hat{v}_1)\right\rangle$$

into (2.29), (2.30). We obtain

$$\begin{aligned}
\nabla p_{\mathrm{s}} = {}& -\sigma\boldsymbol{k}\nabla\cdot\boldsymbol{k}\frac{\langle\tilde{u}_0^2\rangle}{k} - \tfrac{1}{2}\sigma\frac{\langle\tilde{u}_0^2\rangle}{k^2}\nabla k^2\\
&+\begin{pmatrix}\hat{k}_1\\ \hat{k}_2\end{pmatrix}\{\alpha'(\hat{\boldsymbol{k}}\times\nabla\psi)\cdot\hat{\boldsymbol{z}} + \alpha_0\Theta_T + \alpha_{11}\Theta_{XX} + 2\alpha_{12}\Theta_{XY} + \alpha_{22}\Theta_{YY}\}\\
&+\begin{pmatrix}-\hat{k}_2\\ \hat{k}_1\end{pmatrix}\{-\beta(\hat{\boldsymbol{k}}\cdot\nabla\psi) + \beta_{11}\Theta_{XX} + 2\beta_{12}\Theta_{XY} + \beta_{22}\Theta_{YY}\}.
\end{aligned} \tag{2.59}$$

We can write

$$\alpha_{11}\Theta_{XX}+2\alpha_{12}\Theta_{XY}+\alpha_{22}\Theta_{YY}=\frac{1}{\tau'_\alpha(k)}\nabla\cdot\boldsymbol{k}B'_\alpha(k), \tag{2.60}$$

$$\beta_{11}\Theta_{XX}+2\beta_{12}\Theta_{XY}+\beta_{22}\Theta_{YY}=(\nabla\times\boldsymbol{k}B_\beta(k))\cdot\hat{z}. \tag{2.61}$$

The mean drift equation is obtained by eliminating p_s,

$$\hat{z}\cdot\nabla\times\hat{\boldsymbol{k}}\left\{(\alpha'-\alpha_0\rho k)(\hat{\boldsymbol{k}}\times\nabla\psi)\cdot\hat{z}+\alpha_0\left(\frac{1}{\tau'_\alpha(k)}\nabla\cdot\boldsymbol{k}B'_\alpha(k)-\frac{1}{\tau(k)}\nabla\cdot\boldsymbol{k}B(k)\right)\right\}$$

$$+\nabla\cdot\{\hat{\boldsymbol{k}}(-\beta\hat{\boldsymbol{k}}\cdot\nabla\psi+(\nabla\times\boldsymbol{k}B_\beta(k))\cdot\hat{z})\}=\sigma\hat{z}\cdot\nabla\times\boldsymbol{k}\nabla\cdot\boldsymbol{k}A^2,\quad A^2=\frac{\langle\tilde{u}_0^2\rangle}{k^2}, \tag{2.62}$$

where the phase diffusion equation (2.54) is used to replace Θ_T and we have noted the fact that the second term on the right-hand side of (2.36) is a gradient. Since B'_α always occurs together with B we define a new B_α, τ_α defined by

$$\alpha_0\left(\frac{1}{\tau'_\alpha}\nabla\cdot\boldsymbol{k}B'_\alpha-\frac{1}{\tau}\nabla\cdot\boldsymbol{k}B\right)=\alpha_0((\alpha_{11}-\gamma_{11})\Theta_{XX}+2(\alpha_{12}-\gamma_{12})\Theta_{XY}+(\alpha_{22}-\gamma_{22})\Theta_{YY})$$

$$=\frac{1}{\tau_\alpha}\nabla\cdot\boldsymbol{k}B_\alpha. \tag{2.63}$$

We also set

$$\alpha'-\alpha_0\rho k=\alpha \tag{2.64}$$

and then write (2.62) as

$$\hat{z}\cdot\nabla\times\hat{\boldsymbol{k}}\alpha(\hat{\boldsymbol{k}}\times\nabla\psi)\cdot\hat{z}-\nabla\cdot\hat{\boldsymbol{k}}\beta\hat{\boldsymbol{k}}\cdot\nabla\psi=\hat{z}\cdot\nabla\times\left(\sigma k\nabla\cdot\boldsymbol{k}A^2-\frac{\hat{\boldsymbol{k}}}{\tau_\alpha}\nabla\cdot\boldsymbol{k}B_\alpha\right)$$

$$-\nabla\cdot\hat{\boldsymbol{k}}(\nabla\times\boldsymbol{k}B_\beta)\cdot\hat{z}. \tag{2.65}$$

Note that the term containing A^2 could be absorbed in B_α. It is not done here since we want to separate the contributions coming from the horizontal and vertical Reynolds stress and because it will be useful to keep an explicit dependence on the amplitude A in Appendix E. The two equations, (2.54) the phase diffusion equation and (2.65) the mean drift equation, constitute a closed pair of equations for the slowly varying fields

$$\boldsymbol{k}(X,Y,T)=\nabla\Theta,\quad V(X,Y,T)=\nabla\times\psi\hat{z}. \tag{2.66}$$

We observe that the equation pair (2.54) and (2.65) has the properties of translational invariance, rotational invariance and (local) Galilean invariance. The first two properties can be seen by inspection. A small calculation will show that the equations are also invariant if the slowly varying velocity $\boldsymbol{U}(X,Y,T)$ is added to $f/\langle f\rangle\, V$ and the spatial coordinates are measured with respect to a frame of reference moving with velocity $\mathrm{d}\boldsymbol{X}/\mathrm{d}T=\boldsymbol{U}$. So even though the original microscopic system does not have the property of Galilean invariance because of the no-slip boundary conditions, the macroscopic equations describing the dynamics of the wavevector and mean-drift fields do.

In most cases, the most natural conditions to apply on the lateral boundaries are

$$\boldsymbol{k}\cdot\hat{\boldsymbol{n}}=V\cdot\hat{\boldsymbol{n}}=0, \tag{2.67}$$

namely the lateral boundary is normal to constant phase contours (the roll axes are

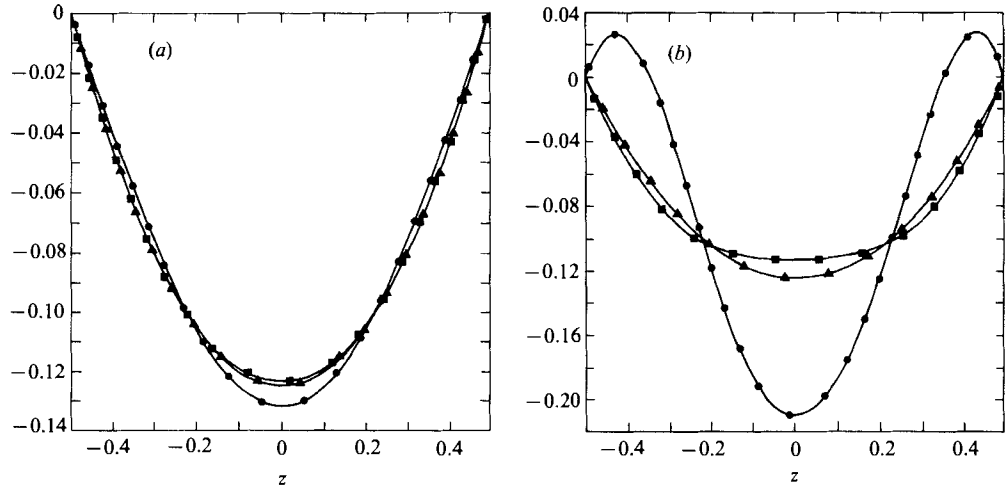

FIGURE 6. The vertical structure of the coefficients of $(\hat{\boldsymbol{k}} \times \nabla\psi) \cdot \hat{\boldsymbol{z}}$ (circles) and $-\hat{\boldsymbol{k}} \cdot \nabla\psi$ (squares) for (a) $P = 0.71$, $R = 1800$ and (b) $P = 0.71$, $R = 3000$; and the Poiseuille profile (triangles).

perpendicular to the boundary) and also a streamline. In certain situations, it may be necessary to take account of viscous boundary layers associated with the mean drift velocity. On the other hand, if the lateral boundaries are heated, they can force the roll axis to be tangent to the boundary, and in those cases the relevant boundary condition is that

$$\boldsymbol{k} \times \hat{\boldsymbol{n}} = 0 \tag{2.68}$$

or that the lateral boundary is a constant phase contour. We shall study this case when we examine the stability of boundary forced circular roll patches in cylindrical geometries.

As a final remark in this subsection, we want to emphasize the importance of solving for the complete θ-independent mean drift velocity fields $U_1 + \hat{u}_1$, $V_1 + \hat{v}_1$ and not simply relying on the first terms U_1, V_1 which are the ones associated with non zero flux. In figure 6, we show graphs of the z-dependence of the coefficients in $U_1 + \hat{u}_1$ and $V_1 + \hat{v}_1$ proportional to $(\hat{\boldsymbol{k}} \times \nabla\psi) \cdot \hat{\boldsymbol{z}}$ and $(-\hat{\boldsymbol{k}} \cdot \nabla\psi)$ respectively at Rayleigh numbers 1800 and 3000 for a value of Prandtl number $P = 0.71$. If the slow pressure gradient ∇p_s dominated the contribution to the mean drift fields we would find vertical profiles which were Poiseuille-like. In figure 6(a), in which we plot $\hat{u}$, $\hat{v}$ (the coefficients of $(\hat{\boldsymbol{k}} \times \nabla\psi) \cdot \hat{\boldsymbol{z}}$ and $-\hat{\boldsymbol{k}} \cdot \nabla\psi$ in $U_1 + \hat{u}_1$, $V_1 + \hat{v}_1$ respectively), we observe that the profiles match the Poiseuille-like profiles arising from U_1, V_1 alone very well. However at $R = 3000$, figure 6(b), there are significant differences, in particular in the profile of $\hat{\boldsymbol{u}}$ marked with circles. We find this behaviour, the departure of the vertical structure of the $(\hat{\boldsymbol{k}} \times \nabla\psi) \cdot \hat{\boldsymbol{z}}$ component of the θ-independent field, to be typical of the across-the-roll component of the mean drift velocity at all low and low to moderate Prandtl numbers up to about $P = 3$. Obviously this departure has a crucial effect on the coefficients in the mean drift equation because both α and β depend on the boundary stress which depends on the derivatives of $\hat{u}$ and $\hat{v}$ at $z = \pm\frac{1}{2}$.

In order to find the z-structure of the total, as opposed to that of the $(\hat{\boldsymbol{k}} \times \nabla\psi) \cdot \hat{\boldsymbol{z}}$ term, mean drift velocity field, we also have to take account of the other terms such as $\alpha_{ij}, \beta_{ij}, i = 1, 2$ which are the coefficients which depend on $\Theta_{XX}, \Theta_{XY}, \Theta_{YY}$, namely the particulars of the pattern structure. These terms are also important and non-trivial. In summary, then, we want to stress that for low to moderate Prandtl

numbers, any attempt to circumvent solving for the full $\tilde{u}_1$, $\tilde{v}_1$ fields by guessing the vertical structure of their θ-independent components is doomed to failure. Indeed, in our first attempts to derive the phase diffusion and mean drift equations, we had fallen into this trap.

2.4. *Implementation of the calculation*

The key step in this list is the calculation of u_1', w_1, T_1, p_1 from the singular equations (2.39)–(2.42*a*) and $\tilde{v}_1'$ from the non-singular equation (2.43). The first set of equations can be written in the vector form

$$L_1(\tilde{u}_1', w_1, T_1, p_1) = \boldsymbol{c}_0 \Theta_T + \boldsymbol{c}_{11}\Theta_{XX} + 2\boldsymbol{c}_{12}\Theta_{XY} + \boldsymbol{c}_{22}\Theta_{YY} + \boldsymbol{c}_1 \hat{\boldsymbol{k}} \cdot \nabla p_s + \boldsymbol{c}_2(\hat{\boldsymbol{k}} \times \nabla\psi) \cdot \hat{\boldsymbol{z}}, \tag{2.69}$$

where the vectors $\boldsymbol{c}_0$, $\boldsymbol{c}_{11}$, $\boldsymbol{c}_{12}$, $\boldsymbol{c}_{22}$, $\boldsymbol{c}_1$ and $\boldsymbol{c}_2$ are

$$\boldsymbol{c}_0 = \left(\sigma\frac{\partial}{\partial\theta}\tilde{u}_0, \sigma\frac{\partial}{\partial\theta}w_0, \frac{\partial}{\partial\theta}T_0, 0\right), \tag{2.70}$$

$$\boldsymbol{c}_1 = (1,0,0,0), \tag{2.71}$$

$$\boldsymbol{c}_{11} = \begin{cases} -\left(4k_1^2\frac{\partial}{\partial k^2}\left(\frac{\partial}{\partial\theta}\tilde{u}_0\right) + \frac{\partial}{\partial\theta}\tilde{u}_0\right) + \sigma\left(2\frac{k_1^2}{k}\frac{\partial}{\partial k^2}\tilde{u}_0^2 + \frac{\tilde{u}_0^2}{k^3}k_2^2\right) + \left(2\frac{k_1^2}{k}\frac{\partial p_0}{\partial k^2}\right) \\ -\left(4k_1^2\frac{\partial}{\partial k^2}\left(\frac{\partial}{\partial\theta}w_0\right) + \frac{\partial}{\partial\theta}w_0\right) + \sigma\left(2\frac{k_1^2}{k}\frac{\partial}{\partial k^2}(\tilde{u}_0 w_0) + \frac{u_0 w_0}{k^3}k_2^2\right) \\ -\left(4k_1^2\frac{\partial}{\partial k^2}\left(\frac{\partial}{\partial\theta}T_0\right) + \frac{\partial}{\partial\theta}T_0\right) + \left(2\frac{k_1^2}{k}\frac{\partial}{\partial k^2}(T_0 w_0) + \frac{T_0 u_0}{k^3}k_2^2\right) \\ 2\frac{k_2^2}{k}\frac{\partial}{\partial k^2}\tilde{u}_0 + \frac{\tilde{u}_0}{k^3}k_2^2, \end{cases} \tag{2.72}$$

$$\boldsymbol{c}_{12} = \begin{cases} -\left(4k_1k_2\frac{\partial}{\partial k^2}\left(\frac{\partial}{\partial\theta}\tilde{u}_0\right)\right) + \sigma\left(2\frac{k_1k_2}{k}\frac{\partial}{\partial k^2}\tilde{u}_0^2 + \frac{\tilde{u}_0^2}{k^3}k_1k_2\right) + \left(2\frac{k_1k_2}{k}\frac{\partial p_0}{\partial k^2}\right) \\ -\left(4k_1k_2\frac{\partial}{\partial k^2}\left(\frac{\partial}{\partial\theta}w_0\right)\right) + \sigma\left(2\frac{k_1k_2}{k}\frac{\partial}{\partial k^2}(w_0\tilde{u}_0) + \frac{(w_0\tilde{u}_0)}{k^3}k_2^2\right) \\ -\left(4k_1k_2\frac{\partial}{\partial k^2}\left(\frac{\partial}{\partial\theta}T_0\right)\right) + \left(2\frac{k_1k_2}{k}(T_0\tilde{u}_0) + \frac{T_0\tilde{u}_0}{k^3}k_2^2\right) \\ 2\frac{k_2^2}{k}\frac{\partial}{\partial k^2}\tilde{u}_0 + \frac{k_1k_2}{k^3}\tilde{u}_0, \end{cases} \tag{2.73}$$

$$\boldsymbol{c}_{22} = \begin{cases} -\left(4k_2^2\frac{\partial}{\partial k^2}\left(\frac{\partial}{\partial\theta}\tilde{u}_0\right) + \frac{\partial}{\partial\theta}\tilde{u}_0\right) + \sigma\left(2\frac{k_2^2}{k}\frac{\partial}{\partial k^2}\tilde{u}_0^2 + \frac{\tilde{u}_0^2}{k^3}\cdot k_1^2\right) + \left(2\frac{k_2^2}{k}\frac{\partial p_0}{\partial k^2}\right) \\ -\left(4k_2^2\frac{\partial}{\partial k^2}\left(\frac{\partial}{\partial\theta}w_0\right) + \frac{\partial}{\partial\theta}w_0\right) + \sigma\left(2\frac{k_2^2}{k}\frac{\partial}{\partial k^2}(w_0\tilde{u}_0) + \frac{(w_0\tilde{u}_0)}{k^3}k_2^2\right) \\ -\left(4k_2^2\frac{\partial}{\partial k^2}\left(\frac{\partial}{\partial\theta}T_0 + \frac{\partial}{\partial\theta}T_0\right)\right) + \left(2\frac{k_1^2}{k}\frac{\partial}{\partial k^2}(T_0\tilde{u}_0) + \frac{T_0\tilde{u}_0}{k^3}k_2^2\right) \\ 2\frac{k_2^2}{k}\frac{\partial}{\partial k^2}\tilde{u}_0 + \frac{\tilde{u}_0}{k^3}k_1^2, \end{cases} \tag{2.74}$$

$$c_2 = \frac{1}{\langle f \rangle}\left(\sigma k f \frac{\partial \tilde{u}_0}{\partial \theta} + \sigma w_0 f' - f'', \sigma k f \frac{\partial w_0}{\partial \theta}, k f \frac{\partial T_0}{\partial \theta}, 0.\right) \tag{2.75}$$

The equation for $\tilde{v}_1'$ is

$$L_2(\tilde{v}_1') = e_{11}\Theta_{XX} + 2e_{12}\Theta_{XY} + e_{22}\Theta_{YY} + e_1(\hat{\boldsymbol{k}} \times \nabla p_s) \cdot \hat{\boldsymbol{z}} - e_2 \hat{\boldsymbol{k}} \cdot \nabla \psi, \tag{2.76}$$

where

$$e_{11} = -\frac{k_1 k_2}{k^3}\left(2k^2 \frac{\partial p_0}{\partial k^2} + \sigma \tilde{u}_0^2 - 2\tilde{u}_0\right), \tag{2.77}$$

$$e_{12} = \frac{k_1^2 - k_2^2}{k^3}\left(2k^2 \frac{\partial p_0}{\partial k^2} + \sigma \tilde{u}_0^2 - 2\tilde{u}_0\right), \tag{2.78}$$

$$e_{22} = \frac{k_1 k_2}{k^3}\left(2k^2 \frac{\partial p_0}{\partial k^2} + \sigma \tilde{u}_0^2 - 2\tilde{u}_0\right), \tag{2.79}$$

$$e_1 = 1, \tag{2.80}$$

$$e_2 = \frac{1}{\langle f \rangle}(\sigma w_0 f' - f''). \tag{2.81}$$

We observe that all the θ- and z-structure is contained in the coefficients c_0, $c_{1,}$ c_2, e_1, $e_{2,}$ c_{11}, c_{12}, c_{22}, e_{11}, e_{12}, e_{22}. The variables $\Theta_{XX}, \Theta_{XY}, \Theta_{YY}, \hat{\boldsymbol{k}} \cdot \nabla p_s, (\hat{\boldsymbol{k}} \times \nabla p_s) \cdot \hat{\boldsymbol{z}}, \hat{\boldsymbol{k}} \cdot \nabla \psi$, $(\hat{\boldsymbol{k}} \times \nabla \psi) \cdot \boldsymbol{z}$ are all constants as far as integration in θ, z is concerned. Therefore the particular solutions will also be linear combinations of the latter variables and will have the form (2.56), (2.57). In particular, since the terms $c_{11}\Theta_{XX} + 2c_{12}\Theta_{XY} + c_{22}\Theta_{YY}$ have the form of a scalar function of k times $\nabla \cdot \boldsymbol{k}F(k)$ for some scalar $F(k)$, then so will the solution. Also, the particular solution arising from $e_{11}\Theta_{XX} + 2e_{12}\Theta_{XY} + e_{22}\Theta_{YY}$ will have the form $\nabla \times \boldsymbol{k}G(k) \cdot \hat{\boldsymbol{z}}$ for some scalar $G(k)$.

How are these equations solved? First they are converted to algebraic equations for the coefficients of $\tilde{u}_1'$, w_1, T_1, p_1 expanded in the bases $\{e^{im\theta}(g_n'(z), g_n(z), \sin n\pi(z+\frac{1}{2}), \cos n\pi(z+\frac{1}{2}))\}$ respectively, and $\tilde{v}_1'$ expanded in the basis $\{e^{im\theta}g_n'(z)\}$, by projecting (2.39), (2.40), (2.41) and (2.43) into the bases $\{e^{im\theta}(g_n'(z), g_n(z), \sin n\pi(z+\frac{1}{2}), g_n'(z))\}$ respectively. The algebraic equations arising from (2.42a) are obtained by direct identification of coefficients of $e^{im\theta}g_n'(z)$. In this way we obtain two systems of algebraic equations:

$$\boldsymbol{A}_1 \boldsymbol{x} = \boldsymbol{c} \tag{2.82}$$

from (2.39)–(2.42a) and, from (2.43),

$$\boldsymbol{A}_2 \boldsymbol{y} = \boldsymbol{e}. \tag{2.83}$$

Because we have chosen that component of the horizontal velocities $\tilde{u}_1'$, $\tilde{v}_1'$ with non-zero flux to be contained entirely in U_1, V_1, the solutions $\tilde{u}_1'$, $\tilde{v}_1'$ are expanded in bases with zero flux, i.e. $\int \tilde{u}_1' \, d\theta \, dz = \int \tilde{v}_1' \, d\theta \, dz = 0$. Then, because $c_1 \hat{\boldsymbol{k}} \cdot \nabla p_s$ and $e_1 \hat{\boldsymbol{k}} \times \nabla p_s \cdot \hat{\boldsymbol{z}}$ have no projections in these bases, no terms proportional to ∇p_s will appear in either $\tilde{u}_1'$ or $\tilde{v}_1'$. On the other hand, if we had decomposed $\tilde{u}_1$, $\tilde{v}_1$ in the wider basis, then terms involving ∇p_s would have appeared on the right-hand side of (2.76) and (2.77) and have taken the place, in the phase diffusion equation, of the term $\rho(k)\boldsymbol{k} \cdot \boldsymbol{V}$. The equivalence of the two approaches is discussed in Appendix B.

There is a fundamental and important difference between the two systems (2.82) and (2.83). The first system is singular; $\boldsymbol{A}_1$ has a null space of dimension two. The second system is non-singular and can easily be inverted for all e. The vector $\boldsymbol{c}$ on the

right-hand side of (2.82), however, is constrained to lie in the range of $\boldsymbol{A}_1$ and a necessary and sufficient condition that it does is the Fredholm alternative theorem which demands that

$$\boldsymbol{v}^{\mathrm{T}}\boldsymbol{c} = 0 \tag{2.84}$$

for each $\boldsymbol{v}^{\mathrm{T}}(\boldsymbol{v})$ which is a left (right) null row (column) vector of $\boldsymbol{A}_1(\boldsymbol{A}_1^{\mathrm{T}})$. For the null vector corresponding to the homogeneous solution $(\partial/\partial\theta)(\tilde{u}_0, w_0, T_0, p_0)$ of (2.39)–(2.42a), (2.84) is precisely the phase diffusion equation and indeed the inner products appearing in (2.49) are evaluated directly from (2.84) for each k lying within the marginal stability curve. The solvability condition arising from null vector (0, 0, 0, 1) corresponding to the homogeneous solution $(\partial/\partial p_s)(\tilde{u}_0, w_0, T_0, p_0+p_s)$ is automatically satisfied at order ϵ.

To solve (2.82) we must subtract the projection of $\boldsymbol{c}$ which lies in the null space of $\boldsymbol{A}_1^{\mathrm{T}}$ from $\boldsymbol{c}$, namely we must replace $\boldsymbol{c}$ by $\boldsymbol{c}-(\boldsymbol{v}^{\mathrm{T}}\boldsymbol{c})\,\boldsymbol{v}$ where $\boldsymbol{v}^{\mathrm{T}}$ is the non-trivial unit left null vector of $\boldsymbol{A}_1^{\mathrm{T}}$ which gives rise to the phase diffusion equation. If we think of solving (2.82) separately for each of the coefficients of Θ_T, Θ_{XX}, Θ_{XY}, Θ_{YY} and $(\hat{\boldsymbol{k}}\times\nabla\psi)\cdot\hat{\boldsymbol{z}}$, then we must subtract from each corresponding $\boldsymbol{c}$ that portion which was used in the phase diffusion equation. The difficulty in achieving this task is that small numerical errors can mean that the $\boldsymbol{c}$ is not quite in the range of $\boldsymbol{A}_1$ and therefore we need a robust method of inversion which is relatively insensitive to these errors.

The generalized inverse obtained through applying a singular-valued decomposition (Businger & Golub 1969) to the singular matrix $\boldsymbol{A}_1$ is ideally suited for these purposes because it picks that solution x' of (2.82) which minimizes the least squares error $\|\boldsymbol{A}\boldsymbol{x}-\boldsymbol{x}\|^2$. Therefore it effectively solves

$$\boldsymbol{A}_1\boldsymbol{x}' = \boldsymbol{c}-(\boldsymbol{c},\boldsymbol{v})\,\boldsymbol{v}, \quad (\boldsymbol{c},\boldsymbol{v}) = \boldsymbol{v}^{\mathrm{T}}\boldsymbol{c}, \tag{2.85}$$

exactly. To see this we shall briefly describe the algorithm for square matrices and then illustrate its application with an example. Any matrix $\boldsymbol{A}$ can be decomposed into a product $\boldsymbol{U}\boldsymbol{D}\boldsymbol{V}^{\mathrm{T}}$, where $\boldsymbol{U}$ and $\boldsymbol{V}$ are orthogonal matrices and $\boldsymbol{D}$ a diagonal matrix. The diagonal entries of $\boldsymbol{D}$ are called the spectrum or singular values of $\boldsymbol{A}$. If $\boldsymbol{A}$ is singular, the number of zero entries is equal to $n-r$, where r is the rank of $\boldsymbol{A}$. The unit vectors consisting of the columns of $\boldsymbol{U}$ corresponding to the positions of the non-zero entries span the range of $\boldsymbol{A}$, the columns of $\boldsymbol{U}$ corresponding to zero entries span the null space of $\boldsymbol{A}^{\mathrm{T}}$. The columns of $\boldsymbol{V}$ corresponding to the position of zero entries of $\boldsymbol{D}$ span the null space of $\boldsymbol{A}$. The proof of these statements is an easy exercise. Because $\boldsymbol{U}$ is orthogonal, it is clear from this construction that the direct sum of the range of $\boldsymbol{A}$ and null space of $\boldsymbol{A}^{\mathrm{T}}$ spans R^n. Minimizing the least squares error $\|\boldsymbol{A}\boldsymbol{x}-\boldsymbol{c}\|^2$ means that $\boldsymbol{c}$ is resolved into $\boldsymbol{c}_1+\boldsymbol{c}_2$, where $\boldsymbol{c}_1$ belongs to the range of $\boldsymbol{A}$ and $\boldsymbol{c}_2$ to the null space of $\boldsymbol{A}^{\mathrm{T}}$ and that the choice of $\boldsymbol{x}'$ which achieves this goal solves $\boldsymbol{A}\boldsymbol{x}' = \boldsymbol{c}_1$ or (2.80). For example, if

$$\boldsymbol{A} = \begin{pmatrix} 1 & 1 \\ 2 & 2 \end{pmatrix} \quad \text{and} \quad \boldsymbol{c} = \begin{pmatrix} c^{(1)} \\ c^{(2)} \end{pmatrix}, \tag{2.86}$$

then the singular-valued decomposition of $\boldsymbol{A}$ is

$$\begin{pmatrix} \frac{1}{\sqrt{5}} & -\frac{2}{\sqrt{5}} \\ \frac{2}{\sqrt{5}} & \frac{1}{\sqrt{5}} \end{pmatrix} \begin{pmatrix} \sqrt{10} & 0 \\ 0 & 0 \end{pmatrix} \begin{pmatrix} \frac{1}{\sqrt{2}} & \frac{1}{\sqrt{2}} \\ -\frac{1}{\sqrt{2}} & \frac{1}{\sqrt{2}} \end{pmatrix}.$$

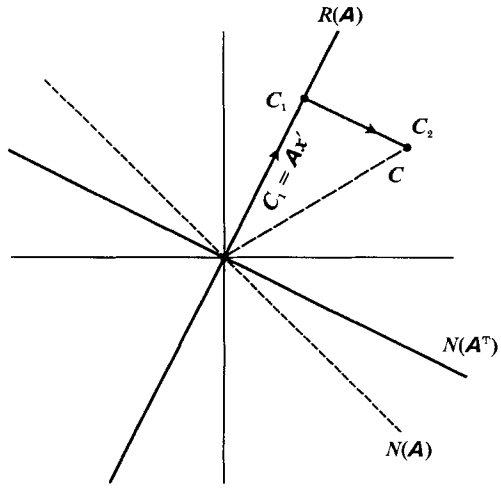

FIGURE 7. The range $R(\boldsymbol{A})$ and null space $N(\boldsymbol{A})$ of the matrix $\boldsymbol{A}$, the null space of $\boldsymbol{A}^{\mathrm{T}}(N(\boldsymbol{A}^{\mathrm{T}}))$, and the solution $\boldsymbol{x}'$ of $\boldsymbol{A}\boldsymbol{x} = \boldsymbol{c}$ given by minimizing $|\boldsymbol{A}\boldsymbol{x} - \boldsymbol{c}|$.

The range of $\boldsymbol{A}(R(\boldsymbol{A}))$, the null space of $\boldsymbol{A}^{\mathrm{T}}(N(\boldsymbol{A}^{\mathrm{T}}))$ and the null space of $\boldsymbol{A}(N(\boldsymbol{A}))$ are shown in figure 7.

Multiplying (2.82) on the left by $\boldsymbol{U}^{\mathrm{T}}$ we obtain

$$\boldsymbol{D}\boldsymbol{V}^{\mathrm{T}}\boldsymbol{x} = \boldsymbol{U}^{\mathrm{T}}\boldsymbol{c}. \tag{2.87}$$

Removing the secular part of $\boldsymbol{c}$, the part that is not in the range of $\boldsymbol{A}$, corresponds to putting to zero the elements of $\boldsymbol{U}^{\mathrm{T}}\boldsymbol{c}$ which occupy the same position as the zeros of $\boldsymbol{D}$ since the kernel of $\boldsymbol{A}^{\mathrm{T}}$ is spanned by the rows of $\boldsymbol{U}^{\mathrm{T}}$ which correspond to these positions. Then (2.87) can be solved for the other non-zero components and we get $\boldsymbol{x}' = \boldsymbol{V}\boldsymbol{D}^{-1}\boldsymbol{U}^{\mathrm{T}}\boldsymbol{c}$, where we replace the singular entries in $\boldsymbol{D}^{-1}$ by 0. By minimizing $\|\boldsymbol{A}\boldsymbol{x} - \boldsymbol{c}\|^2$, this solution chooses an $\boldsymbol{x}'$ so that $\boldsymbol{A}\boldsymbol{x}'$ is closest to $\boldsymbol{c}$, namely it solves (2.74) by replacing $\boldsymbol{c}$ by $\boldsymbol{c}_1 = \boldsymbol{c} - \boldsymbol{c}_2 = \boldsymbol{c} - (\boldsymbol{c}, \boldsymbol{v})\,\boldsymbol{v} = (\frac{1}{2}c^{(1)} + c^{(2)})\,(\frac{1}{2})$ in this example. Thus the generalized inverse algorithm arising from the singular-valued decomposition of $\boldsymbol{A}$ automatically takes account of the Fredholm alternative theorem. It therefore should have widespread application in situations for which one must go beyond the first order in the perturbation parameter to apply all the solvability conditions. After preparing the manuscript we learned that Chen & Joseph (1990) had also found the singular decomposition method to be extremely useful in obtaining and deriving solvability conditions of complex Ginzburg–Landau type.

There still remains a practical difficulty involving the conditioning of the matrix $\boldsymbol{A}$. The condition number of $\boldsymbol{A}$ is the ratio of highest to lowest non-zero singular values and if its square exceeds 10^8, serious numerical errors can arise. In our equations, the ratio of the differential operators representing diffusion effects in (2.39), (2.40), (2.41) to those involved in the continuity equation (2.42a) (the sign of this ratio is best seen from the vorticity formulation in which the pressure is eliminated; it can be as large as k^2N^2, N the number of terms in the Galerkin expansion) leads to a large and therefore poor conditioning number. It is wise, therefore, to use (2.42a) to eliminate the coefficients of $\tilde{u}_1'$ in terms of those in w_1 or vice versa. However, before one carries out this elimination, it is necessary to apply the solvability conditions to (2.82), namely to remove from the right-hand side of the continuity equation, the projection of the vector $\boldsymbol{c}$ in the null space of $\boldsymbol{A}^{\mathrm{T}}$. Once that part of $\boldsymbol{c}$ which arises from the continuity equation (2.42a) has been corrected, one

eliminates the coefficients of either $\tilde{u}_1'$ or w_1. The remaining system, which is essentially the algebraic system arising from (2.35), (2.40), (2.41), the horizontal and vertical momentum and heat equations, is then solved by the generalized inverse algorithm discussed previously.

The results are fairly spectacular and we have managed to achieve an accuracy of better than 1 % using a Galerkin basis of between six and ten modes in the vertical direction. More details of the numerics are given in Appendix C.

3. Results: comparison with previous theories, experiments and new predictions

In this section, we use the phase diffusion and mean drift equations to

(i) Reproduce the borders of the Busse balloon corresponding to long-wave (zigzag, Eckhaus and skew-varicose) instabilities to within an accuracy (as compared with the numerical results of Busse) of better than 1 %. The argument serves as a non-trivial check to our theory. Further, because we have explicit expressions for the growth rates of the instabilities and the shapes of the most unstable modes, we are able to understand their dependence on parameters.

(ii) Show that the maxima of the wavenumber distribution curves taken from the Heutmaker & Gollub (1987) experiment at $P = 2.5$ and the Steinberg *et al.* (1985) experiment at $P = 6.1$ agree exactly with our calculated values of k_B, the zero of the perpendicular diffusion coefficient and those of Buell & Caton (1986). This serves as an independent check on our results since the latter calculation was done in an entirely different manner by assuming that the total pattern was circular. In particular, a circular roll pattern is an exact solution of the phase diffusion, mean drift equations at all Prandtl numbers provided $k = k_B$. Further for $k < k_B (k > k_B)$, we shall show that the focus or umbilicus of a pattern will act as a source (sink) of rolls.

(iii) Argue, consistent with observation, that the onset of time dependence can occur for values of the Rayleigh number and the wavenumber k_B chosen by circular roll patterns well inside the Busse balloon.

(iv) Make a specific prediction, which appears to agree well with the observations of Steinberg *et al.* (1985), for the instability of a purely circular roll target pattern induced in a cylindrical container by thermally forced sidewalls. The discussion will involve some new thinking about the role of the amplitude order parameter near singularities. It is no longer slaved to the phase gradient at these points. In addition, it turns out that the non-slaved part of the amplitude parameter contributes significantly to the production of mean drift near the focus at moderate aspect ratios.

(v) Calculate the mean drift velocity fields for two deformed patterns: the circular roll pattern after it has gone through a focus instability and the straight roll pattern after it has experienced a skew-varicose instability. For the latter, we explicitly integrate (using a biharmonic term to regularize the phase diffusion equation) the equations and show clearly that the mean drift velocity field induced by the deformation of the straight roll pattern acts in a positive feedback manner. It advects the phase contours so as to enhance the narrowing of the distance between two phase contour maxima. It is clear that if we could safely continue the computation with suitable regularization terms, the phase contours would be forced to intersect and reconnections would be formed to create a pair of dislocations. We shall discuss the difficulties involved in using the equations close to this point in the conclusion.

3.1. *The instabilities of straight parallel rolls*

We begin with a linear stability analysis of the straight parallel roll solution

$$\Theta = k_0 X, \quad \psi = 0, \tag{3.1}$$

with constant k_0, by setting

$$\Theta = k_0 X + \Phi(X, Y, T), \quad \psi = \Psi(X, Y, T) \tag{3.2}$$

and linearizing the resulting equations to obtain

$$\Phi_T + \rho_0 k_0 \Psi_Y + \frac{1}{\tau_0}\frac{\mathrm{d}}{\mathrm{d}k}(kB)\Phi_{XX} + \frac{1}{\tau_0}B_0 \Phi_{YY} = 0, \tag{3.3}$$

$$\beta_0 \Phi_{XX} + \alpha_0 \Phi_{YY} = \left(\sigma(kA^2)' - \frac{1}{\tau}(kB_\alpha)' - B'_\beta\right)_0 \Phi_{XXY} + \left(\sigma A^2 - \frac{1}{k\tau_\alpha}B_\alpha\right)_0 \Phi_{YYY}, \tag{3.4}$$

where each of the coefficients is evaluated at k_0. First, let us check instabilities that are Y-independent. In this case, no mean flow is generated and stability is decided by the sign of the parallel diffusion coefficient $D_\parallel = (-1/\tau_0)(\mathrm{d}/\mathrm{d}k)(kB)_0$. For a perturbation

$$\Phi = \mathrm{e}^{\mathrm{i}kX + \gamma T}, \tag{3.5}$$

the growth rate γ is given by

$$\gamma = +\frac{1}{\tau_0}\left(\frac{\mathrm{d}}{\mathrm{d}k}kB\right)_0 K_x^2. \tag{3.6}$$

This is the Eckhaus instability. To examine the more general case for which the instability sets in with some Y-independence and for which $D_\parallel = (-1/\tau)(\mathrm{d}/\mathrm{d}k)\,kB > 0$, it is convenient to rescale

$$\tilde{\Psi} = \frac{\rho_0 k_0 \tau_0}{(-kB)'_0}\Psi$$

and obtain

$$-\frac{\tau_0}{(kB)'_0}\Phi_T + \tilde{\Psi}_Y - \Phi_{XX} - a\Phi_{YY} = 0, \tag{3.7}$$

$$\Psi_{XX} + c\Psi_{YY} = s\Phi_{XXY} - b\Phi_{YYY}, \tag{3.8}$$

where

$$a = \frac{B_0}{(kB)'_0} = \frac{D_\perp}{D_\parallel}, \tag{3.9}$$

$$c = \alpha_0/\beta_0, \tag{3.10}$$

$$s = \frac{\rho_0 k_0^2 \tau_0}{\beta_0(-kB)'_0}\left\{\sigma(kA^2)'_0 - \frac{1}{k_0\tau_\alpha}(kB_\alpha)'_0 - (B'_\beta)_0\right\}, \tag{3.11}$$

$$b = -\frac{\rho_0 k_0^2 \tau_0}{\beta_0(-kB)'_0}\left\{\sigma A^2 - \frac{1}{k_0\tau_\alpha}B_\alpha\right\}_0, \tag{3.12}$$

$$e = -\frac{\rho_0 k_0^2 \tau_0}{\beta_0(-kB)'_0}(B'_\beta)_0. \tag{3.13}$$

The last coefficient will enter the calculations for circular rolls. Substituting,

$$(\Phi, \tilde{\Psi}) = (\hat{\Phi}, \hat{\Psi})\exp(\mathrm{i}k_x X + \mathrm{i}k_y Y + \gamma T), \tag{3.14}$$

we obtain

$$\frac{\gamma}{K^2}\left(\frac{-\tau_0}{(kB)'_0}\right) = -1 - (a-1)S + \frac{S}{1+(c-1)S}(s - (s+b)S), \tag{3.15}$$

where $K^2 = K_x^2 + K_y^2$ and $S = K_y^2/K^2$.

For instability, we must have γ positive for some S, $0 \leqslant S \leqslant 1$. As we have seen, the purely Y-independent instability, the Eckhaus instability, occurs when $S = 0$ and $(kB)_0'/\tau_0$ is positive with the growth rate

$$\gamma = \frac{(kB)_0'}{\tau_0} K^2. \tag{3.16}$$

This instability dominates the right-hand border of the stability balloon for large Prandtl numbers (see figure 8*a*), the low-Rayleigh-number portion of the right border for moderate Prandtl numbers (see figure 8*b*) and the left border for very low Prandtl numbers (see figure 8*d*). A purely Y-dependent instability, called the zigzag instability occurs when $S = 1$ and its growth rate is given by

$$\gamma = \left(\frac{B_0}{\tau_0} + \rho_0 k_0^2 \sigma A_0^2\right) K^2. \tag{3.17}$$

From (3.17) and the fact that $\rho_0 < 0$, we see that the growth rate of the zigzag instability is lowered by finite-Prandtl-number, mean drift effects. This means one needs a strictly negative perpendicular diffusion coefficient $D_\perp = -B/\tau$ in order to trigger the instability and therefore the left stability boundary is moved to lower values of k. This can be seen by comparing the left border of the balloon in figure 8(*a–d*).

The skew-varicose instability occurs when the maximum growth rate γ is positive and for a value of S, $0 < S < 1$. Differentiating (3.15), we find

$$\frac{\mathrm{d}}{\mathrm{d}k}\frac{\gamma}{K^2}\left(\frac{-\tau_0}{(kB)_0'}\right) = -a + 1 + \frac{s - 2(s+b)S}{1+(c-1)S} - \frac{sS - (s+b)S^2}{1+(c-1)S^2}(c-1). \tag{3.18}$$

As our graph of c in figure 9 shows, it is close to unity for large ranges of the wavenumbers and Prandtl number. Therefore approximating c by 1, we see that a necessary condition for a skew-varicose instability is that

$$s > a - 1. \tag{3.19}$$

Both these and the other relevant quantities are plotted as a function of k at Prandtl number $P = 0.71$ and Rayleigh numbers $R = 1800$ and 3000 in figures 9 and 10. In graphing them, it turns out to be convenient to multiply them by a factor $D_\parallel$. A table of values of all these quantities at various Rayleigh and Prandtl numbers is given in Appendix D.

We note several features in figure 9.

(i) Observe that the value which $A^2 = \langle \tilde{u}_0^2 \rangle / k^2$ achieves at its maximum sharply increases with Rayleigh number from about 2 at $R = 1800$ to almost 6 at $R = 3000$. The graphs of kB have almost the same shape but slopes are significantly larger for the larger Rayleigh number.

(ii) ρ, the factor which accounts for the vertical averaging of the mean drift advection velocity in the phase diffusion equation, is almost constant and negative. Therefore in plotting mean drift velocities we always plot ρV.

(iii) For low Rayleigh numbers, c is almost constant and equal to one. This comes from the fact that the vertical structure of the mean drift profile is almost Poiseuille-like. Also, in that case, the left-hand side of (1.2) is the vertical vorticity. For $R = 3000$, c is not 1 but varies between 1 and 0.85.

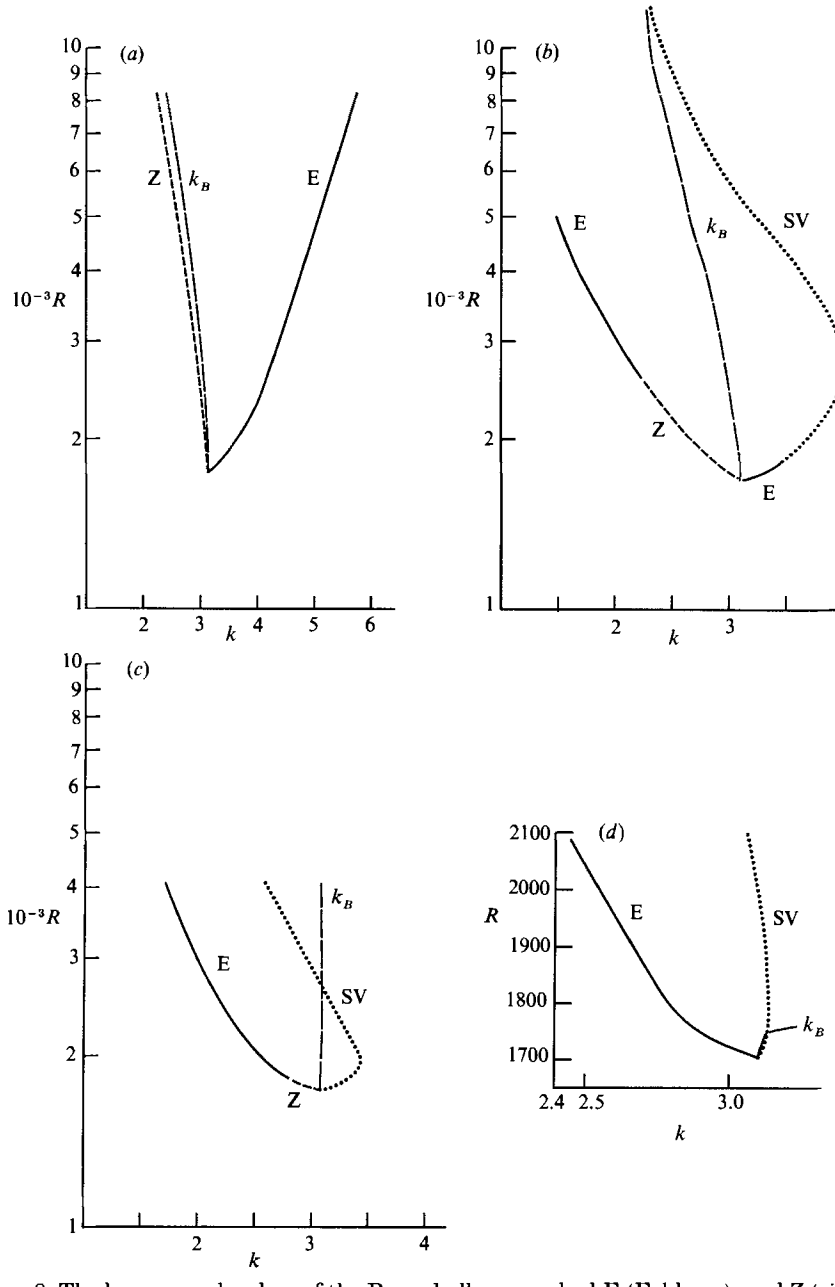

FIGURE 8. The long-wave borders of the Busse balloon marked E (Eckhaus), and Z (zigzag) and SV (skew-varicose) and the zeros k_B of $B(k)$ as calculated from (1.1), (1.2) for Prandtl number (*a*) 70, (*b*) 2.5, (*c*) 0.71 and (*d*) 0.1. The agreement with the calculations of Busse for the E, Z, and SV borders is so good that the two sets of curves superimpose exactly. In (*b*), the Eckhaus border for $P = 2.5$ is calculated accurately only to $R = 5000$. The skew-varicose border and k_B are calculated up to $R = 12000$ where they cross. Note that the two borders become close and run almost parallel from about $R = 7000$, the point where Heutmaker & Gollub (1987) observe the onset of time dependency. Observe that k_B crosses the SV boundary almost immediately for $P = 0.1$ suggesting that spatial and temporally chaotic behaviour will occur immediately after the conduction solution becomes unstable.

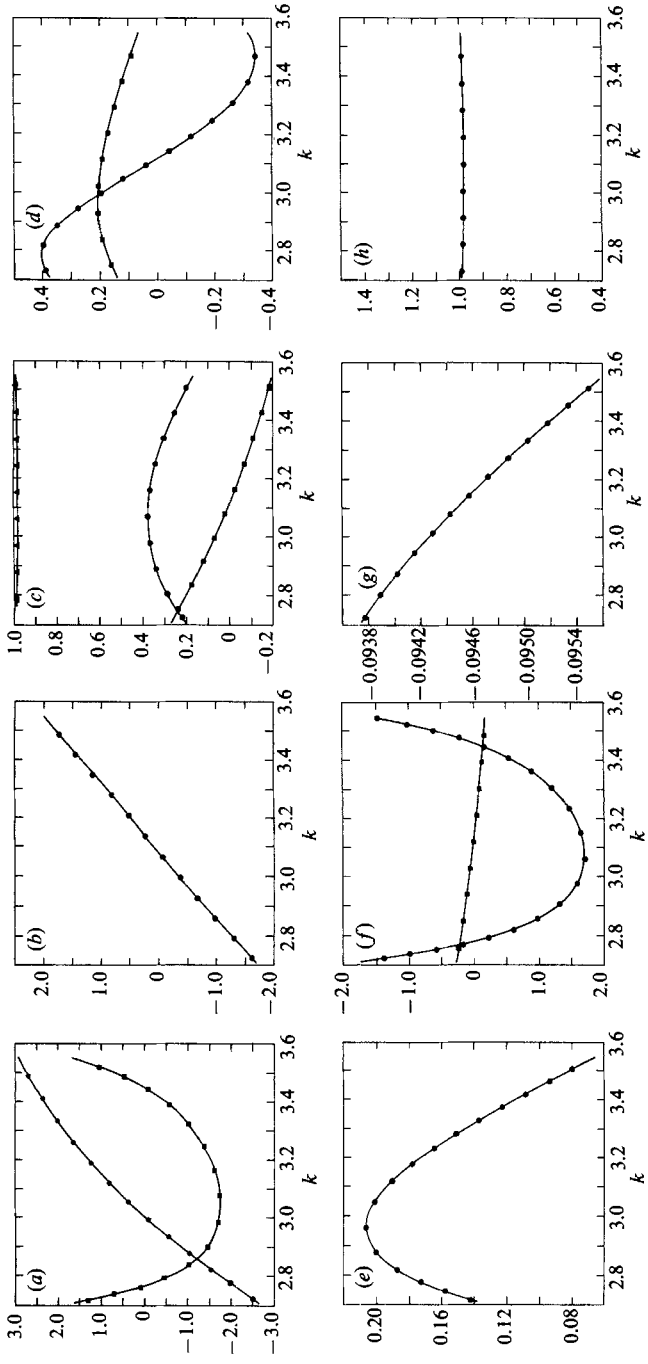

FIGURE 9. Graphs of (*a*) $D_\parallel s$ (circles), $a-1$ (squares); (*b*) $D_\parallel e$, (*c*) $D_\parallel b$ (circles), $-a$ (squares), *c* (triangles), (*d*) $kB(k)$ (circles), $A^2 = \langle \tilde{u}_0^2 \rangle / k^2$ (squares), (*e*) $A^2 = \langle \tilde{u}_0^2 \rangle / k^2$ on an expanded scale, (*f*) $D_\parallel$ (circles), $D_\perp$ (squares), (*g*) ρ, (*h*) *c*, (*i*) Nusselt number as functions of *k*; and (*j*), (*k*) growth rates of the various instabilities, as functions of $S = \sin^2(\tan^{-1}(K_y/K_x))$; for $R = 1800$, $P = 0.71$.

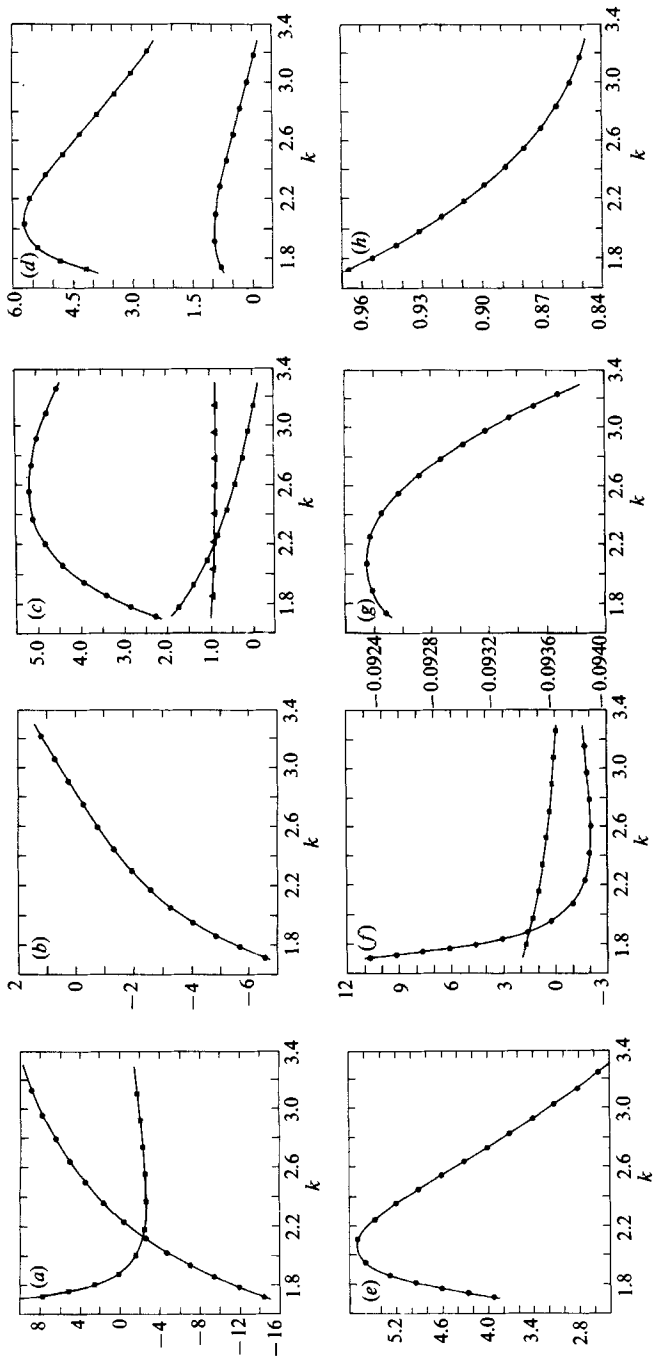

FIGURE 10. As figure 9, but for $R = 3000$, $P = 0.71$.

At this point, we want to make several remarks on the importance of the terms depending on B_α and B_β. These terms would have been absent had we assumed that the vertical structure of the mean drift velocity was determined principally by horizontal pressure differences and therefore has a Poiseuille-like ($\tilde{u}_1$, $\tilde{v}_1$ proportional to $\frac{1}{4}-z^2$) profile. Indeed we originally made this approximation and were initially encouraged by the fact that our errors on the borders of the Busse balloon were less than 10%. However, this accuracy was fortuitous and a closer examination of $\tilde{u}_1$, $\tilde{v}_1$ revealed that the coefficients of Θ_{XX}, Θ_{XY}, Θ_{YY}, Θ_T in $\tilde{u}_1$, $\tilde{v}_1$, were equally important to those of $(\boldsymbol{kx}\nabla\psi)\cdot\hat{\boldsymbol{z}}$ and $\hat{\boldsymbol{k}}\cdot\nabla\psi$. Indeed the terms $(1/k\tau_\alpha)(kB_\alpha)'$, B'_β and B_α are of the same order as $\sigma(kA^2)'$ and σA^2 respectively.

The second remark concerns the infinite-Prandtl-number limit $\sigma\to 0$. On the surface the disappearance of terms involving B_α, B_β in the mean drift equation is not obvious because not all terms in c_{ij} and e_{ij} in (2.72)–(2.74), (2.77)–(2.79) contain σ, the inverse Prandtl number, as a factor. Nevertheless, it can be shown that in the limit $\sigma\to 0$, B_α and B_β cancel, and no mean drift is generated.

Finally, we describe the result of integrating the phase diffusion and mean drift equations (1.1) and (1.2) beginning with a small initial perturbation which leads to a skew-varicose instability. We take as initial state, for $P = 1$ and $R = 2500$,

$$\Theta = k_0 X + 0.001\cos(X+Y) \tag{3.20}$$

with $k_0 = 3.4$, together with the corresponding mean drift field Ψ calculated using the approximation $c = 1$. Since we are outside the stability balloon, (1.1) and (1.2) have the character of the reverse heat equation and will therefore preferentially amplify the smallest scales. In order to control and indeed damp these scales, we add the biharmonic term $\mu\nabla^2\Theta$ to (1.1), in order to regularize the equation. The magnitude of μ, which is proportional to the square of the inverse aspect ratio ϵ, reintroduces a lengthscale into the problem by essentially indicating how large the container is compared to the roll wavelength. Such a correction term is indeed present in the final multiple scale expansion if carried out to the next order in the inverse aspect ratio, as was shown by Cross & Newell (1984) in the context of several model equations. A more important correction is present in the amplitude equation converting it from an algebraic equation where A is slaved to k to a differential one in which the amplitude is an independent order parameter. However, because of the complexity of the full Oberbeck–Boussinesq equations, it is extremely difficult to carry out that step here. Nevertheless it is a step that should ultimately be taken because it turns out that while the linear regularization is good enough to allow the instability to develop to a finite-amplitude state in which the phase contours are distorted in such a way that one sees that they apparently want to form dislocation pairs, it does not let us get sufficiently close to the singular state in order to study the details of the breaking and reconnection of the phase contours. We conjecture, but at the moment this is as much of a hope as a rational deduction, that, for sufficiently small ϵ, the results will be independent of the exact details of the amplitude regularization and only depend on a certain canonical form. This will be discussed further in §4. In figure 11, we show the phase contours and superimposed mean drift field at two values of μ, 0.05 and 0.2, at the last time before the wavenumber k goes outside the marginal stability boundary in the regions of strong phase gradients. It is clear from these pictures that the induced mean drift field acts in a manner to enhance the production of strong phase gradients and the necking of contours.

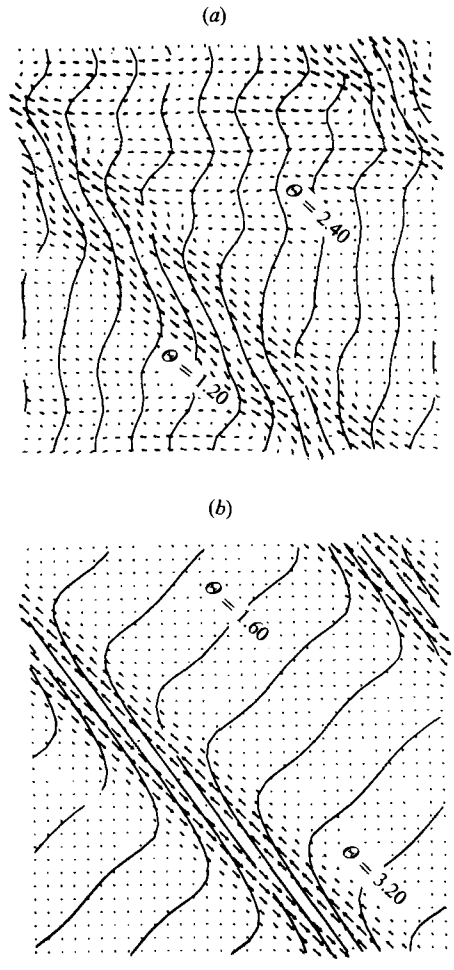

FIGURE 11. Graphs of phase contours, initiated as $\Theta = 3.4X + 0.001\cos(X+Y)$, $0 < \epsilon \ll 1$ with corresponding mean drift velocity field as calculated from (1.1), (1.2) superimposed, for (*a*) $\mu = 0.05$ and (*b*) $\mu = 0.2$ at $P = 1$ and $R = 2500$.

3.2. *Circular roll patches and their deformations*

Because of the influence of sidewall boundaries, patches of almost circular rolls tend to be the dominant convection pattern observed in large-aspect-ratio containers. It is, therefore, natural to investigate whether there are equilibrium solutions and instabilities peculiar to these geometries which are not part of the repertoire arising from the deformation of straight roll patterns.

The first important property to note is that curved and, in particular circular, roll patches, as opposed to straight rolls, select a wavenumber, an observation first made by Pomeau & Manneville (1981). A calculation of the selected wavenumber k_B at finite Prandtl numbers near threshold was done by Cross (1983) and at finite Prandtl and Rayleigh numbers by Buell & Caton (1986). Their idea was to expand the circularly symmetric solution in powers of $1/r$ and then determine the wavenumber by the solvability condition at first order. In our theory, in the infinite Prandtl number case, we see that it is simply the curvature of the rolls that induces this selection. At finite Prandtl number, we must assume that the pattern is circular.

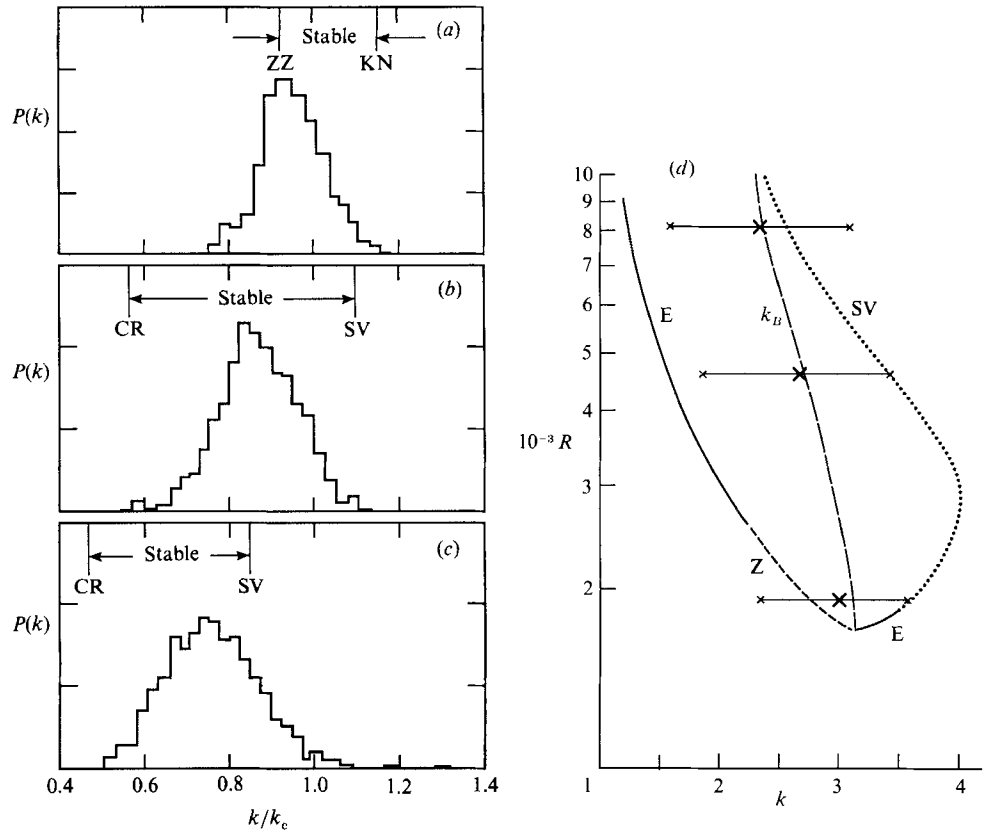

FIGURE 12. (*a–c*) From Heutmaker & Gollub (1987), showing the distribution of wavenumber for $P = 2.5$ at (*a*) $R = 1.1R_c$, $\epsilon = 0.01$, (*b*) $R = 2.61R_c$, $\epsilon = 1.61$, and (*c*) $R = 4.64R_c$, $\epsilon = 3.64$. In (*d*), the maxima (marked with $\times$) and the support of the wavenumber distribution are superimposed on figure 8(*b*), the Busse balloon. Note that the maxima are at k_B. Observe that at $R = 2.61R_c$, where the states achieve equilibrium, the wavenumber band number lies entirely in the balloon, whereas at $R = 4.64R_c$, a significant number of rolls have supercritical wavenumbers.

Then it is an easy exercise to show that no mean drift is produced and therefore, from (1.1),

$$\frac{\partial \Theta}{\partial T} + \frac{1}{\tau r}\frac{\partial}{\partial r} rkB = 0. \tag{3.21}$$

In particular, if the pattern is stationary

$$rkB(k) = \text{constant} \tag{3.22}$$

and in order that (3.22) holds arbitrarily close to the pattern centre, the constant is zero to leading order; it may be of order ϵ, the inverse aspect ratio, reflecting the order-ϵ corrections to (1.1). Hence k is chosen so that $B(k) = 0$. This wavenumber, the zero of $D_\perp = (-1/\tau(k))B(k)$, we call k_B. As we have seen in figure 8, we can calculate k_B as function of Rayleigh number at each Prandtl number. We now compare this theoretical result with the observations of the wavenumber distribution as function of Rayleigh number, as measured in experiments by Heutmaker & Gollub (1987) and Steinberg *et al.* (1985) at Prandtl numbers 2.5 and 6.1 respectively.

The Heutmaker–Gollub experiment uses natural convection in cylindrical containers, and as we have seen in snapshots taken at several Rayleigh numbers, while the patterns have many features, they are dominated by circular patches.

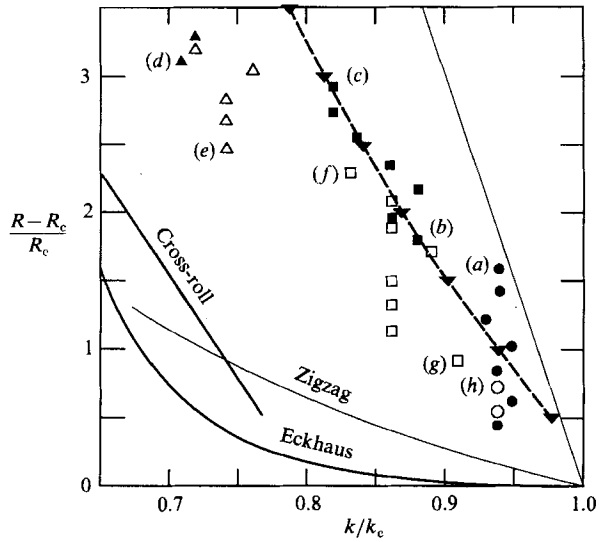

FIGURE 13. Taken from Steinberg *et al.* (1985), showing the wavenumbers (as measured by $2\pi/\lambda$, where λ is the width of the second pair of rolls from the wall) of the $3\frac{1}{2}$ (●), 3 (■), $2\frac{1}{2}$ (▲) roll equilibrium states as functions of Rayleigh number as the Rayleigh number is increased. Open symbols denote the same states achieved as the Rayleigh number is decreased. Superimposed are the zigzag, Eckhaus, and cross-roll stability boundaries, the prediction of the wavenumber by small-amplitude theories (light line) and our predictions (——).

The wavenumber distribution of three values of the Rayleigh number, $R = 1.1R_c$, $R = 2.61R_c$ and $R = 4.64R_c$ are shown in figure 12(*a–c*). In figure 12(*d*), we show the maxima of these distributions and the ranges of support of the wavenumber distribution (the values of k where it is non-zero) superimposed on figure 8(*b*), the Busse balloon. Note first that our theoretical calculation of k_B agrees almost exactly with the maxima at all three Rayleigh numbers. This suggests that, even at low and moderate Prandtl numbers, the zero of $B(k)$ plays an important role. However, it is not completely dominant and there is a range of wavenumbers. Some spread in wavenumber, of the order of the inverse aspect ratio, can be expected by simply including the mean drift field, but this is not enough to explain the observed distribution width. Wavenumbers less than the maximum are caused by the decrease of wavenumber around defects and along boundaries as the pattern attempts to adjust to the boundary conditions (at moderate Rayleigh numbers). Wavenumbers greater than the maximum are due to the compression of rolls. Roll compression is caused by several mechanisms, sidewall boundary conditions and more importantly the focus instability, and each will induce a mean drift field. Notice that on figure 12(*d*), the support of the wavenumber distribution lies inside the Busse balloon at $R = 2.61R_c$ and partially outside at both $R = R_c$ and at $R = 4.64R_c$. We return to this observation shortly when we discuss the onset of time dependence.

The Steinberg *et al.* (1985) experiment involved the initiation of circular target patterns (as shown in figure 4*d*, *e*, *f*) by sidewall forcing. In figure 4(*e*), we see a stable circular target pattern with three roll pairs at values of R of about $3R_c$. In figure 4(*f*), the target pattern has shifted off-centre but still has three roll pairs. They estimate that the off-centre shift of the umbilicus begins for values of R about $3.5R_c$ and the shift increases monotonically as with R. We shall come back to the reason for this shift shortly but at this point we draw the readers' attention to figure 13, taken directly from Steinberg *et al.* (1985). In figure 13, the solid circles (squares, triangles)

denote the values of k (as measured by $2\pi/\lambda$, the wavelength of the second roll pair from the walls) in a pattern containing $3\frac{1}{2}(3, 2\frac{1}{2})$ roll pairs as R is increased. The open symbols of the same type correspond to decreasing R. The zigzag and cross-roll instabilities are shown on the left and the prediction of the dominant wavenumber by a small-amplitude calculation is shown on the right. Our calculation of k_B is shown as a boldfaced hatched line. The agreement with the observed dominant wavenumber again strongly suggests that there is a tendency for almost circular patterns to select k_B, the zero of the perpendicular diffusion coefficient $D_\perp = -(1/\tau(k))\,B(k)$. We cannot prove, as yet, that (1.1), (1.2) have a Lyapunov functional which naturally leads to this selection, but remind the reader that in 1984, Cross & Newell pointed out that the functional

$$F = \iint\left(-\frac{1}{2}\int^{k^2} B\,\mathrm{d}k^2\right)\mathrm{d}X\,\mathrm{d}Y \tag{3.23}$$

acts as a Lyapunov functional in the infinite-Prandtl-number limit as long as dislocations are stationary when $k = k_B$, which in this case is the zigzag instability border of the Busse balloon.

Next we ask what happens if we allow the circular patterns to be time dependent. In that case, if we take k to be a fixed value k_0,

$$\frac{\partial\Theta}{\partial T} = -\frac{1}{\tau_0}k_0 B_0 \frac{1}{r}, \tag{3.24}$$

which shows that Θ decreases for $k < k_B$ where $(1/\tau_0)\,k_0 B_0$ is positive and increases for $k > k_B$ where $(1/\tau_0)\,k_0 B_0$ is negative. Since in writing down (3.24), we have chosen the $\boldsymbol{k}$ in $\boldsymbol{\nabla k} B$ to be k_0, k_0 positive, the phase contours have increasing value as r increases. Therefore a decreasing Θ at fixed r means the phase contour at that value of r has been replaced by one from the inside. Therefore the focus singularity (umbilicus) is acting as a source of new rolls. On the other hand, for $k > k_B$, the umbilicus acts as a sink. Suppose the wavenumber near $r = 0$ is $k_B + \Delta k(r)$. Then for Δk, v small, the exact solution $\Theta = k_B + \int^r \Delta k(r)\,\mathrm{d}r + vT$ gives

$$\frac{-k_B B'(k_B)}{\tau(k_B)}\Delta k(r) = v\tfrac{1}{2}r. \tag{3.25}$$

Therefore when the focus acts as a source (sink) $v > 0$ (< 0), namely when the wavenumber near $r = 0$ is less (greater) than k_B, the wavenumber correction $\Delta k(r)$ increases (decreases) with r so that the wavenumber in the outer part of the circular patch always has the tendency to move towards k_B.

We next carry out a linear stability analysis of a stationary circular patch by setting

$$\Theta(r, T) = k_0 r + k_0 D(r, t)\sin m\theta, \quad \frac{\rho_0\tau_0}{k_0 B_0'}\psi(r, T) = \phi(r, t)\cos m\theta, \tag{3.26}$$

where $r = (X^2 + Y^2)^{\frac{1}{2}}$, $\tan\theta = Y/X$, the time t is rescaled as $-(\tau_0/k_0 B_0')\,t$, and we shall choose k_0 to be k_B, the zero of $B(k)$. (Note on notation: The use of t and θ as rescaled horizontal diffusion time and circular angle are different from the t, the original dimensionless time in the Oberbeck–Boussinesq equations and $\theta = \Theta/\epsilon$, the phase, used in §2.) Before we discuss the calculation, we want to mention a small but subtle difficulty involving the singular nature of the polar representation of the field in terms of amplitude and phase at the origin $r = 0$. Note that the undisturbed phase $\Theta_0 = k_0 r$ has a discontinuity in derivative on any ray through the origin. This of

course is necessary to ensure that the phase increases along any ray from a chosen value, say zero, at the origin. We want the perturbed field $\Theta_0+\Delta\Theta$ to have the same property, namely that the phase increases on any ray emanating from its new zero point. For example, if the umbilicus is shifted from $X=0$, $Y=0$ to $X=0$, $Y=-D$, then on the ray $X=0$, we want to choose $\Theta=k_0(Y+D)$ for $Y>-D$ and $\Theta=-k_0(Y+D)$ for $Y<-D$. Mathematically this difficulty can be overcome by considering a function of phase, like $w(X,Y)=\cos\Theta$, which represents a real field variable, such as velocity or temperature. Observe that whereas the translation modes $\partial\Theta/\partial X$, $\partial\Theta/\partial Y$ of the phase are discontinuous at the origin, the translation modes of w are continuous. If we write $w(X,Y+D)$ as $w(X,Y)+D\,\partial w/\partial Y$, where $w(X,Y)$ is $\cos k_0(X^2+Y^2)^{\frac{1}{2}}$ and then invert we would obtain $\Theta=\cos^{-1}w(X,Y)+D\,\partial\Theta_0/\partial Y$, and $\partial\Theta_0/\partial Y=k_0\,\mathrm{sgn}\,Y$. The important point to make is that one must chose the sign of $\cos^{-1}$ so that along a ray Θ is always positive. Therefore the representation $\Theta=k_0 r+k_0 D(r,t)\sin m\theta$ is fine as long as we remember that Θ is positive. We want to emphasize the point here of introducing a continuously differentiable function of Θ like cosine because very similar considerations are important when we consider the nature of the relevant order parameters near defects.

We linearize the equations in D and ϕ and, after a little calculation, find that (1.1) and (1.2) become

$$D'_t-(D')_{rr}-\frac{1}{r}(D')_r+\frac{1}{r^2}D'=m\left(\frac{\phi}{r}\right)_r \tag{3.27}$$

and

$$\phi_{rr}+\frac{1}{r}\phi_r-\frac{m^2c}{r^2}=ms\frac{(rD')\,r}{r^2}-me\frac{D'}{r^2}+m(m^2-1)\,b\frac{D}{r^3} \tag{3.28}$$

respectively. In (3.27), (3.28), c, s, e, b, are exactly the same quantities as were defined in the previous section (§3.1) and D' is $\partial D/\partial r$. The wavevector $\boldsymbol{k}$, in circular coordinates, is

$$\boldsymbol{k}=k_0(1+D'\sin m\theta),\, mk_0 D/r\cos m\theta, \tag{3.29}$$

and the effective mean drift velocity field $\rho\boldsymbol{V}$ which advects the phase contours is

$$\rho\boldsymbol{V}=\frac{-B'_0}{\tau_0}\left(-\frac{m}{r}\phi\sin m\theta,\,-\phi_r\cos m\theta\right). \tag{3.30}$$

Before we discuss the boundary conditions, we must understand the extent to which the stability problem can be considered by appealing to the phase equation alone. First, there are no boundary conditions natural to the phase equation in a finite geometry except that an integer number of rolls fit in the box. If, during the instability process, the number of rolls is conserved, then D is zero at the boundary. Second, observe that the phase equation to this order does not contain the aspect ratio. By choosing to non-dimensionalize length with the radius of the container so that its boundary is $r=1$, the stability of circular patterns would appear to be independent of aspect ratio for container width ϵ^{-1}. We shall see that this is only the case when ϵ is sufficiently small, and that the number of rolls n in the container sufficiently large that $1/n$ is an order of magnitude less than the width of the stability band of the Busse balloon. In order to bring the effects of finite ϵ back in the model, and obtain an approximate boundary condition on D' at $r=1$, and, most important, to describe correctly the behaviour of the patterns near the focus singularity, we reintroduce the amplitude as an active order parameter to regularize the phase equation. The details are given in Appendix E. Here we survey the main points. The natural boundary condition on the amplitude A at $r=1$ is $A=0$. The mean drift

velocity V should also have a zero normal component there. Therefore $\boldsymbol{k} \cdot \boldsymbol{V}$ will be at most order ϵ at the boundary, so that $(\partial/\partial r)\, rkA^2F(k)\,(B(k) = A^2(k)\,F(k)$ when the amplitude A is slaved to k) must be zero to leading order. This gives us that $rkA^2F(k)$ is constant and the boundary conditions on A make this constant zero or at most of order ϵ. Outside a boundary-layer width ϵ at $r = 1$, therefore, we must have that k approaches the zero k_B of $F(k)$ to within order ϵ. Therefore, for ϵ small, it is entirely reasonable to impose the boundary conditions $D' = \phi = 0$ at $r = 1$. At $r = 0$, we must match the outer solution which is governed by (3.27), (3.28) to a boundary layer in which the amplitude is an active order parameter, for which details are given in Appendix E. This matching allows us to control the behaviour of D' as $r \to 0$. Without this control D' will oscillate infinitely fast as $r \to 0$ in the unstable case. The relevant boundary conditions are that both D' and the perturbation amplitude are zero at $r = 0$. However, for small ϵ, the stability result depends only weakly on the exact structure of the amplitude equation and on the nature of the solutions in the ϵ layer about $r = 0$.

With these considerations in mind, we return to a qualitative analysis of (3.27), (3.28) for the case of the most unstable mode $m = 1$. We will ignore the term eD'/r^2 (for moderate Prandtl numbers, this is a reasonable approximation, see the table in Appendix D) and take c equal to unity, which is a good approximation for almost all values of P and R. We can now solve (3.28) exactly,

$$\phi = rs \int_1^r \frac{D'}{r^2}\,\mathrm{d}r, \tag{3.31}$$

and, from this, we see that the term on the right-hand side of the phase diffusion equation (3.27) which represents the advection of wavenumber is

$$s\frac{D'}{r^2}. \tag{3.32}$$

For positive s, this term acts to increase the wavenumber, while the terms

$$\frac{\partial^2}{\partial r^2}D' + \frac{1}{r}\frac{\partial}{\partial r}D' - \frac{D'}{r^2}$$

are simply the r-derivative of the parallel diffusion $(1/r)/(\partial/\partial r)(rD')$ term in (1.1). The mean drift field has the shape of a dipole

$$\rho \boldsymbol{V} = \frac{-B_0' s}{\tau_0}\left[-\left(\int_1^r \frac{D'}{r^2}\,\mathrm{d}r\right)\sin\theta, -\left(\int_1^r \frac{D'}{r^2}\,\mathrm{d}r + \frac{D'}{r}\right)\cos\theta\right]. \tag{3.33}$$

Observe that near $r = 0$, the azimuthal velocity is bounded (the focus centre does not act like a vortex) whereas the radial velocity is $(-B_0' s/\tau_0)(D'(0)/r)\sin\theta$. Instability occurs when the production of wavenumber by sD'/r^2 on the side of the circular pattern on which the rolls are compressed overcomes the diffusion of wavenumber. If we write $D'(r,t) = y(r)\,\mathrm{e}^{\sigma t}$, we obtain

$$\sigma y = \frac{\partial^2}{\partial r^2}y + \frac{1}{r}\frac{\partial}{\partial r}y - \frac{(1-s)}{r^2}y, \tag{3.34}$$

from which we find

$$\sigma \int_0^1 ry^2\,\mathrm{d}r = -\int_0^1 ry'^2\,\mathrm{d}r - (1-s)\int_0^1 \frac{y^2}{r}\,\mathrm{d}r. \tag{3.35}$$

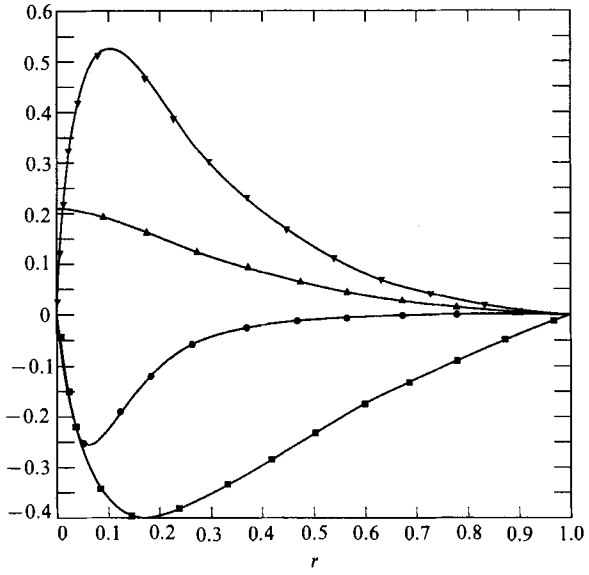

FIGURE 14. Graph of $y(r)$ (■), $w+s_2 y$ (●), $D(r)$ (▲), and $\phi(r)$, (▼).

R/R_c	k_B/k_c	s	e	c	b
1.5	0.98	0.33	−0.03	1.00	0.19
2.0	0.94	0.64	−0.09	0.99	0.39
2.5	0.89	0.91	−0.16	0.99	0.59
3.0	0.85	1.13	−0.20	0.99	0.79
3.5	0.82	1.29	−0.26	0.99	0.96
4.0	0.79	1.45	−0.29	0.99	1.13
4.5	0.76	1.59	−0.31	0.98	1.28

TABLE 1. Values of k_B, s, d, c, b estimated at k_B for $P = 6.1$

As we have explained, since the amplitude variations are confined to the boundary layers, stability or instability is determined to leading order by the balances involved in (3.34), (3.35). In particular we note that stability is guaranteed if $s < 1$. The subtlety involved in determining a sufficient condition for instability is as follows. If we take (3.34) on its own and take the boundary conditions that $y(1) = 0$ and $y(0)$ is bounded, then for $s > 1$ we are led to solutions which oscillate infinitely fast as $r \to 0$ and for which there is a continuous positive spectrum σ. Moreover, if we take (3.35) literally, we see that the second integral dominates the first and so it would appear that a sufficient condition for instability is indeed that $s > 1$. However, this is not quite the case because the problem is singular and the outer solution for $1 > r > O(\epsilon)$ does not oscillate as $r \to 0$ but grows towards an algebraic or logarithmic singularity before turning back to zero within the boundary layer (see figure 14). For $s < 1$, the stability region, we find that the solution approaches $r = 0$ with zero derivative. At $s = 1$, its derivative is unity. As s exceeds unity, the behaviour of y seems to vary from logarithmic $(-\ln r)$ to a power law divergence $(r^{-\alpha}, \alpha > 0)$. (We stress, however, that in all cases, the solution turns back to zero in the boundary layer.) If the divergence is logarithmic, thus one again would expect the second term on the right-hand side of (3.35) to dominate the first and obtain $\sigma > 0$. Most of our

numerical calculations for $s > 1$ seem to indicate that the first term in (3.35) has a stabilizing effect (in many cases the ratio of $\int_0^1 ry'^2\,\mathrm{d}r$ to $\int_0^1 (y^2/r)\,\mathrm{d}r$ was $\frac{1}{3}$) and so instability requires $s > 1$, and perhaps about $\frac{4}{3}$. For now, all we can definitely say is that the focus instability is initiated for a value of s close to but somewhat greater than unity, and leave the extremely subtle mathematical analysis to a later paper. However, we do emphasize that the instability will be triggered well inside the confines of the Busse balloon and therefore will be of importance in understanding the dynamics of patterns. For example, for $P = 2.5$, s exceeds unity at $R = 2750$. It is certainly important in the target pattern in the experiment of Steinberg *et al.* (1985) where $P = 6.1$ (see figures 4*d*, *e*, *f* and 13). New phase contours are not created by this focus instability but the phase contours are compressed on the side toward which the dipole-shaped mean drift velocity advects them. The phase contours are spread out on the other side (see figure 4*f*). In table 1 we give the values of k_B and s, c, b for Rayleigh numbers $R = 1.5R_c$ to $4.5R_c$ at $P = 6.1$. We observe that the critical parameter s reaches unity at about $R = 2.7R_c$. However, as we have mentioned, the first term in (3.29) will delay onset of the focus instability by an amount which, using a trial shape for D', we estimate to be approximately $\frac{1}{3}$ (the ratio of $\int_0^{r_c} r(D')_r^2\,\mathrm{d}t$ to $\int_0^{r_c} (1/r)\,D'^2\,\mathrm{d}r$). The critical value of s would thus be about 1.33. We observe that this corresponds to a Rayleigh number of $3.5R_c$ which is consistent with the value at which Steinberg *et al.* observe that their circular pattern, figure 4(*e*) (point *b* in figure 13) begins to deform towards figure 4(*f*) (point *c* in figure 13). The structure of the unstable mode is calculated in Appendix E and shown in figure 14. We have not yet done any finite-amplitude analysis on this instability but, from the experimental evidence of Steinberg *et al.*, the instability would seem to be saturated at finite amplitude. The amount by which the umbilicus of the pattern shifts off-centre will be a monotonically increasing function of the difference between R/R_c and that value at which the focus instability is first triggered. G. Ahlers (private communication) has experimental data on this and we hope to be able to present a comparison of the results of the finite-amplitude theory with experiment in a later paper.

3.3. *The onset of time dependence*

Based upon the experimental evidence and the analyses presented in §§3.1, 3.2 we shall now discuss the factors that appear to be important in initiating time dependence and raise some questions which will need to be answered before certain difficulties are satisfactorily resolved. Our starting point is a list of observations and remarks:

(i) The phase diffusion equation (1.1) involves three terms. Time dependence is represented by Θ_T, mean drift advection by $\rho V \cdot k$ and wavenumber diffusion by $1/\tau \nabla \cdot kB(k)$. In the absence of mean drift, as would be the case at infinite Prandtl number or in circular roll patterns, the last term causes curved roll patterns to relax to a circular pattern with preferred wavenumber k_B. In the presence of mean drift no such choice is imposed by the dynamics and stationary patterns can be achieved through a balance of mean drift and diffusion terms.

(ii) In natural convection patterns, the container cannot be tiled with a texture in which the wavenumber is everywhere constant. Therefore the diffusion term is never everywhere zero and the pattern must be time dependent or produce a mean drift which can balance the diffusion or both.

(iii) The boundary condition which forces the roll axes at the boundary to be along its normal gives rise to patches of almost circular patterns in natural convection situations. In between the patches, there is considerable forcing for the mean drift

flow. However, the patches themselves are clearly circular. The stability or instability of exactly circular patterns is therefore very important because it tells us whether, within an almost circular pattern, the distortion and the mean drift (and it is the mean drift within the patch which is important) are maintained by the forcing of boundaries (if the constant phase contours are normal to the boundary, they cannot at the same time be circles which maintain a constant distance between them) or if the mean drift component is naturally induced by an instability. In the former case, the magnitude of the mean drift flow is determined by a balance involving how well the boundary forcing overcomes the natural tendency of the patch to achieve a circular shape. In Appendix E, we show that until the focus instability Rayleigh number is reached, this attenuation can be considerable. In the latter case, the magnitude of the mean drift component is determined by a finite-amplitude saturation of the unstable deformation. We expect the latter to grow by an amount proportional to some power of $R-R_{\mathrm{F}}$ (probably $(R-R_{\mathrm{F}})^{\frac{1}{2}}$) where R_{F} is the Rayleigh number at which the focus instability is triggered. For a sufficiently large Rayleigh number (although, we have indicated, still within the confines of the Busse balloon), the focus instability has to be important.

(iv) For a sufficiently large deformation of the circular pattern, the rolls on one side can be compressed so that their wavenumber lies far enough outside the skew-varicose instability boundary calculated for straight rolls in an infinite horizontal geometry that this instability can be initiated and dislocations nucleated.

(v) A circular target pattern with wavenumber $k \neq k_B$ can do one or a combination of three things. It can remain axisymmetric and become time dependent and nucleate or absorb rolls in the focus until either $k = k_B$ or k is as close to k_B (within one roll) as the finite container size will allow. It can develop a non-uniform but still axisymmetric wavenumber distribution with $k > k_B$ almost everywhere and adjust the wavenumber in the boundary layer at $r = 0$ by allowing the amplitude to become an independent order parameter. (To be specific, we may ask for stationary, axisymmetric solutions of (E1), (E2), (E3)). These two situations may be related, and for small enough ϵ, the latter may lead to the former. In a container with moderate aspect ratio (say $\epsilon = 0.2$) the incremental jump Δk in wavenumber induced by introducing or taking away a roll or roll pair may be comparable with the width of the stable band of wavenumbers and consequently it may be easier for the amplitude to make the necessary adjustment in a reasonably large boundary layer. As ϵ decreases, however, it may be difficult for the amplitude to adjust and remain time independent. Instead the large-amplitude gradient can help product an extra roll. The third response is that the pattern break its circular symmetry and develop a mean drift flow which balances the diffusion term. We remark that if k is very close to k_B or can become so by the nucleation or absorption of rolls, the last possibility is unlikely if the circular pattern is strongly stable with respect to the focus instability.

(vi) In order to sustain a time dependence on this dissipative system, at the very least one requires in the phase space either one unstable fixed point with a homoclinic orbit or two unstable fixed points where the unstable manifold of one intersects the stable manifold of the other. We have already alluded to the unstable fixed point connected with the skew-varicose instability, the neighbourhood of which is reached via roll compression. We have also indicated that the skew-varicose instability leads to the nucleation of a dislocation pair which climbs to the lateral sidewall and disappears there or glides along the boundary to disappear in the foci. The stress on the pattern is relieved. The mean flow subsides. How does the system return to the

state so that the skew-varicose instability is again initiated? Equivalently, how did it get there in the first place? Is there another unstable fixed point? Or, what is responsible for the homoclinic cycle emanating from the skew-varicose instability?

There has been no clear discussion in the literature of this last point except for the paper of Croquette, Le Gal & Pocheau (1986*a*) in the case of the time dependency seen near threshold values of the Rayleigh number for $P = 0.71$. In this range of values, the forcing from the boundary conditions is strong because the angle between the roll axis and sidewall normal is a sensitive function of Rayleigh number. At onset, the rolls are almost straight and violate the boundary condition severely (see figure 3*a*). However, as the Rayleigh number increases, the boundary condition becomes more enforced and the phase contours become more curved, as shown in figure 3(*b*). This bulge compresses the rolls in the centre and the skew-varicose instability is initiated. When the stress on the pattern is relieved, the rolls attempt to relax to a straight roll state (as in figure 3*a*) but the boundary condition again forces the phase contours to bulge, a new roll is nucleated at the focus, and the cycle is repeated.

However, for circular target patterns (figure 4), and for natural convection patterns at moderate Prandtl number for which the time dependence occurs at finite Rayleigh numbers and at which point the boundary conditions have already forced almost circular patches, the mechanism for setting up the mean flow has not been clearly established. Let us first discuss the circular target pattern case in the limit of very large-aspect-ratio containers. In these cases, the increment Δk in k caused by the addition or subtraction of one roll is very small compared with the width of the stability band of the Busse balloon. Suppose now that the Rayleigh is raised past the point R_{F} at which the focus instability occurs. At a certain finite Rayleigh number R_{sv} greater than R_{F}, the finite-amplitude equilibrium state representing a balance between mean drift and wavenumber diffusion will compress the rolls in the outer regions sufficiently to nucleate a dislocation pair (figure 4*b*). Note from Appendix E that the largest compression is not at the outer boundary. The dislocations glide to the focus and disappear, leaving the pattern again circular with no mean drift and one less roll pair. Now if the new wavenumber of the pattern is less than the value of k_B at the Rayleigh number R_{sv}, then new rolls will be nucleated at the focus and the system will be returned to the same unstable state from which the off-centre shift of the umbilicus originally occurred. The cycle repeats. For smaller aspect ratios, the incremental changes in wavenumber are correspondingly larger and it may very well be that the wavenumber of the new circular target pattern state at R_{sv} is stable at this value of Rayleigh number. In this case, the second unstable state has disappeared, there is insufficient forcing and the pattern does not remain time dependent but relaxes to a new fixed point.

For higher Prandtl number, the removal of a roll may be due to an Eckhaus rather than a skew-varicose instability. Indeed it would appear that in the Steinberg *et al.* (1985) experiment where $P = 6.1$ this is indeed the case in the transitions from $3\frac{1}{2}$ to 3 roll pairs and from 3 roll pairs to $2\frac{1}{2}$ roll pairs. We calculated the stability boundaries for $R = 3.5R_{\mathrm{c}}$ and $P = 6.1$ and found that $k_{\mathrm{sv}} = 4.6$ and $k_{\mathrm{E}} = 5.4$. However, because of the finite aspect ratio, it is difficult to initiate the fastest growing skew-varicose mode ($K_y^2/K^2 = S^2 = 0.36$). Therefore when the rolls are sufficiently compressed by the finite-amplitude stage of the focus instability in order to trigger the skew-varicose instability, they are probably also in the unstable Eckhaus range. The Eckhaus instability has the additional advantage that it can remove only one roll. In a previous paper, Arter, Bernoff & Newell (1987) using a full numerical simulation of the fluid equations found that in a two-dimensional box, the

Eckhaus instability created or annihilated a roll at the boundary where the amplitude is already small. In the experiment in a circular cylinder, it is more likely that the extra roll is absorbed in the focus.

We now return to the case of almost circular patches surrounding sidewall foci in the moderate-Prandtl-number case investigated by Heutmaker & Gollub (1987). Here, because the onset of time dependence occurs at values well above threshold, the patches are forced by the boundaries to be almost but not quite circular. After a roll pair has been removed by the formation of dislocations and their disappearance, the relaxed pattern has a wavenumber distribution whose maximum is less than k_B. Therefore there is a tendency for the focus to produce new rolls because at this stage, as Greenside, Cross and Coughran (1988) observe in their numerical experiment, the mean drift flow has subsided and the balance to the third term in (1.1) is the first. However, once a new roll is produced by the focus, the pattern is again stressed, the mean flow is produced (we find in Appendix E that, in the model equation used to simulate the effect of an active amplitude order parameter near the focus, for moderate aspect ratios a significant part of the mean flow contribution is due to the non-slaved part of the amplitude) and the rolls near the centre of the container between the two roll patches are compressed so that their wavenumber again exceeds the value necessary to trigger the skew-varicose instability. For larger aspect ratios, the addition of the extra roll produces less distortion of the pattern and may not be enough to cause a sufficient distribution of the phase contours. In that case, we would suggest that the focus instability, this time with $m = 2$ so that the induced mean flow is quadripolar rather than dipolar, may serve to initiate the finite-amplitude state, although we have not yet carried out these calculations. (The reader should recall that the stability analysis is not changed by putting $D(r = 0, t) = 0$ so that the umbilicus stays on the sidewall and the outer portion of the roll patch is compressed.) The key point to make, then, is that the state to which the pattern relaxes after the disappearance of the dislocations, is either itself unstable or sufficiently close to an unstable state that it is strongly influenced by the unstable manifold of the latter.

In all these cases, the time dependence does not involve a disordered spatial state and would appear to be described by low-dimensional dynamics (Greenside *et al.* 1988 found a Hausdorff dimension of less than 3 for their model system) although no useful suggestion on how to coordinatize the phase space has been yet suggested. However, as the Rayleigh number is increased further, to the point where the centre of the wavenumber distribution k_B passes through the skew varicose boundary, we expect and predict a qualitative change in the dynamics. This occurs for $R = 7R_c$ at $P = 2.5$, about $R = 2R_c$ for $P = 0.71$ and almost immediately $R \gtrsim R_c$ when $P = 0.1$, although because of finite-aspect-ratio effects, these numbers should be taken as lower bounds. Once k_B crosses the skew-varicose boundary, every roll in the texture is unstable and we expect the nucleation of many defects and a resulting rapid decorrelation of the spatial pattern, in short a kind of macho rather than wimpy turbulence.

4. Conclusion

In this paper, we have derived the phase diffusion and mean drift equations for convection patterns, tested their predictions against known theoretical results, made some new predictions and compared them with experimental evidence. While this contribution represents a major step forward, it does not, alas, 'solve' the problem.

A theory that insists that the amplitude is everywhere slaved to the phase gradient does not provide the means for handling dislocations, disclinations and foci singularities and, as we have discovered, defects are an integral part of the pattern texture and play central roles in its dynamics. It is this challenge, the inclusion of a particle or singular component of the field, that we principally address in our concluding remarks.

We first remark that the initial boundary-value problem represented by (1.1) and (1.2) is ill-posed mathematically. The reason for this is that, for a large class of but not all initial conditions, the wavenumber k can evolve so as locally to exceed the values for the stability borders of the Busse balloon. At this point, (1.1) is like a nonlinear reverse heat equation and so requires a regularization term. Our previous work with model equations suggests that this regularization term can be approximated in certain cases by the biharmonic term $\epsilon^2\nabla^4\Theta$. However, we saw when we integrated the finite amplitude of the skew-varicose instability that this regularization was not quite sufficient close to the nucleation of a defect. As both the mathematics and the physics of the situation show, the instability is never arrested and, in the vicinity of the anticipated dislocation, the wavenumber becomes very large. At this stage is passes through the marginal stability curve and carries the validity of our theory right out the window with it! Indeed, at the marginal stability boundary, the amplitude, if still slaved (which we believe from evidence from simpler models is approximately true), is zero. For larger k, the amplitude must become a free parameter in the theory, namely an active rather than passive order parameter.

Some may argue that this is not enough and that as soon as the field approaches the zero state one must include as additional order parameters the full set of modes associated with the centre manifold of the zero state at the marginal stability boundary. This would include, for example, a combination of rolls with all directions. However, we shall suggest that this is not necessary, that because the wavenumber passes through the marginal stability boundary only locally, the outer solution near these defects effects a bias in the choice of roll direction at the defect so that in general it is sufficient to consider only the amplitude of that wavevector which is dominant in the neighbourhood of the singularity as the extra active order parameter. (In special cases, where one might be near parameter values at which different planforms are equally likely, then this would not be true and the defect case may serve as the nucleation point of the new phase. Coullet (private communication) argues that grain boundaries (which are line singularities) do indeed play such a role.

Another instance in which we found the phase diffusion – mean drift description inadequate was near regions of large curvature of rolls such as at the centre of foci singularities. As we have seen in §3.2 and Appendix E, even the stability problem of circular rolls is extremely delicate owing to the behaviour of the eigenmodes near the focus. We could prove stability for $s < 1$ with (3.34). In order to treat the unstable region in parameter space, it was necessary to know exactly what the phase perturbation does near $r = 0$ and to accomplish this we had to match the solution to the behaviour of an active amplitude parameter there. Even the case of stationary circular patterns is non-trivial and, as pointed out in the works of Brown & Stewartson (1978) and Pomeau, Zaleski & Manneville (1985), requires the consideration of the behaviour of the amplitude at the focus.

How do we remedy this situation? In Appendix E, we indicate what the amplitude regularization is near foci. Here we discuss dislocations. We gain some insight by thinking back to the case of small-amplitude convection, valid near $R = R_c$ and correctly described by the Newell–Whitehead–Segel equation for the complex

amplitude $w = A\,e^{i\theta}$ which includes both amplitude A and phase θ. It is well known that the two-dimensional version of this equation in a non-rotational invariant situation (as is the case here because of the influence of the outer solution),

$$\frac{\partial w}{\partial t} - \nabla^2 w = (R - R_c)\,w - w^2 w^*, \tag{4.1}$$

also known as the Ginzburg–Landau equation, has vortex solutions for which the complex amplitude w is smooth but which, when written in polar form $w = A\,e^{i\theta}$, involve a 2π phase discontinuity along contours surrounding the vortex. What we have been able to do in model equation situations (e.g. for the Swift–Hohenberg equation and for (4.1); the full Oberbeck–Boussinesq equations are too complicated) is to write down what is the amplitude regularization of the phase diffusion equation. Then we introduce the new complex amplitude $w = A \exp i\Theta/\epsilon$ in these coordinates, the equations have removable singularities. The problem of matching involves an intermediate regime which connects the inner solutions with the outer phase diffusion approximation in which the amplitude is slaved. We emphasize that in this intermediate region, the corrections to the outer phase diffusion – amplitude (in the outer region, to leading order the amplitude is determined by an algebraic equation with corrections involving amplitude derivations) – mean drift equation, involving the amplitude terms are the largest. In these model situations, we are close to having a general description of patterns which combine the advantages of the Cross–Newell formalism, which has rotational invariance, and the Newell–Whitehead–Segel equations, which have an amplitude component but no rotational invariance. We shall report on these ideas shortly.

Our programme for the next stage of this research is:

1. Use the theory just described to describe the nucleation, motion and annihilation of dislocation pairs for (4.1) beginning with initial conditions $w = (R - R_c - K^2)^{\frac{1}{2}} \exp iKx$, where the wavenumber K lies outside the Eckhaus stability boundary, and compare the results with the experiments of Lowe & Gollub (1986) and theory of dislocation velocities of Bodenschatz, Pesch and Kramer (1989).

2. Derive the partial differential equation for the amplitude for the fluid equations and show that, in the infinite-aspect-ratio limit $\epsilon \to 0$, the presence of the amplitude correction is crucial but its exact form is not, much like the case of the drag on bodies in fluids at the infinite-Reynolds-number limit (D'Alembert paradox). We would then like to be able to use the amplitude terms to design weak solutions to the phase diffusion–mean drift equations which tell us how to apply conditions to these variables so as to be able to continue the solutions through the formation of singularities. This problem has much in common with, but may be simpler than, the vortex reconnection problem in high-Reynolds-number flows.

3. Carry out the linear stability analysis and calculate the finite-amplitude state for the focus instability.

In short, the programme we have outlined seeks to construct the first macroscopic field-particle theory from an underlying set of governing equations at the microscopic level. A tall order? Perhaps. But then again, there is hardly a more suitable context than convection patterns in which to make the attempt.

The authors are grateful for support under Air Force grant number AFOSR4962086C0130 and NSF grant number DMS 8703397. One of us (A.C.N.) is also grateful for a Humboldt Fellowship and the hospitality he received at the

University of Bayreuth. We also want to thank Fritz Busse, Mike Cross, Rob Indik, David Levermore, Yves Pomeau and Pierre-Louis Sulem for useful discussions and the referees for pointing out many references we had overlooked.

Appendix A. The vorticity formulation

We now give an alternative derivation of the phase diffusion and mean drift equations using the vorticity formulation. It will provide some insights and also serves as an independent check of the coefficients in the phase diffusion equation. The advantage of the vorticity formulation is that it eliminates the pressure term from (2.3) but we have seen how a slowly varying pressure field is built up by the mean drift fields driven by horizontal Reynolds stresses. It is important, therefore, to see how this slowly varying pressure term is reintroduced.

We now take as our governing equations (2.6), (2.4) and (2.5) and write the equations for the perturbed vorticity and temperature fields. In the local across- and along-the-roll coordinates, these equations at first order in the perturbation fields decompose into two uncoupled systems. The equations for perturbation temperture T_1, along the roll perturbation vorticity $\eta_1 = (\partial\tilde{u}_1/\partial z) - k(\partial/\partial\theta)\, w_1$ and the continuity equation gives us three equations for $\tilde{u}_1$, w_1 and T_1:

$$\begin{aligned}
&\left\{\left(k^2\frac{\partial^2}{\partial\theta^2}+\frac{\partial^2}{\partial z^2}\right)\frac{\partial}{\partial z}-\sigma k\frac{\partial}{\partial\theta}\tilde{\eta}_0-\sigma w_0\frac{\partial^2}{\partial z^2}-\sigma\tilde{u}_0 k\frac{\partial^2}{\partial\theta\,\partial z}\right\}\tilde{u}_1 \\
&\quad+\left\{\sigma\tilde{u}_0 k^2\frac{\partial^2}{\partial\theta^2}+\sigma w_0 k\frac{\partial^2}{\partial\theta\,\partial z}+\sigma\frac{\partial\tilde{\eta}_0}{\partial z}-\left(k^2\frac{\partial^2}{\partial\theta^2}+\frac{\partial^2}{\partial z^2}\right)k\frac{\partial}{\partial\theta}\right\}w_1+k\frac{\partial T}{\partial\theta} \\
&=\sigma\Theta_T\frac{\partial\tilde{\eta}_0}{\partial\theta}+\sigma\tilde{u}_0(\hat{\boldsymbol{k}}\cdot\nabla)\,\tilde{\eta}_0-\sigma\tilde{u}_0\,\tilde{\eta}_0\,\nabla\cdot\hat{\boldsymbol{k}}-D\frac{\partial\tilde{\eta}_0}{\partial\theta}+(\hat{\boldsymbol{k}}\cdot\nabla)\,T_0 \\
&\quad+\left(k^2\frac{\partial^2}{\partial\theta^2}+\frac{\partial^2}{\partial z^2}\right)(\hat{\boldsymbol{k}}\cdot\nabla)\,w_0-\sigma k\tilde{u}_0(\hat{\boldsymbol{k}}\cdot\nabla)\frac{\partial w_0}{\partial\theta}-\sigma w_0(\hat{\boldsymbol{k}}\cdot\nabla)\frac{\partial w_0}{\partial z}. \qquad \text{(A 1)}
\end{aligned}$$

$$\begin{aligned}
&\left(k^2\frac{\partial^2}{\partial\theta^2}+\frac{\partial^2}{\partial z^2}-\tilde{u}_0 k\frac{\partial}{\partial\theta}-w_0\frac{\partial}{\partial z}\right)T_1-k\frac{\partial T_0}{\partial\theta}\tilde{u}_1+\left(R-\frac{\partial T_0}{\partial z}\right)w_1 \\
&\qquad=\Theta_T\frac{\partial T_0}{u\theta}-D\frac{\partial T_0}{u\theta}+\tilde{u}_0(\hat{\boldsymbol{k}}\cdot\nabla)\,T_0, \qquad \text{(A 2)}
\end{aligned}$$

$$k\frac{\partial}{\partial\theta}\tilde{u}_1+\frac{\partial w_1}{\partial z}=-\nabla\cdot\hat{\boldsymbol{k}}\tilde{u}_0. \qquad \text{(A 3)}$$

The two remaining equations for across-the-roll and vertical vorticities do not, on the surface, involve $\tilde{u}_1$, w_1, T_1 but only $\tilde{v}_1$. They are

$$-\frac{\partial}{\partial z}\mathrm{L}\tilde{v}_1=R_1, \qquad \text{(A 4)}$$

$$\frac{\partial}{\partial\theta}\mathrm{L}\tilde{v}_1=R_2, \qquad \text{(A 5)}$$

where

$$\left.\begin{aligned}
\mathrm{L} &= \tilde{u}_0 k\frac{\partial}{\partial\theta}+w_0\frac{\partial}{\partial z}-\sigma^{-1}\left(k^2\frac{\partial^2}{\partial\theta^2}+\frac{\partial^2}{\partial z^2}\right)\\
R_1 &= \frac{1}{2k^2}\frac{\partial\tilde{u}_0^2}{\partial z}(\hat{\boldsymbol{k}}\times\boldsymbol{\nabla})\,k^2-\hat{\boldsymbol{k}}\times\boldsymbol{\nabla}\left(k\frac{\partial}{\partial\theta}(\tilde{u}_0 w_0)+\frac{\partial w_0^2}{\partial z}\right)+\sigma^{-1}\left\{-\left(\frac{\partial^2}{\partial\theta\,\partial z}\frac{\tilde{u}_0}{k}-\frac{\partial^2}{\partial\theta^2}\right)(\hat{\boldsymbol{k}}\times\boldsymbol{\nabla})\,k^2\right.\\
&\quad\left.+(\hat{\boldsymbol{k}}\times\boldsymbol{\nabla})\,T_0+\left(k^2\frac{\partial^2}{\partial\theta^2}+\frac{\partial^2}{\partial z^2}\right)(\hat{\boldsymbol{k}}\times\boldsymbol{\nabla})\,w_0\right\}\\
R_2 &= (\hat{\boldsymbol{k}}\times\boldsymbol{\nabla})\frac{\partial}{\partial z}w_0\frac{\tilde{u}}{k}+(\hat{\boldsymbol{k}}\times\boldsymbol{\nabla})\frac{\partial}{\partial\theta}\tilde{u}_0^2-\frac{1}{2k^2}\frac{\partial}{\partial\theta}\tilde{u}_0^2(\hat{\boldsymbol{k}}\times\boldsymbol{\nabla})\,k^2-\sigma^{-1}\left(k^2\frac{\partial^2}{\partial\theta^2}+\frac{\partial^2}{\partial z^2}\right)(\hat{\boldsymbol{k}}\times\boldsymbol{\nabla})\frac{\tilde{u}_0}{k}.
\end{aligned}\right\} \tag{A 6}$$

The solvability of (A 1) (A 2) (A 3) for $\tilde{u}_1$, w_1, T_1 will give the phase diffusion equation. However, before we apply the Fredholm condition, we must first consider the compatibility of (A 4) and (A 5), two equations for one unknown. We must have

$$\frac{\partial R_1}{\partial\theta}+\frac{\partial R_2}{\partial z}=0 \tag{A 7}$$

which can be easily verified. Integrating (A 5), we find

$$\mathrm{L}\tilde{v}_1 = P_2+F(z), \tag{A 8}$$

where $R_2=\partial P_2/\partial\theta$ and $F(z)$ is an arbitrary function of z. The compatibility condition (A 7) shows that F is independent of θ and z and, therefore, up to dependence on the slow variables, is a constant F_0. But it cannot be determined at this order. In fact it is found at the next order, order ϵ^2. This extra constant F_0 will play the role of $\boldsymbol{\nabla}P_s$, a constant pressure gradient, and will drive a Poiseuille-like mean flow $\tilde{v}_1$ (the solution of $\mathrm{L}\tilde{v}_1=F_0$), nonlinearly coupled to the convective structure.

We find an equation for F_0 by looking at the vorticity equation (2.6) at order ϵ^2 and averaging over θ and z. The components parallel and perpendicular to the rolls give no non-trivial contributions but the vertical vorticity equation gives

$$\left\langle\frac{\partial^2\zeta}{\partial z^2}\right\rangle=\sigma\langle\boldsymbol{\nabla}\cdot(\boldsymbol{\omega}_1\cdot\boldsymbol{u}_0+\boldsymbol{\omega}_0\cdot\boldsymbol{u}_1-\boldsymbol{u}_0\cdot\boldsymbol{\omega}_1-\boldsymbol{u}_1\cdot\boldsymbol{\omega}_0)\rangle \tag{A 9}$$

or

$$\left\langle\frac{\partial^2}{\partial z^2}\left(\partial_x v_1-\partial_y u_1\right)\right\rangle=\langle\boldsymbol{\nabla}\times\boldsymbol{\nabla}\cdot(u_0\,u_0)\rangle. \tag{A 10}$$

This gives as an equation for F_0 (which now is a slowly varying function of X, Y and T). However, we are not yet out of the woods because $\tilde{v}_1$ and $\tilde{u}_1$ which were, up to now, uncoupled, are constrained to satisfy continuity which in these variables takes the form:

$$\boldsymbol{\nabla}\cdot\langle\hat{\boldsymbol{k}}\tilde{u}_1\rangle-\hat{\boldsymbol{z}}\cdot\boldsymbol{\nabla}\times\langle\hat{\boldsymbol{k}}\tilde{v}_1\rangle=0. \tag{A 11}$$

Therefore, if $\tilde{u}_1$ were to be solved from (A 1)–(A 3) by first applying the Fredholm alternative for that system of equations and then determining $\tilde{u}_1$ from what remains, the three equations (A 7), (A 10) and (A 11) give us three conditions for two unknowns, $\tilde{v}_1$ and F_0.

The only way to overcome this overdeterminacy is to constrain $\tilde{u}_1$ as follows. Decompose the total velocity field $\tilde{\boldsymbol{u}}_1 = (\tilde{u}_1, \tilde{v}_1)$ into a mean and fluctuating component

$$\tilde{\boldsymbol{u}}_1 = \boldsymbol{U}_1 + \tilde{\boldsymbol{u}}_1', \tag{A 12}$$

where $\tilde{\boldsymbol{u}}_1'$ averaged over θ is zero. Instead of calculating $\tilde{u}_1$ from (A 1) (A 3) on a complete basis which contains both $\{g_n(z)\,\mathrm{e}^{\mathrm{i}m\theta}\}_{m=0,\,n=1}^{M,\,N}$ and a θ-independent mean flow $g_0(z)$ with non-zero vertical average, we make the decomposition (A 12) and calculate $\tilde{u}_1'$, $\tilde{v}_1'$ in the constrained original basis used for $\tilde{u}_0$, $\tilde{v}_0$ using no mean flow. The equation for u_1' now will have terms on the right-hand side containing U_1. The resulting solvability condition, the phase diffusion equation, will contain an unknown function $\tilde{\boldsymbol{u}}(z, X, Y, T)$, but this together with $\tilde{\boldsymbol{v}}(z, X, Y, T)$ will be determined by the pair of equations (A 10) and (A 11). We shall obtain exactly as before the mean drift equation (1.2).

The phase diffusion equation reads:

$$\begin{aligned}
&\boldsymbol{\Theta}_T\left\{\sigma\left(\frac{\partial}{\partial\theta}\tilde{\eta}_0, \tilde{u}^{\mathrm{A}}\right)+\left(\frac{\partial T_0}{\partial\theta}, w^{\mathrm{A}}\right)\right\}\\
&\qquad+\boldsymbol{k}\cdot\boldsymbol{V}\left\{\sigma\left(\frac{\partial}{\partial\theta}\tilde{\eta}_0 f(z), u^{\mathrm{A}}\right)+\frac{\sigma}{k}(w_0 f''(z), \tilde{u}^{\mathrm{A}})+\left(\frac{\partial}{\partial\theta}T_0 f(z), w^{\mathrm{A}}\right)\right\}\\
&\qquad-\left(D\frac{\partial}{\partial\theta}\tilde{\eta}_0, u^{\mathrm{A}}\right)-\left(D\frac{\partial T_0}{\partial\theta}, w^{\mathrm{A}}\right)+((\hat{\boldsymbol{k}}\cdot\boldsymbol{\nabla})\,T_0, \tilde{u}^{\mathrm{A}})\\
&\qquad+\left(\left(k^2\frac{\partial^2}{\partial\theta^2}+\frac{\partial^2}{\partial z^2}\right)\hat{\boldsymbol{k}}\cdot\boldsymbol{\nabla}k\,w_0, \tilde{u}^{\mathrm{A}}\right)\\
&\qquad+(\tilde{u}_0(\hat{\boldsymbol{k}}\cdot\boldsymbol{\nabla})\,T_0, w^{\mathrm{A}})+(\boldsymbol{\nabla}(k\tilde{u}_0), T^{\mathrm{A}})\\
&\qquad+\sigma\left\{(\tilde{u}_0(\hat{\boldsymbol{k}}\cdot\boldsymbol{\nabla})\,\tilde{\eta}_0, \tilde{u}^{\mathrm{A}})-(\tilde{u}_0\tilde{\eta}_0\,\boldsymbol{\nabla}\cdot\hat{\boldsymbol{k}}, \tilde{u}^{\mathrm{A}})\right.\\
&\qquad\left.-\left(\tilde{u}_0 k(\hat{\boldsymbol{k}}\cdot\boldsymbol{\nabla})\frac{\partial w_0}{\partial\theta}, \tilde{u}^{\mathrm{A}}\right)-\left(w_0(\hat{\boldsymbol{k}}\cdot\boldsymbol{\nabla})\frac{\partial w_0}{\partial z}, \tilde{u}^{\mathrm{A}}\right)\right\}=0.
\end{aligned}\tag{A 13}$$

In (A 13), $\tilde{u}^{\mathrm{A}}$, w^{A} and T^{A} are the solutions to the adjoint equations for (A 1)–(A 3). They are different from the previous adjoint solutions. Even though the coefficients in the equations for the phase diffusion and mean drift equation are derived from a completely different starting point, a numerical check of the coefficients show they agree to better than 1 %.

Appendix B. Compatibility of two approaches

In this Appendix we shall briefly sketch how we can deduce the same diffusion equation as (2.54) when working with the full basis including the extra mode $g_0(z)$ which has a non-zero flux associated with it. A detailed and quantitative check of the equivalence has to be done numerically (and was done only for the derivation of the mean drift equation itself) since the coefficients appearing in the two versions of the phase equation involve adjoint vectors calculated numerically on different bases. The derivation proceeds in the same way as in §2 except that in (2.34) terms on the right-hand side containing U_1 are absent. They are included in the left-hand side as coefficients of $g_0(z)$. The term ∇p_{s}, which previously did not project on the restricted

basis of zero flux, will now be present in the phase diffusion equation as $(\hat{\boldsymbol{k}} \cdot \boldsymbol{\nabla} p_s, \tilde{u}^A)$ which replaces terms containing U_1. Let us then calculate $\hat{\boldsymbol{k}} \boldsymbol{\nabla} p_s$ as a function of U_1. The equations for the total horizontal velocity $\tilde{u}_1$, w_1, T_1, p_1 are

$$(k^2 \partial_0^2 + \partial_z^2)\tilde{u}_1 - 2\sigma k \partial_0(\tilde{u}_0 \tilde{u}_1) - \sigma \frac{\partial}{\partial z}(\tilde{u}_0 w_1 + \tilde{u}_1 w_0) - k \frac{\partial p_1}{\partial_0} = \sigma \Theta_T \frac{\partial \tilde{u}_0}{\partial \theta}$$

$$- D \frac{\partial \tilde{u}_0}{\partial \theta} + \sigma \boldsymbol{\nabla} \cdot (\hat{\boldsymbol{k}} \tilde{u}_0^2) + (\hat{\boldsymbol{k}} \cdot \boldsymbol{\nabla})(p_0 + p_s), \quad \text{(B 1)}$$

$$(k^2 \partial_0^2 + \partial_z^2) w_1 - \sigma k \partial_\theta(\tilde{u}_0 w_1 + \tilde{u}_1 w_0) - 2\sigma \frac{\partial}{\partial z}(w_0 w_1) - \frac{\partial p_1}{\partial z} + T_1$$

$$= \sigma \Theta_T \frac{\partial w_0}{\partial \theta} - D \frac{\partial w_0}{\partial \theta} + \sigma \boldsymbol{\nabla} \cdot (\hat{\boldsymbol{k}} \tilde{u}_0 w_0), \quad \text{(B 2)}$$

$$(k^2 \partial_0^2 + \partial_z^2) T_1 - k \partial_\theta(\tilde{u}_0 T_1 + \tilde{u}_1 T_0) - \frac{\partial}{\partial z}(w_0 T_1 + w_1 T_0) + R w_1$$

$$= \Theta_T \frac{\partial T_0}{\partial \theta} - D \frac{\partial T_0}{\partial \theta} + \boldsymbol{\nabla} \cdot (\hat{\boldsymbol{k}} \tilde{u}_0 T_0), \quad \text{(B 3)}$$

$$k \frac{\partial \tilde{u}_1}{\partial \theta} + \frac{\partial w_1}{\partial z} = - \boldsymbol{\nabla} \cdot (\hat{\boldsymbol{k}} \tilde{u}_0). \quad \text{(B 4)}$$

When solving this system on the full basis, we have for $\tilde{u}_1$:

$$\tilde{u}_1 = a_0 \Theta_T + a_{11} \Theta_{XX} + 2a_{12} \Theta_{XY} + a_{22} \Theta_{YY} + a \hat{\boldsymbol{k}} \cdot \boldsymbol{\nabla} p_s. \quad \text{(B 5)}$$

It is convenient to introduce a new independent variable in the system, namely ψ, the stream function of the mean horizontal velocity. We write

$$\langle \tilde{u} \rangle = \hat{\boldsymbol{k}} \times \boldsymbol{\nabla} \psi \cdot \boldsymbol{z}. \quad \text{(B 6)}$$

p_s can be expressed in terms of ψ by integrating (B 5) with respect to θ and z, whereupon we find

$$\hat{\boldsymbol{k}} \cdot \boldsymbol{\nabla} p_s = \frac{1}{\langle a \rangle} \hat{\boldsymbol{k}} \times \boldsymbol{\nabla} \psi \cdot \boldsymbol{z} - \frac{\langle a_0 \rangle}{\langle a \rangle} \Theta_T - \frac{\langle a_{11} \rangle}{\langle a \rangle} \Theta_{XX} - 2 \frac{\langle a_{12} \rangle}{\langle a \rangle} \Theta_{XY} - \frac{\langle a_{22} \rangle}{\langle a \rangle} \Theta_{YY}. \quad \text{(B 7)}$$

We see clearly that one of the combinations of $(\hat{\boldsymbol{k}} \cdot \boldsymbol{\nabla} p_s, \tilde{u}^A)$ will be an advection term of the form $\boldsymbol{k} \cdot \boldsymbol{V}$ where $\boldsymbol{V} = \boldsymbol{\nabla} \times \psi \boldsymbol{z}$. The equation for ψ is obtained in the same way as in §2 by replacing p_s in terms of ψ in (B 5) and using this expression for $\tilde{u}_1$ in (2.29) and (2.30) after which we take the curl to eliminate $\boldsymbol{\nabla} p_s$. The equations we obtain have exactly the same form as (2.49) and (2.62).

Appendix C. Further comments on the numerical calculations

The complete calculation of the coefficients for the phase diffusion (1.1) and mean drift (1.2) equations has been carried out with both the momentum formulation (referred to as I) and the vorticity formulation (referred to as II). We shall present here the detailed steps for both cases. The first step involves the computation of the steady roll solution for all values of the wavenumber lying inside the marginal stability curve. For each Rayleigh and Prandtl number, a set of values of the wavenumber k is chosen, spanning the whole interval located inside of the marginal

stability curve. The basis chosen for the velocity and temperature fields is the same in I and II and given explicitly in §2. In formulation I we also have to choose a Galerkin basis for the pressure. A good choice is $\{e^{im\theta}\cos n\pi(z+\frac{1}{2})\}$, the same as one would choose for the zero-stress boundary condition case (called the free–free case), since in both cases no conditions on the horizontal boundaries are given on the pressure. Note that p is only determined up to a constant p_s. The equations of formulation I at order ϵ^0 read:

$$(k^2\partial_\theta^2+\partial_z^2)\,\tilde{u}_0-\sigma(\tilde{u}_0\,k\,\partial_\theta\,\tilde{u}_0+w_0\,\partial_z\,\tilde{u}_0)-k\,\partial_\theta\,p_0=0, \tag{C 1}$$

$$(k^2\,\partial_\theta^2+\partial_z^2)\,w_0-\sigma(\tilde{u}_0\,k\,\partial_\theta\,\tilde{w}_0+w_0\,\partial_z\,\tilde{w}_0)-\partial_z\,p_0=0, \tag{C 2}$$

$$(k^2\,\partial_\theta^2+\partial_z^2)\,T_0-\sigma(\tilde{u}_0\,k\,\partial_\theta\,T_0+w_0\,\partial_z\,T_0)+Rw_0=0, \tag{C 3}$$

$$k\,\partial_\theta\,u_0+\partial_z\,w_0=0. \tag{C 4}$$

Having chosen the bases in which we wish to expand the fields, the next step is to project these equations onto some basis functions in order to obtain the right number of algebraic questions for the coefficients in the former expansions. Since the fields themselves are decomposed in different bases, *a priori* no single projection appears more natural than any other. As a guide, consider what we do in the free–free case for I in which case the fields $\tilde{u}_0$ and w_0 are decomposed on to the bases $\{e^{im\theta}h_n(z)\}$ and $\{e^{im\theta}f_n(z)\}$ respectively. In this case, the algebraic questions can be derived directly by identification, which is equivalent to projecting (C 1) onto the basis $\{e^{im\theta}h_n(z)\}$ and (C 2) and (C 3) onto the basis $\{e^{im\theta}f_n(z)\}$. The continuity equation (C 4) is eliminated by using the relation

$$w_{mn}=k_m\,U_{mn}.$$

Returning to the rigid–rigid boundary conditions, this suggests that it is reasonable to project (C 1) onto the basis $\{e^{im\theta}g_n'(z)\}$, (C 2) onto the basis $\{e^{im\theta}g_n(z)\}$ and (C 3) onto the basis $\{e^{im\theta}f_n(z)\}$. This choice of projection for (C 2) turns out to give a correct and rapid convergence to the solution. Turning now to formulation II, we find that the equation for the vorticity along the rolls is best projected onto the basis $\{e^{im\theta}g_n(z)\}$ and the equation for the temperature onto the basis $\{e^{im\theta}f_n(z)\}$. In each case, we obtain a set of algebraic equations that we solve using a Newton's method. In solving this system, it is vital to find a good starting approximation. To get this approximation, we first solve for the coefficients interatively in terms of the amplitude A of the lowest-order mode in the horizontal velocity field u at values of a wavenumber $k_{\max}$ near the right-hand edge of the marginal stability curve where the amplitudes are very small. Each field is written in its appropriate basis with the coefficient of the nth component of the basis vector used to describe the vertical structure proportional to A^n, e.g. $u=\sum u_{mn}\,e^{im\theta}g_n'(z)\,A^n$. It is sufficient to use the first two terms, $-2\leqslant m\leqslant 2$, $1\leqslant n\leqslant 2$. Substituting this expansion into the equations, we get linear equations for u_{mn} and T_{mn} and a nonlinear dispersion relation determining A in terms of the chosen k and the Rayleigh and Prandtl numbers. Having obtained a good approximation when A is small, we can use this to apply the Newton method. As we move the wavenumbers to lower values of k well within the marginal stability curve, we can use as the first guess the values of the solutions computed at the previous k. We want to stress that the step size in k is varied as the 'amplitude' (see figure 9*e* which draws $\langle\tilde{u}_0^2\rangle/k^2$ as a function of k) of the solutions and its derivative with respect to k becomes very large. Since we also need to be able to differentiate all the calculated functions with respect to k, we interpolate all coefficients of the fields using cubic spline polynomials. We find that the

convergence for the System I requires more modes in the vertical direction than for System II. One could argue, therefore, that the vorticity formulation is slightly better adapted for numerical purposes. Convergence is tested by checking the Nusselt number (the non-dimensional heat flow) against the existing results of Clever & Busse (1974, 1979).

The second major step in the computation involves determining, for each k, the null eigenvector for the adjoint linear system of equations (2.39)–(2.42a) or (A 1)–(A 3). Here two methods are possible. The first one consists in directly solving the adjoint linear system (2.44)–(2.48), which gives the components of $\tilde{u}^{\mathrm{A}}$, w^{A}, T^{A}, p^{A} onto their respective bases:

$$\{\mathrm{e}^{\mathrm{i}m\theta} g_n'(z)\}, \quad \{\mathrm{e}^{\mathrm{i}m\theta} g_n(z)\}, \quad \{\mathrm{e}^{\mathrm{i}m\theta} f_n(z)\}, \quad \{\mathrm{e}^{\mathrm{i}m\theta} h_n(z)\}.$$

The second method, which we adopt, is to build the matrix equivalent of the linear systems (2.39)–(2.42a) and (A 1)–(A 3) by projecting the equations on the same basis functions as we used for the nonlinear system. We then obtain the algebraic equations (2.82), (2.83). One advantage of this formulation is that it is possible to check the numerics by comparing the null eigenvector of the matrix $\boldsymbol{A}_1$ with $(\partial/\partial\theta)(\tilde{u}_0, w_0, T_0, p_0)$. To find agreement to within 10^{-9}, the precision required in the calculation of the nonlinear system. The solvability condition is computed directly on this algebraic system by taking the transpose of $\boldsymbol{A}_1$ and calculating its null eigenvector. As discussed already, we use a singular-value decomposition method which is found to be much more reliable and robust than the direct calculation of the eigenvectors. The application of the solvability condition on the algebraic system means that a term like $(\boldsymbol{k}\cdot\boldsymbol{\nabla} p_0, \tilde{u}^{\mathrm{A}})$ in (2.49) is evaluated by expressing the X-derivative $\partial/\partial X$ as $\boldsymbol{\Theta}_{XX}(k_1/k)(\partial/\partial k) + \boldsymbol{\Theta}_{XY}(k_2/k)(\partial/\partial k)$, namely in terms of products of second derivatives in $\boldsymbol{\Theta}$ with derivatives with respect to k. Finally we mention how we calculate the functions $B(k)$ from $\tau(k)$, $\gamma_{11}(k)$, $\gamma_{12}(k)$, $\gamma_{22}(k)$. Since we evaluate all coefficients with $k_1 = k$, $k_2 = 0$, we can find for $B(k)$ by solving (using a Runge–Kutta method) the equation

$$\frac{\mathrm{d}B}{\mathrm{d}k} = \frac{B}{k}\left(\frac{\gamma_{11}}{\gamma_{22}} - 1\right)$$

with $\mathrm{d}B/\mathrm{d}k = \gamma_{11}/k$ at $k = k_B$, the zero of $\gamma_{22}(k)$. The functions B_α and B_β are calculated in a similar way.

Appendix D. Table of data

R	$k_i - k_n$	k_L	k_R	k_B	c	s	e	b
				$P = 70$				
2000	2.9–4	3.08 (Z)	3.74 (E)	—	—	—	—	—
3000	2.7–4.8	2.93	4.42 (E)	3	0.9999	4.44×10^{-2}	-9.8×10^{-2}	2.44×10^{-2}
4000	2.5–5.1	2.74 (Z)	4.82 (E)	2.85	0.9998	7.26×10^{-2}	-0.21	4.47×10^{-2}
5000	2.5–2.7	2.56	5.12 (E)	2.71	0.9998	—	9.8×10^{-2}	6.48×10^{-2}
6000	2.2–5.6	2.417 (Z)	5.37	2.589	0.9998	0.117	-0.397	8.34×10^{-2}
8000	2–6	2.19 (Z)	5.784 (E)	2.386	0.9997	0.147	0.529	0.116
				$P = 2.5$				
1800	2.8–3.6	2.96 (Z)	3.45 (S)	3.107	0.998	0.09	0.6×10^{-2}	0.5
2000	2.4–3.7	2.7 (Z)	3.7 (S)	3.08	0.995	0.297	1.5×10^{-2}	0.16
2500	2.2–4.1	2.26 (Z)	3.97 (S)	3.016	0.988	0.78	1.89×10^{-2}	0.45
2600	—	—	—	3.002	0.986	0.874	1.84×10^{-2}	0.51
2620	—	—	—	2.9987	0.986	0.893	1.81×10^{-2}	0.52
2640	—	—	—	—	0.985	0.911	1.77×10^{-2}	0.53
2660	—	—	—	—	0.985	0.929	1.75×10^{-2}	0.54
2680	—	—	—	2.989	0.985	0.948	1.72×10^{-2}	0.55
2700	—	—	—	—	0.985	0.966	1.68×10^{-2}	0.57
2720	—	—	—	—	0.985	0.984	1.65×10^{-2}	0.58
2760	—	—	—	—	0.984	1.02	1.58×10^{-2}	0.60
2800	—	—	—	2.97	0.983	1.056	1.52×10^{-2}	0.63
2850	—	—	—	2.964	0.982	1.1	1.42×10^{-2}	0.66
2900	—	—	—	2.955	0.982	1.14	1.32×10^{-2}	0.69
3000	1.8–4.1	2 (Z)	4 (S)	2.94	0.9811	1.23	9.26×10^{-2}	0.74
4000	1.6–3.7	1.7 (E)	3.61 (S)	2.786	0.969	1.969	-4.7×10^{-2}	1.32
5000	1.4–3.4	1.47 (E)	3.2 (S)	2.656	0.959	2.57	-6.75×10^{-2}	1.86
6000	1.4–3.2	1.50 (E)	2.92 (S)	2.55	0.95	3.09	-7.35×10^{-2}	2.36
7000	1.5–2.9	1.35	2.73	2.46	0.94	3.53	-7.19×10^{-2}	2.82
9000	1.2–2.6	1.22	2.48	2.33	0.927	4.27	-9.05×10^{-2}	3.67
10000	2.1–2.5	—	2.39 (S)	2.28	0.92	4.61	-8.9×10^{-2}	4.07
11000	2.1–2.5	—	2.299 (S)	2.24	0.914	4.94	-7.8×10^{-2}	4.45
12000	2.1–2.4	—	2.22	2.20	0.908	5.27	-7.09×10^{-2}	4.82

TABLE 2. For caption see next page.

R	$k_l - k_n$	k_L	k_R	k_B	c	s	e	b
				$P = 0.71$				
1800	2.7–3.5	2.8 (Z)	3.37 (S)	3.117	0.983	0.46	0.09	0.222
1850	—	—	—	—	0.9737	0.715	0.1426	0.3405
1860	—	—	—	—	0.972	0.764	0.150	0.364
1870	—	—	—	—	0.970	0.8122	0.1597	0.388
1880	—	—	—	—	0.9687	0.860	0.168	0.411
1890	—	—	—	3.119	0.967	0.908	0.1766	0.434
1900	—	—	—	—	0.965	0.956	0.186	0.458
1910	—	—	—	3.12	0.964	1.003	0.194	0.48
1920	—	—	—	3.12	0.962	1.05	0.202	0.504
1930	—	—	—	—	0.96	1.095	0.209	0.527
1940	—	—	—	3.1708	0.959	1.143	0.218	0.55
1950	—	—	—	—	0.957	1.189	0.226	0.573
1960	—	—	—	—	0.956	1.236	0.234	0.596
1970	—	—	—	3.121	0.954	1.28	0.241	0.619
1980	—	—	—	—	0.952	1.33	0.25	0.641
1990	—	—	—	—	0.951	1.373	0.258	0.664
2000	2.3–4.1	2.54 (E)	3.4 (S)	3.122	0.95	1.42	0.265	0.67
2500	2.0–3.5	2.38 (E)	3.17 (S)	3.128	0.896	3.35	0.4116	1.745
3000	1.7–3.3	197 (E)	2.93 (S)	3.124	0.85	5.51	0.998	2.706
4000	1.4–3.2	1.688 (E)	2.62 (S)	3.109	0.8	7.67	0.407	4.403
				$P = 0.1$				
1750	2.8–3.3	—	—	—				
1800	2.6–3.5	2.82 (E)	3.139 (S)	3.521				
1900	—	2.706	3.125 (S)	3.76				
2000	2.5–4.1	2.63 (E)	3.09 (S)	—				
2100	2.4–4.3	2.548	3.048	4.07				

TABLE 2 A list of the values of the left and right boundaries of the Busse balloon k_L and k_R respectively, the zero k_B of the perpendicular diffusion coefficient, and the values of c, s, e, b evaluated at k_B for a range of Rayleigh numbers at four values of Prandtl number. In the first column we list the value of the Rayleigh number. In the second, we give the range of wavenumbers over which the functions, graphed in figures 9 and 10, were tabulated. We omit these data as well as the data for the left and right ends of the Busse balloon for $P = 2.5$ and $P = 0.71$ when we interpolate between $R = 2500$ and 3000 and 1850 and 1990 respectively in which the intervals the parameter s, increases through unity. (Z) denotes zigzag instability, (E) Eckhaus, and (S) skew-varicose.

Appendix E. The focus instability

In this Appendix, we study the stability of target patterns using a coupled phase–amplitude–mean drift formulation. As mentioned in §3.2, it is absolutely necessary to regularize the phase diffusion – mean drift equations close to the centre of the patch where the strong curvature of the rolls invalidates the phase description. Here we calculate the shape of the unstable mode of the focus instability and study the influence of the aspect ratio $\Gamma = \epsilon^{-1}$ on the stability criterion. In contrast to the case of a dislocation, the amplitude does not vanish at the centre of a focus. In fact, it is larger there (see Brown & Stewartson 1978; Pomeau *et al.* 1985). One possibility for regularizations is to add the next-order term in the phase equation, which takes the form of a biLaplacian (Cross–Newell 1984). However, except for special cases (see Meiron & Newell 1985) for which the dislocation is stationary, this kind of regularization proves to be inadequate, especially for defect cores and time-dependent situations. A much more attractive possibility, and one that fits naturally with the idea that, near singularities, the amplitude becomes an independent and active order parameter, is to use the amplitude. Indeed, it turns out that in the region in which one matches the solution at a dislocation core to the outer solution described by the phase equation, the amplitude correction is more important. As mentioned in §4, we have as a goal to compute the appropriate amplitude equation for the Oberbeck–Boussinesq equations, but for the purposes of this Appendix shall use the model equations (2.42), (2.43) of the Cross–Newell paper. We conjecture that, for sufficiently small ϵ, the results on the stability of the focus are relatively insensitive to the exact form of the amplitude equation. In this model, the diffusion term in the amplitude equation has been simplified by a Laplacian, the phase equation retains its form with a simplified mean drift. The equations read:

$$A^2(\Theta_T + \gamma \boldsymbol{k} \cdot \boldsymbol{V}) + \boldsymbol{\nabla} \cdot [\boldsymbol{k} A^2 F(k)] = 0, \tag{E 1}$$

$$\epsilon^2(\partial_T - \Delta) A = \mu^2(k) A - A^3, \tag{E 2}$$

$$\boldsymbol{\nabla}\psi = \boldsymbol{\nabla} \times \{\boldsymbol{k}\boldsymbol{\nabla} \cdot (\boldsymbol{k}A^2)\} \tag{E 3}$$

$$\boldsymbol{V} = \boldsymbol{\nabla} \times \psi \boldsymbol{z}. \tag{E 4}$$

The notation is the same as used in the rest of the paper; (r, θ) will designate polar coordinates in the plane, $\tau(k)$ is replaced by the active order parameter A^2 and $B(k)$ by $A^2F(k)$, γ is $-\rho\sigma/\beta$. We shall consider only the simplest stationary solution $\Theta_0 = k_0 r, A = \mu(k_0)$ where $F(k_0) = 0$, avoiding the consideration of wall boundary layers necessary if rolls of wavenumbers k_0 did not 'fit' in the box. The above simplifications lead to the boundary conditions $k = k_0(k_B)$ and $A = \mu(k_0)$ on the boundary of the container ($r = 1$). Another condition for Θ is the conservation of the number of rolls. Let

$$\Theta = k_0(r + D(r, \theta, T)), \quad A = \mu(k_0)[1 + a(r, \theta, T)], \quad \psi = \phi(r, \theta, T). \tag{E 5}$$

For brevity we consider only the most unstable mode $m = 1$. A linearization of the equations leads to

$$y'' + \frac{1}{r}y' + \left\{\sigma - \frac{(1 - s_1)}{r^2}\right\} y = \frac{w}{r^2}, \tag{E 6}$$

$$w'' + \frac{1}{r}w' + \left\{\sigma\omega - \frac{1}{\eta^2} - \frac{1}{r}\right\} w = \frac{s_2}{\eta^2} y, \tag{E 7}$$

where

$$D'(r,T) = y\,\mathrm{e}^{-\sigma(-k_0F_0')T}, \quad a(r,T) = \left(\frac{2\gamma\mu_0^2 k_0}{-F_0'}\right)^{-1} w\,\mathrm{e}^{-\sigma(-k_0F_0')T}$$

$$\omega = -k_0F_0', \quad s_1 = \frac{\gamma(\mu_0^2)\,k_0}{F_0'}, \quad s_2 = \frac{\gamma(\mu_0^2)'\,k^2}{F_0'}, \quad \eta = \frac{\epsilon}{\sqrt{2\mu_0}}. \tag{E 8}$$

The boundary conditions take the form:

$$y(0) = w(0) = 0, \quad y(1) = w(1) = 0, \quad D(1) = 0. \tag{E 9}$$

The last two conditions have already been discussed. A study of (E 6)–(E 7) near the origin $r = 0$ leads us to the first. Otherwise solutions are unbounded. The finiteness of the box is now measured by the parameter η. When η goes to zero (large containers) one recovers (3.34) where $s = s_1 + s_2$. In this case the amplitude is slaved to the wavevector within the whole container by the relation:

$$w = -s_2 y. \tag{E 10}$$

For a finite value of η there is a boundary layer of width η near the origin near which the algebraic relation (E 10) no longer holds. One finds instead from (E 6) that

$$w = s_1 y, \tag{E 11}$$

and both w and y are proportional to r as $r \to 0$. These facts assure us of the convergence of both the radial and azimuthal velocities near the origin. Inner and outer solutions of (E 6) and (E 7) can be found in terms of generalized Bessel functions with both real and imaginary index. Matching these solutions requires the detailed analysis of a fourth-order system, and so we chose to solve this system numerically. The behaviour near the origin indicates that a Galerkin expansion of both y and w in terms of the Bessel functions $J_1(\sigma_i r)$, $i = 1, \ldots N$, is appropriate. They form an orthogonal basis with respect to the scalar product $\langle f, g\rangle = \int_0^1 rf(r)\,g(r)\,\mathrm{d}r$ if σ_i is the ith positive zero of J_1. Writing

$$y = \sum_{i=1}^{N} y_i J_1(\sigma_i r), \; w = \sum_{i=1}^{N} w_i J_1(\sigma_i r),$$

we obtain the following generalized eigenvalue problem:

$$\boldsymbol{M}\begin{bmatrix} y_i \\ w_i \end{bmatrix} = \sigma \boldsymbol{L}\begin{bmatrix} y_i \\ w_i \end{bmatrix}, \tag{E 12}$$

where $\boldsymbol{M}$ and $\boldsymbol{L}$ are the following block matrices:

$$M_{ki} = \begin{bmatrix} \sigma_i^2 I_{ki}^{(3)} - s_1 I_{ki}^{(1)} & I_{ki}^{(1)} \\ \dfrac{s_2}{\eta^2} I_{ki}^{(3)} & \left(\sigma_i^2 - \dfrac{1}{\eta^2}\right) I_{ki}^{(3)} \end{bmatrix},$$

$$L_{ki} = \begin{bmatrix} I_{ki}^{(3)} & 0 \\ 0 & \omega I_{ki}^{(3)} \end{bmatrix},$$

with

$$I_{ki}^{(1)} = \int_0^1 tJ_1(\sigma_k t)\,J_1(\sigma_i t)\,\mathrm{d}t = \tfrac{1}{2}\delta_{ki}[J_1'(\sigma_k)]^2, \quad I_{ki}^{(3)} = \int_0^1 t^3 J_1(\sigma_k t)\,J_1(\sigma_i t)\,\mathrm{d}t.$$

We find (i) The point at which instability ($\sigma = 0$) occurs depends strongly on

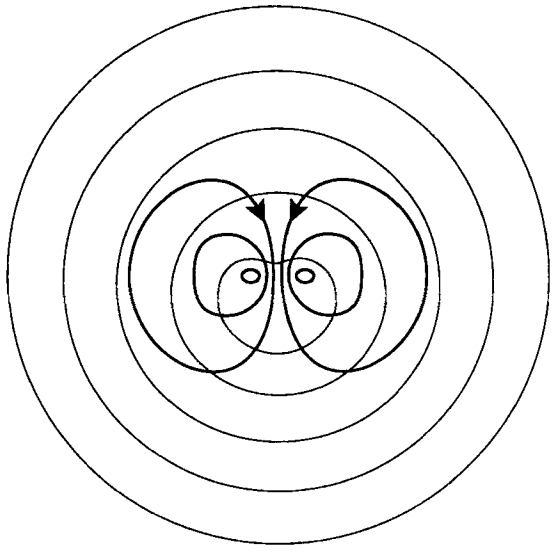

FIGURE 15. Isovalues of $|\Theta|$ calculated by (E 5) and streamlines of the mean drift field.

R/R_c	ω	s_1	s_2	σ_1	σ_2
2.0	2.73	−0.02	0.66	10.81	10.82
2.5	2.84	−0.06	−0.97	8.93	8.61
3.0	3.0	−0.1	1.23	7.16	6.0
3.5	3.16	−0.18	1.47	5.84	3.31
4.0	3.33	−0.23	1.68	4.42	−0.91
4.5	3.5	−0.28	1.87	3.14	−6.85

TABLE 3. Values of σ_1 (at $\eta = 0.05$) and σ_2 (at $\eta = 0.01$) for different values of R at $P = 6.1$

$s = s_1 + s_2$ and only weakly on $s_1 - s_2$ and ω. (ii) The growth rate σ passes through zero on the real axis. (iii) The limit $\eta \to 0$ is singular owing to the lack of regularity on the eigenmodes near the origin for $s > 1$. (iv) For values of $\omega = 1$, $s_2 = 2.5$, we found the instability to occur at $s = 2.4$ when $\eta = 0.1$, $s = 1.95$ for $\eta = 0.05$ and $s = 1.45$ for $\eta = 0.01$. (v) We plan to investigate the behaviour at lower values of η more carefully but from preliminary results at the lowest value of η we were able to resolve suggest a value of s of about 1.3. It is probably quite fortuitous that the transition seen by Steinberg *et al.* occurred at $R = 3.5$ for which $s = 1.29$, especially since the η in their case is quite large.

Although our results are not rigorous, we can say definitely that $s = 1$ provides a lower bound for instability. We believe that the behaviour of the most unstable eigenmode near $r = 0$ (whether outside the boundary layer it diverges like $-\ln r$ or $r^{-\alpha}$, $\alpha > 0$) is very sensitive to $s - 1$. (vi) When s decreases below unity, the growth rate σ quickly falls, indicating that perturbations from the circular state are heavily damped. In these cases, one needs a large forcing, either from the smaller k again at the boundary or between the circular patches, to sustain the mean drift. Table 3 displays the values of σ for $\eta = 0.05$ (σ_1) and $\eta = 0.01$ (σ_2) at $P = 6.1$ and for different values of R. Note that we took the value of ω and s_2 from (E 8) but calculated s_1 by $s_1 = s - s_2$ with s given from table 1. This takes into account the terms of the mean

drift equation that were neglected in (E 3). Observe that the decay rates are relatively insensitive to aspect ratio when they are large! They are very sensitive, however, near the stability point.

We close this Appendix with a word about the graph of the eigenmodes $y(r)$ and $w+s_2 y$ for $s_1 = -0.5$, $s_2 = 2.5$ and $\eta = 0.5$, (figure 14, see §3.2). The combination $w+s_2 y$ corresponds to the unslaved part of the amplitude. It is concentrated at the origin in the boundary layer of width η. Observe from figure 14 that the amplitude of $w+s_{2y}$ is approximately one third that of y at its maximum where the roll comparison is greatest. We also display on the same graph the functions $D(r)$ and $\phi(r)$. Figure 15 shows the corresponding spatial configuration of the off-centred rolls with the mean drift.

REFERENCES

AHLERS, G. & BEHRINGER, R. 1978 Evolution of turbulence from the Rayleigh–Bénard instability. *Phys. Rev. Lett.* **40**, 712–716.

AHLERS, G., STEINBERG, V. & CANNELL, D. S. 1985 Time dependence of flow patterns near the convective threshold in a cylindrical container. *Phys. Rev. Lett* **54**, 1373.

ARTER, W., BERNOFF, A. & NEWELL, A. C. 1987 Wavenumber selection of rolls in a box. *Phys. Fluids* **30**, 3840–3842.

ARTER, W. & NEWELL, A. C. 1988 Numerical simulation of Rayleigh–Bénard convection in shallow tanks. *Phys. Fluids* **31**, 2474–2485.

BERGÉ, P. & DUBOIS, M. 1974 Convective velocity field in the Rayleigh–Bénard instability: experimental results. *Phys. Rev. Lett.* **32**, 1041–1044.

BERNOFF, A. 1990 Structure and dynamics of dislocations in anisotropic pattern-forming systems. Preprint.

BODENSCHATZ, E., PESCH, W. & KRAMER, L. 1989 *Physica* **32D**, 135–145.

BOLTON, E. W., BUSSE, F. H. & CLEVER, R. M. 1986 Oscillatory instabilities of convection rolls at intermediate Prandtl numbers. *J. Fluid Mech.* **164**, 469–485.

BROWN, S. N. & STEWARDSON, K. 1978 On finite amplitude Bénard convection in a cylindrical container. *Proc. R. Lond.* A **360**, 455–469.

BUELL, J. C. & CATON, I. 1986 Wavenumber selection in large-amplitude axisymmetric convection. *Phys. Fluids* **29**, 23–30.

BUSINGER, P. A. & GOLUB, G. H. 1969 *Comm. Assoc. Comp. Mach.* **12**, 564–565.

BUSSE, F. H. 1967 On the stability of two-dimensional convection in a layer heated from below. *J. Math. Phys.* **46**, 149–150.

BUSSE, F. H. 1978 Nonlinear properties of convection. *Rep. Prog. Phys.* **41**, 1929–1967.

BUSSE, F. H. 1981 Transition to turbulence in Rayleigh–Bénard convection. In *Hydrodynamic Instabilities and the Transition to Turbulence* (ed. H. L. Swinney and J. P. Gollub), p. 97. Springer.

BUSSE, F. H. & WHITEHEAD, J. A. 1971 Instabilities of convection rolls in a high Prandtl number fluid. *J. Fluid Mech.* **47**, 305–320.

BUSSE, F. H. & WHITEHEAD, J. A. 1974 Oscillatory and collective instabilities in large Prandtl number convection. *J. Fluid Mech.* **66**, 67–79.

CHANDRASEKHAR, S. 1961 *Hydrodynamic and Hydromagnetic Stability*. Oxford University Press.

CHEN, K. P. & JOSEPH, D. D. 1990 Application of the singular value decomposition to the numerical computation of the coefficients of amplitude equations and normal forms, preprint.

CLEVER, R. M. & BUSSE, F. H. 1974 Transition to time dependent convection. *J. Fluid Mech.* **65**, 625–645.

CLEVER, R. M. & BUSSE, F. H. 1978 Large wavelength convection rolls in low Prandtl number fluid. *Z. Agnew Math. Phys.* **29**, 711–714.

CLEVER, R. M. & BUSSE, F. H. 1979 Instabilities of convection rolls in a fluid of moderate Prandtl number. *J. Fluid Mech.* **91**, 319–335.

CROQUETTE, V. 1989*a* Convective pattern dynamics at low Prandtl number. Part I. *Contemp. Phys.* **30**, No. 2, to appear.

CROQUETTE, V. 1989*b* Convective pattern dynamics at low Prandtl number. Part II. *Contemp. Phys.* **30**, No. 2, to appear.

CROQUETTE, V., LE GAL, P. & POCHEAU, A. 1986*a* *Physica Scr.* **33**, 135.

CROQUETTE, V., LE GAL, P., POCHEAU, A. & GUGIELMETTI, R. 1986*b* Large-scale flow characterization in a Rayleigh–Bénard convection pattern. *Europhys. Lett.* **1**, 393.

CROQUETTE, V., MORY, M. & SCHOSSELER, F. 1983 Rayleigh–Bénard convective structures in a cylindrical container. *J. Phys. Paris* **44**, 293.

CROQUETTE, V. & POCHEAU, A. 1984 Wavenumber selection in Rayleigh–Bénard convective structures. In *Cellular structures in Instabilities* (ed. J. E. Wesfrid & S. Zaleski). Springer.

CROSS, M. C. 1983 Phase dynamics of convection rolls. *Phys. Rev.* A **27**, 490–498.

CROSS, M. C. & NEWELL, A. C. 1984 Convection patterns in large aspect ratio systems. *Physica* **10D**, 299–328.

DUBOIS, M. & BERGE, P. 1978 Experimental study of the velocity field in Rayleigh–Bénard convection. *J. Fluid Mech.* **85**, 641–653.

ECKHAUS, A. W. 1965 *Studies in Nonlinear Stability Theory.*

GOLLUB, J. P., MCCARRIAR, A. R. & STEINMAN, J. F. 1982 Convective pattern evolution and secondary instabilities. *J. Fluid Mech.* **125**, 259–281.

GREENSIDE, H. S. & COUGHRAN, W. M. 1986 Nonlinear pattern formation near the onset of Rayleigh–Bénard convection. *Phys. Rev.* A **30**, 398–428.

GREENSIDE, H. S., CROSS, M. C. & COUGHRAN, W. M. JR. 1988 Mean flows and the onset of chaos in large-cell convection. *Phys. Rev. Lett.* **60**, 2269–2272.

HEUTMAKER, M. S. & GOLLUB, J. P. 1987 Wave-vector field of convective flow patterns. *Phys. Rev.* A **35**, 242–260.

HOWARD, L. N. & KOPELL, N. 1977 Slowly varying waves and shock structures in reaction diffusion equations. *Stud. Appl. Maths* **56**, 95–145.

KOLODNER, P., PASSNER, A., SURKO, C. M. & WALDEN, R. W. 1986*a* Onset of oscillatory convection in a binary fluid mixture. *Phys. Rev. Lett* **56**, 2621–2624.

KOLODNER, P., WALDEN, R. W., PASSNER, A. & SURKO, C. M. 1986*b* Rayleigh–Bénard convection in an intermediate-aspect-ratio rectangular container. *J. Fluid Mech.* **163**, 195–226.

KOSCHMEIDER, E. L. & PALLAS, S. C. 1974 Heat transfer through a shallow, horizontal convecting fluid layer. *Trans. ASME* C: *J. Heat Mass Transfer* **17**, 991.

KRISHNAMURTI, R. 1970 On the transition to turbulent convection. Part 1. The transition from two- to three-dimensional flow. *J. Fluid Mech.* **42**, 295–307.

LOWE, M. & GOLLUB, J. P. 1986 Pattern selection near the onset of convection: The Eckhaus instability. *Phys. Rev.* A **32**, 125–130.

MALKUS, W. V. R. & VERONIS, G. 1958 Finite amplitude convection. *J. Fluid Mech.* **4**, 225–260.

MEIRON, D. & NEWELL, A. C. 1985 The shape of stationary dislocations. *Phys. Lett.* 113A, 289–292.

NEWELL, A. C. 1988 The dynamics of patterns: A survey. In *NATO workshop on Propagation in Nonequilibrium Systems, Les Houches, France.* 1987 (ed. J. E. Wesfried, H. Brand, P. Manneville, G. Albinet and N. Boccara.) Springer.

NEWELL, A. C. 1989 The dynamics and analysis of patterns. In *Complex Systems* (ed. D. Stein), pp. 107–173. Santa Fe Institute of Studies in the Sciences of Complexity. Addison-Wesley.

NEWELL, A. C. & WHITEHEAD, J. A. 1969 Finite bandwidth, finite amplitude convection. *J. Fluid Mech.* **38**, 279–303.

PALM, E. 1975 Nonlinear thermal convection. *Ann. Rev. Fluid Mech.* **7**, 39–61.

POCHEAU, A. 1988 Transition to turbulence of convective flows on a cylindrical container. *J. Phys. Paris* **49**, 1127–1145.

POCHEAU, A., CROQUETTE, V. & LE GAL, P. 1985 Turbulence on a cylindrical container of Argon near threshold of convection. *Phys. Rev. Lett.* **55**, 1094–1097.

POMEAU, Y. & MANNEVILLE, P. 1979 Stability and fluctuations of a spatially periodic convective flow. *J. Phys. Lett.* **40**, 609.

POMEAU, Y. & MANNEVILLE, P. 1981 Wavelength selection in axisymmetric cellular structures. *J. Phys. Lett.* **42**, 1067–1074.

POMEAU, Y., ZALESKI, S. & MANNEVILLE, P. 1985 Axisymmetric cellular structures revisited. *Z. Angew. Math. Phys.* **36**, 367–394.

SCHÜLTER, A., LORTZ, D. & BUSSE, F. H. 1965 On the stability of steady finite amplitude convection. *J. Fluid Mech.* **23**, 129–144.

SEGEL, L. A. 1969 Distant side-walls cause slow amplitude modulation of cellular convection. *J. Fluid Mech.* **38**, 203–224.

SEGEL, L. A. & STUART, J. T. 1962 On the question of the preferred mode in cellular thermal convection. *J. Fluid Mech.* **13**, 289–306.

SIGGIA, E. D. & ZIPPELIUS, A. 1981*a* Dynamics of defects in Rayleigh–Bénard convection. *Phys. Rev.* A **24**, 1036.

SIGGIA, E. D. & ZIPPELIUS, A. 1981*b* Pattern selection in Rayleigh–Bénard convection near threshold. *Phys. Rev. Lett.* **47**, 835.

STEINBERG, V., AHLERS, G. & CANNELL, D. S. 1985 Pattern formation and wavenumber selection by Rayleigh–Bénard convection in a cylindrical container. *Physica Scr.* **32**, 534–547.

STUART, J. T. 1960 On the nonlinear mechanics of wave disturbances in stable and unstable parallel flows. Part 1. The basic behaviour in plane Poiseuille flow. *J. Fluid Mech.* **9**, 353–370.

WATSON, J. 1960 On the nonlinear mechanics of wave disturbances in stable and unstable parallel flows. Part 2. The development of a solution for plane Poiseuille flow and for plane Couette flow. *J. Fluid Mech.* **9**, 371–389.

WHITHAM, G. B. 1974 *Linear and Nonlinear Waves*. Wiley-Interscience.